Oxidative Medicine and Cellular Longevity

Oxidative Stress and Epigenetics in Vascular Aging: From Basic to Clinical Research

Lead Guest Editor: Jian Zhang
Guest Editors: Chen Chen and Yanshuo Han

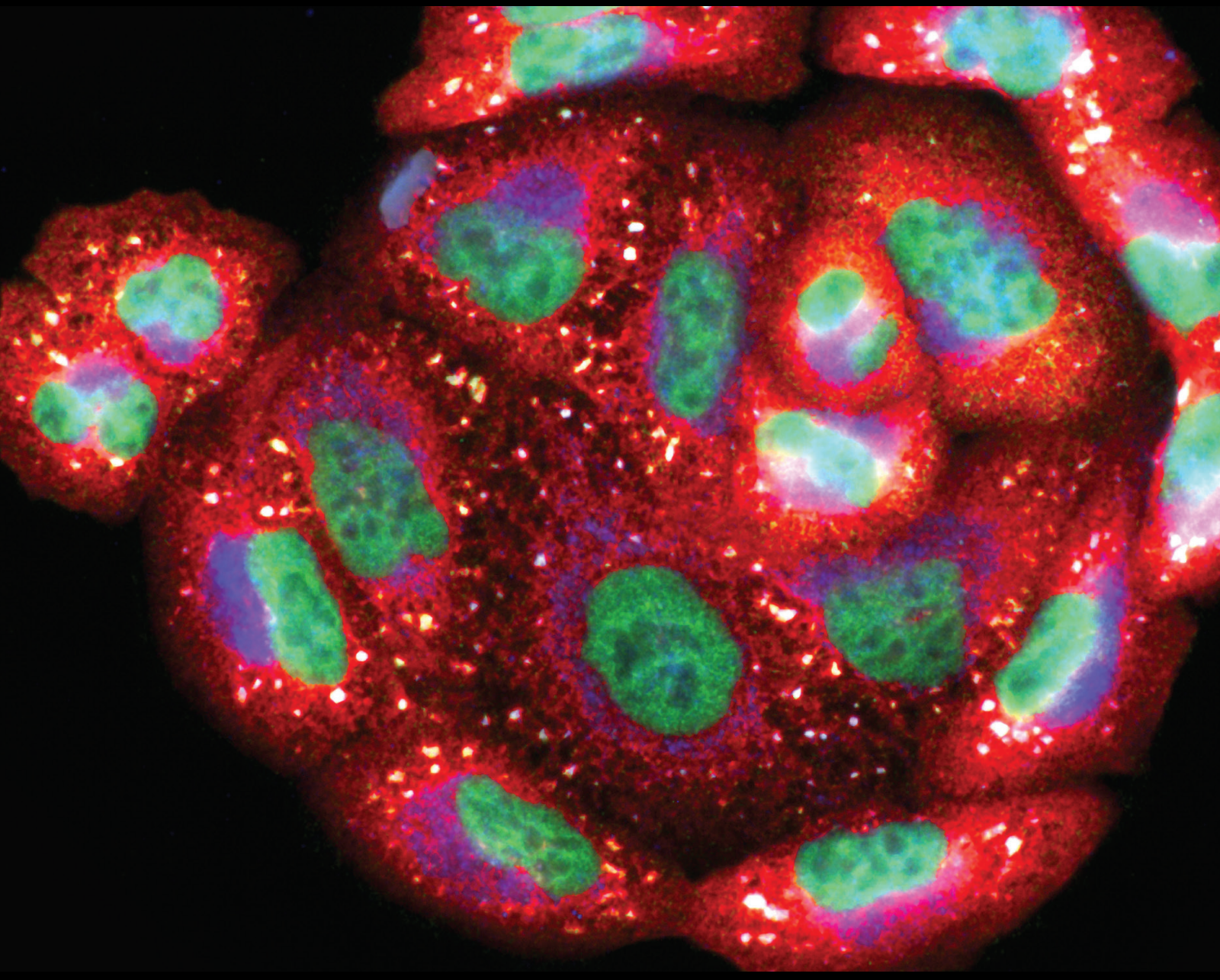

Oxidative Stress and Epigenetics in Vascular Aging: From Basic to Clinical Research

Oxidative Medicine and Cellular Longevity

Oxidative Stress and Epigenetics in Vascular Aging: From Basic to Clinical Research

Lead Guest Editor: Jian Zhang
Guest Editors: Chen Chen and Yanshuo Han

Contents

Hindawi
Oxidative Medicine and Cellular Longevity
Volume 2023, Article ID 3918393, 23 pages
https://doi.org/10.1155/2023/3918393

Research Article

The Effect of N6-Methyladenosine Regulators and m6A Reader YTHDC1-Mediated N6-Methyladenosine Modification Is Involved in Oxidative Stress in Human Aortic Dissection

Fanxing Yin,[1] Kun Liu,[2] Wanfu Peng,[2] Deying Jiang,[3] Hao Zhang,[1] Panpan Guo,[1] Yinhao Wu,[1] Xiaoxu Zhang,[1] Chenxi Sun,[1] Yaxuan Wang,[1] Hecheng Wang,[1] and Yanshuo Han[1]

[1]*School of Life and Pharmaceutical Sciences, Dalian University of Technology, Panjin, China*
[2]*Department of Cardiac Surgery, Affiliated Hospital of Guizhou Medical University, Guiyang, China*
[3]*Department of Vascular Surgery, Dalian Municipal Central Hospital, Dalian, China*

Correspondence should be addressed to Hecheng Wang; wanghc@dlut.edu.cn and Yanshuo Han; yanshuohan@dlut.edu.cn

Received 3 August 2022; Revised 4 October 2022; Accepted 24 November 2022; Published 9 February 2023

Academic Editor: Ammar AL-Farga

Aortic dissection (AD) develops pathological changes in the separation of the true and false aortic lumen, with high lethality. m6A methylation and oxidative stress have also been shown to be involved in the onset of AD. Through bioinformatics methods, three differentially expressed m6A regulators (YTHDC1, YTHDC2, and RBM15) were excavated from the GSE52093 dataset in the Gene Expression Omnibus (GEO) database, and functional enrichment analysis of the differentially expressed genes (DEGs) regulated by m6A regulators was performed. Then, the genes with oxidative stress-related functions among these genes were found. The protein interaction network of the oxidative stress-related genes and the competing endogenous RNA- (ceRNA-) miRNA-mRNA network were constructed. Among them, DHCR24, P4HB, and PDGFRA, which have m6A differences in AD samples, were selected as key genes. We also performed immune infiltration analysis, as well as cell-gene correlation analysis, on samples from the dataset. The results showed that YTHDC1 was positively correlated with macrophage M1 and negatively correlated with macrophage M2. Finally, we extracted AD and healthy aorta RNA and protein from human tissues that were taken from AD patients and patients who received heart transplants, performed quantitative real-time PCR (qRT-PCR) on YTHDC2 and RBM15, and performed qRT-PCR and western blot (WB) detection on YTHDC1 to verify their differences in AD. The mRNA and protein levels of YTHDC1 were consistent with the results of bioinformatics analysis and were downregulated in AD. Immunofluorescence (IF) was used to colocalize YTHDC1 and endothelial cell marker CD31. After knocking down YTHDC1 in human umbilical vein endothelial cells (HUVECs), reactive oxygen species (ROS) levels had a tendency to increase and the expression of peroxide dismutase SOD2 was decreased. This study provides assistance in discovering the role of m6A regulator YTHDC1 in AD. In particular, m6A modification participates in oxidative stress and jointly affects AD.

1. Introduction

AD is a life-threatening medical emergency in which the inner layer of the aorta is torn or bleeding inside the aortic wall, resulting in the separation of different layers of the aortic wall; incidence rates in the general population range from 3.5 to 6 per 100,000 people [1, 2]. It is characterized by separation of the aortic parietal and subsequent creation of a false lumen that may compress the true aortic lumen. Hypertension, atherosclerosis, and some connective tissue diseases (Marfan and Ehlers-Danlos syndromes) are predisposing factors that may induce AD [3]. Its pathological process is closely related to the abnormal state of endothelial cells and smooth muscle cells and the infiltration of inflammatory cells such as macrophages into the aortic wall [4–6]. The classification of AD depends on the duration of

treatment after symptom onset. Therefore, AD was acute dissection in the first two weeks, subacute after three months, and chronic after three months [7]. In patients with untreated acute aortic dissection (AAD), mortality after symptom onset increases by 1-2% per hour [8]. The current treatment for AD is surgery; although the outcome is improving, many debates about the optimal treatment remain [9]. The surgery requires a high level of skill and needs to be performed in a medical center. Patients in some underdeveloped areas are not treated in time, resulting in poor survival [10]. Prevention or treatment other than surgery is necessary. A study by Beam and Moore found that the occurrence of AD was associated with a positive family history of the patient [11]. Therefore, by identifying some key genes of AD, it may provide new ideas or methods for the treatment of AD. It is difficult to mine these genes through experiments, but it is very feasible to screen them through bioinformatics.

Adenosine methylation at the N6 position, known as m6A, is the most abundant posttranscriptional chemical modification, both in human mRNA and noncoding RNA [12]. Aberrant m6A modification levels have been implicated in various cytopathological processes such as nuclear RNA export, splicing, mRNA stability, miRNA biogenesis, and lncRNA metabolism [13]. In the study of vascular diseases, there is emerging evidence that abnormal m6A is closely related to the pathogenesis of cardiovascular diseases (CVDs) such as aortic aneurysm, vascular calcification, and pulmonary hypertension [14]. Moreover, the reduction of m6A modification level helps to inhibit the differentiation of vascular smooth muscle [15]. These are potential predisposing factors for AD, so the occurrence of AD is likely related to m6A modification. The effects of m6A on mRNA are mediated by "readers" (effectors recognizing m6A), "writers"-complex components (m6A methyltransferases), and potential "erasers" (m6A demethyltransferases) [16, 17]. Modification of m6A is performed by m6A writers, removed by m6A erasers, and recognized by reader proteins [18]. These m6A regulators are the basis and key to study m6A modification. Some m6A regulators have been found to be related to CVDs. For example, YTHDF1 can regulate pulmonary hypertension and ALKBH5 has the function of regulating the proliferation of cardiomyocytes and cardiac regeneration, as well as METTL14 leading to increased endothelial inflammation and the development of atherosclerosis [19–21]. In the aspect of AD, Zhou et al. found that the high expression of MTEEL14 and the low expression of FTO may act on some functional genes to alter their m6A levels, thereby regulating the pathogenesis of AD [22].

An imbalance between the production of ROS and the endogenous antioxidant defense system is called oxidative stress [23]. Oxidative stress has been identified as one of the underlying common causes of CVDs with vascular damage [24]. Basal concentrations of ROS are essential for the performance of cellular functions, but uncontrolled ROS concentrations can adversely affect cellular macromolecules, which can further lead to endothelial and vascular smooth muscle cell damage [25–27]. These adverse consequences of ROS cannot be avoided if endogenous antioxidants do not sufficiently function as checkpoints. Therefore, oxidative stress may also be a potential inducer of AD to a large extent. A complex relationship exists between oxidative stress-related and m6A-regulated signaling pathways, while ROS signaling has the function of regulating m6A modification [28]. Oxidative stress can upregulate or downregulate some m6A regulators to alter the degree of m6A modification and affect related molecular mechanisms [29, 30]. The molecular mechanism by which m6A and oxidative stress coact in AD is the focus of this study.

We were dedicated to discovering the underlying molecular mechanisms underlying m6A regulator-mediated m6A modification in relation to oxidative stress in AD, to provide a theoretical ground for the progress of AD etiology in the direction of the synergistic effects of m6A and oxidative stress. In this study, we first analyzed the datasets containing AD tissues and normal tissues in the GEO database, found differentially expressed m6A regulators, and constructed a network of m6A regulators and their target genes related to oxidative stress. We performed a comprehensive analysis of these genes, including enrichment analysis, ceRNA regulatory network construction, immune infiltration correlation, and drug interaction analysis. Then, we identified the differential expression of m6A regulators by quantitative real-time PCR and western blot. IF was used for colocalization. Finally, we attempted to verify the effect of YTHDC1 on ROS levels in HUVECs.

2. Materials and Methods

2.1. Data Collection and Screening of Differentially Expressed m6A Regulatory Genes. We searched the database for studies on human AD in the GEO database (https://www.ncbi.nlm.nih.gov/geo/). The mRNA expression profiling dataset GSE52093 which included AD ($n = 5$) and normal control samples ($n = 7$) was selected. Differential expression analysis of genes between AD and normal aorta was performed by using the R software package "limma." Genes with adjusted P value < 0.05 and $|\log FC| \geq 0.5$ were identified as DEGs. Common m6A methylation regulators include ten m6A readers (HNRNPA2B1, HNRNPC, IGF2BP1, IGF2BP2, IGF2BP3, YTHDC1, YTHDC2, YTHDF1, YTHDF2, and YTHDF3), ten m6A writers (HAKAI, METTL3, METTL14, METTL16, RBM15, RBM15B, WTAP, VIRMA, ZC3H13, and ZCZHC4), and two kinds of m6A erasers (ALKBH5 and FTO). Thereafter, the m6A regulators with P value < 0.05 and $|\log FC| \geq 0.7$ were considered as differentially expressed m6A regulatory genes (DEMRGs).

2.2. Functional Enrichment Analysis of Differential m6A Regulatory-Related Genes. The m6A2Target database (http://m6a2target.canceromics.org) was used for prediction of the target genes of DEMRGs. The common parts of the target genes and the DEGs were differential m6A regulation-related genes. Gene Ontology (GO) enrichment analysis and Kyoto Encyclopedia of Genes and Genomes (KEGG) pathway analysis of DEMRGs were performed using the Database for Annotation, Visualization and Integrated Discovery (DAVID) (https://david.ncifcrf.gov/).

GO enrichment analysis was split into the terms of biological processes (BP), cellular components (CC), and molecular functions (MF). The enrichment results with FDR < 0.05 were regarded as statistically significant.

2.3. The Network Construction of Exosome and Programmed Cell Death-Related Genes. Oxidative stress-related genes were downloaded from the GO database. The above genes were crossed with the differential m6A regulatory-related genes to obtain the overlapped genes. The network of association between DEMRGs and overlapping genes was constructed. The PPI network was analyzed for the overlapped genes employing the Search Tool for the Retrieval of Interacting Genes (STRING) database (https://www.string-db.org) with a combined score > 0.4. Subsequently, two networks were visualized by the Cytoscape software.

2.4. ceRNA Network Construction for DEMRGs. The differentially expressed long noncoding RNAs (DE-lncRNAs) in GSE52093 were screened by using the R software package "limma." The interactions between microRNAs (miRNAs) and DEMRGs were predicted through starBase database (https://starbase.sysu.edu.cn) and miRDB database (http://mirdb.org). And the association pairs between target miRNAs and DE-lncRNAs were also predicted using starBase database. Then, the ceRNA network of mRNA-miRNA-lncRNA was constructed by using interactive miRNAs with DE-lncRNAs and DEMRGs. Cytoscape was utilized to visualize the ceRNA network of mRNA (DEMRGs)-miRNA-ceRNA (DE-lncRNA).

2.5. Establishment of a LASSO Model and ROC Curve Analysis. A LASSO model for the identification of DEMRGs was established by "glmnet" package. Determine the best variable in the model by the minimum lambda value. ROC monofactor analysis which could evaluate the stability and sensitivity was performed to evaluate the diagnostic value of DEMRGs in AD. The LASSO model and the ROC curve were both based on the gene expression profiles of hub genes which are differentially expressed between AD and control.

2.6. Identification and Analysis of Key m6A Oxidative Stress-Related Genes. The differentially methylated m6A genes between AAD and normal human aorta were obtained from the GSE147027 dataset. We found the DEGs with oxidative stress-related functions, differential m6A methylation, and regulated by DEMRGs. The GSE153434 dataset was used to verify the differential expression of these genes in different kinds of samples. These genes were defined as key genes. The "rms" package was used to establish a nomo-diagram-logistic model based on the key genes. Then, the calibration curve was established to evaluate the prediction accuracy of the nomo-diagram-logistic model. The "rmda" package was used to analyze the decision curve and clinical impact curve for assessing the nomo-diagram-logistic model. The Drug Gene Interaction Database (DGIdb) is a database of drug gene interaction data. The drugs interacting with key genes were screened by DGIdb.

2.7. Correlation Analysis between Key Genes and Immune Cells. CIBERSORTx is used to perform immune infiltration analysis of GSE52093 (https://cibersortx.stanford.edu). As the signature gene file, leukocyte signature matrix (LM22) can distinguish 22 human hematopoietic cell phenotypes. The proportion of immune cells in each sample was obtained, and further, the relationship between immune cells and genes which included DEMRGs and key genes was analyzed. The relationship of DEMRGs and key genes was also analyzed based on the expression levels in each sample.

2.8. Human Aortic Samples. All protocols using human specimens were approved by the Human Research Ethics Committees of the Affiliated Hospital of Guizhou Medical University (Guiyang, China), with approval number 2022-LS018. Aortic tissue was obtained from AD patients and patients receiving heart transplantation (controls), and informed consent was obtained from patients or their family members. All samples were stored in liquid nitrogen or paraformaldehyde as soon as possible after surgical resection to avoid sample spoilage.

2.9. The mRNA Expression Levels of DEMRGs in AD Samples. qRT-PCR was conducted to validate part of m6A methylation regulators in tissue samples. Grind human AD tissue and normal aortic tissue in liquid nitrogen to extract total RNA. Then, total RNA was reverse transcribed to cDNA using PrimeScript™ RT Master Mix (RR036A, TaKaRa Bio, Shiga, Japan), and qRT-PCR was performed using the TB Green® Premix Ex Taq™ II (RR820A, TaKaRa Bio, Shiga, Japan). GAPDH was used as the reference gene, and the relative expression levels of mRNAs in tissues were calculated with the $2^{-\Delta\Delta CT}$ method.

2.10. The Protein Expression Levels of YTHDC1 in AD Tissues. Protein samples from AD and normal tissues were added to sodium dodecyl sulfate-polyacrylamide gel (15 μg sample per gel lane) to separate, and then, the protein bands were transferred to polyvinylidene fluoride membranes. The membranes were blocked, followed by incubation with rabbit anti-YTHDC1 (abs117811, Absin, Shanghai, China) and rabbit anti-GAPDH (D110016, Sangon Biotech, Shanghai, China). The blots were then incubated with goat anti-rabbit IgG which was labeled by horseradish peroxidase. Finally, the density of immunoreactive bands normalized to the signal intensity of GAPDH was determined using the Electro Chemical Luminescence Kit and ImageJ software 1.53.

2.11. IF Colocalization of YTHDC1 and CD31 in Human AD Tissues. IF staining analysis of YTHDC1 and endothelial cell marker CD31 was carried out for cellular localization in AD tissue. AD tissue sections were passed through xylene, isopropanol, and ethanol for dewaxing and rehydrating. Dehydrated sections were placed in citrate buffer under high temperature and pressure for antigen retrieval. Then, add hydrogen peroxide to block endogenous peroxidase. After incubation, AD sections were blocked by Immunol Staining Blocking Buffer (P0102, Beyotime, Shanghai,

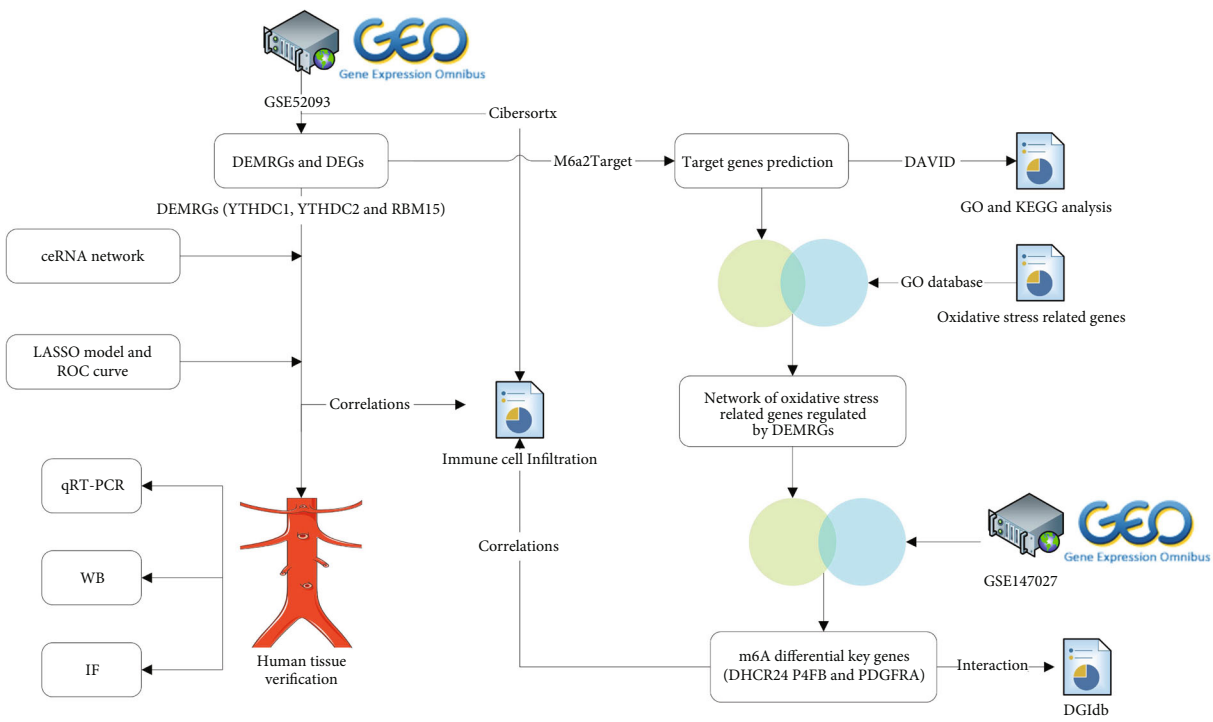

Figure 1: Study workflow.

China). Incubate tissue with rabbit anti-YTHDC1 antibody (abs117811, Absin, Shanghai, China) and the Cy3 (red)-conjugated goat anti-rabbit IgG (GB21303, Servicebio, Wuhan, China). Then, rabbit anti-CD31 antibody (abs120102, Absin, Shanghai, China) and the 488 (green)-conjugated goat anti-rabbit IgG (abs20025, Absin, Shanghai, China) were used to incubate the tissue sequentially. Finally, the sections were stained by Antifade Mounting Medium with DAPI (P0131, Beyotime, Shanghai, China). The prepared sections can be viewed under a fluorescence microscope.

2.12. Endothelial Cell Culture and YTHDC1 siRNA Transfection. HUVECs were cultured with complete growth medium DMEM High Glucose (MA0545, Meilunbio, Dalian, China), 10% fetal bovine serum (10100-147, Gibco, Thermo Fisher Scientific, USA), and 1% penicillin/streptomycin (10000 U/mL; SV30010, HyClone, USA) at 37°C in moist air with 5% CO_2. YTHDC1 siRNA and control (NC) siRNA were from RiboBio (Guangzhou, China). HUVECs were seeded into 6-well plates or 24-well plates at a concentration of 30%. After cell spreading, HUVECs were transfected with 75 nM YTHDC1 siRNAs or NC siRNAs for 48 h by riboFECT™ CP Transfection Kit (C10511-05, RiboBio, Guangzhou, China). ROS detection kit (WLA131a, Wanleibio, Shanghai, China) was used to detect ROS levels of HUVECs in the si-YTHDC1 and si-NC groups under a luciferase microplate reader. The excitation wavelength was 488 nm, and the emission wavelength at 525 nm had the maximum wave peak, and the intensity was proportional to the intracellular ROS levels. As a superoxide dismutase, SOD2 inhibits ROS levels and interacts with YTHDC1; we further examined the difference of SOD2 RNA expression between human AD tissues and normal aortic tissues. Then, total RNA was extracted after siRNA transfection, for further qRT-PCR analysis of transfection efficiency as well as RNA levels of SOD2 and pattern recognition receptors (PRRs) such as NOD1, NOD2, and NLRP3.

3. Results

3.1. Identification of Differentially Expressed m6A Regulatory Genes. The main workflow of this research is summarized in Figure 1. To obtain DEGs related to AD, we compared them with healthy controls. 1807 DEGs were obtained in GSE52093 with criteria for adjusted P value < 0.05 and $|\log FC| \geq 0.7$ (Figure 2(a) and Supplementary File 1). And the expression of m6A regulatory genes is shown in Figures 2(b) and 2(c). Through the screening of differential expression, we finally obtained three m6A regulators (YTHDC1, YTHDC2, and RBM15) as DEMRGs. Compared with normal samples, YTHDC1 and YTHDC2 were upregulated in AD tissues, whereas RBM15 was downregulated in contrast.

3.2. Functional Enrichment of Differential m6A Regulatory-Related Genes. Through the m6A2Target database, we obtained a total of 7685 target genes that may be modified by DEMRGs. The target genes of YTHDC1, YTHDC2, and RBM15 methylation modification had 5547, 2724, and 2702, respectively. The intersection genes of these target genes and DEGs were differential m6A regulatory-related genes in AD. Then, 1306 m6A regulatory-related genes were used to perform GO and KEGG enrichment analyses. 87 GO terms and 7 KEGG pathways with FDR < 0.05 were

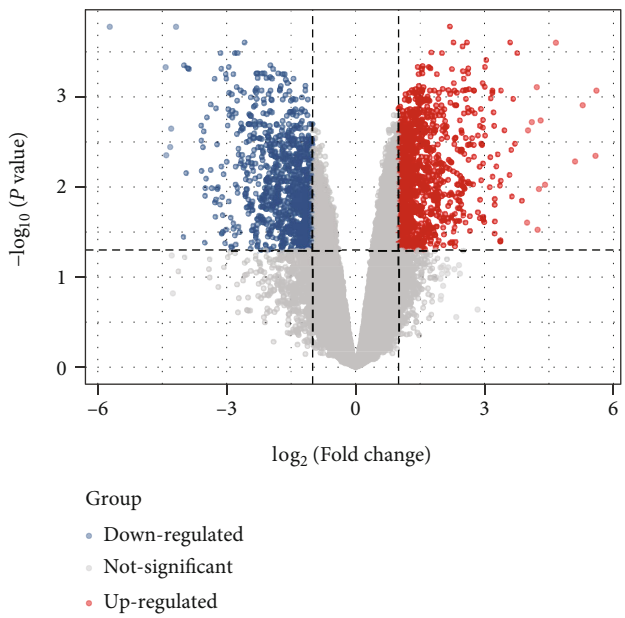

(a)

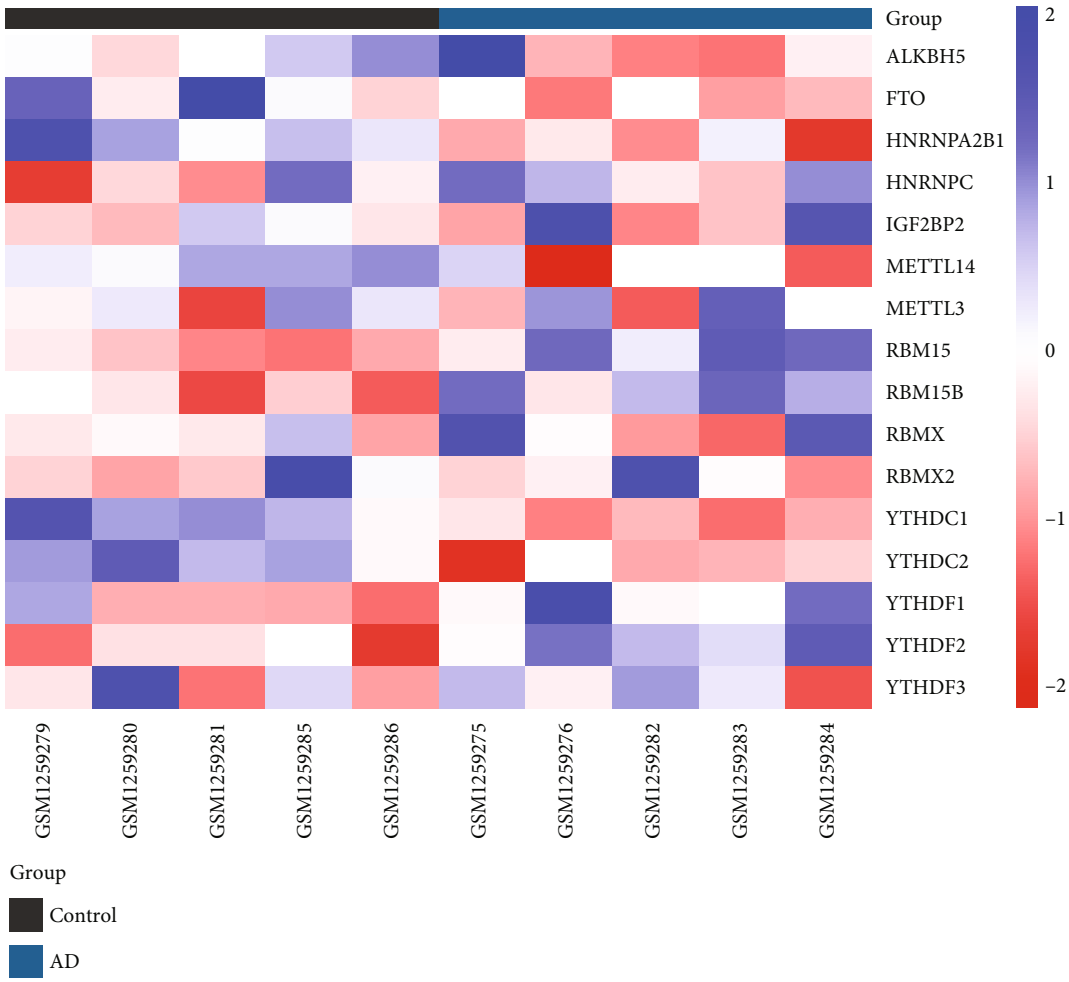

(b)

Figure 2: Continued.

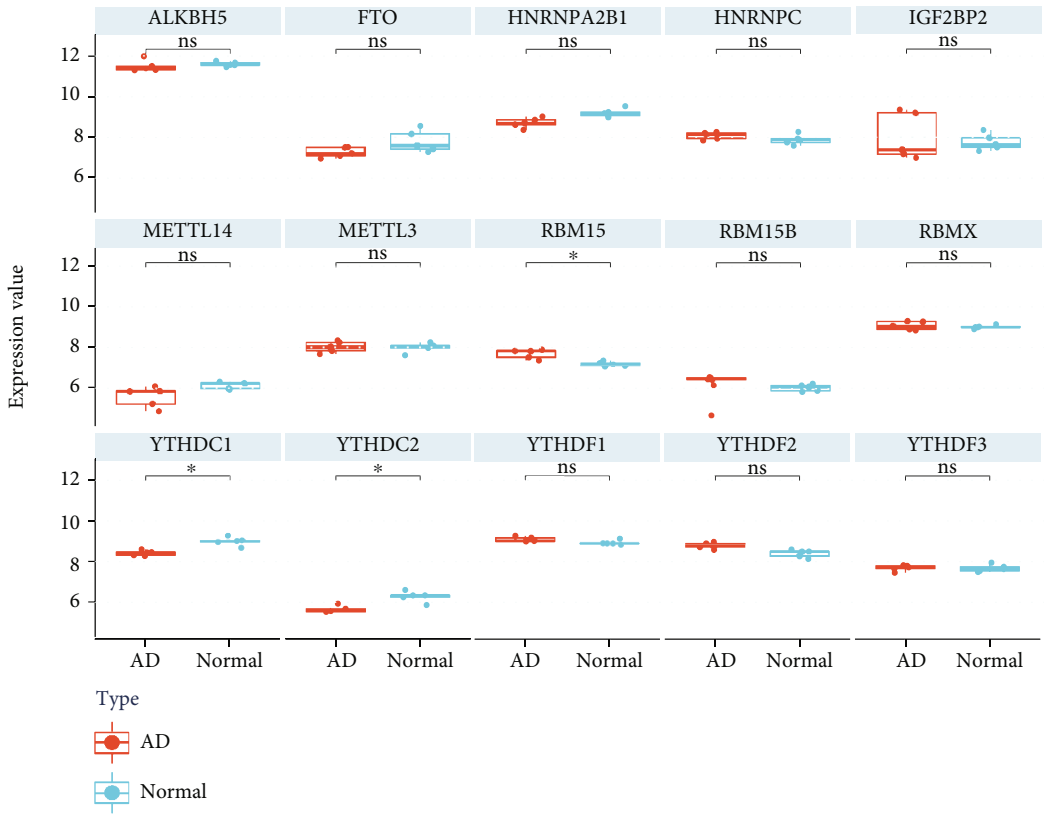

(c)

Figure 2: Identification of DEMRGs and DEGs. (a) Volcano plot of DEGs in GSE52093. (b) Heat map of differential expression of m6A regulators. (c) Expression boxplot of m6A regulators. "*" means adj. P value < 0.05.

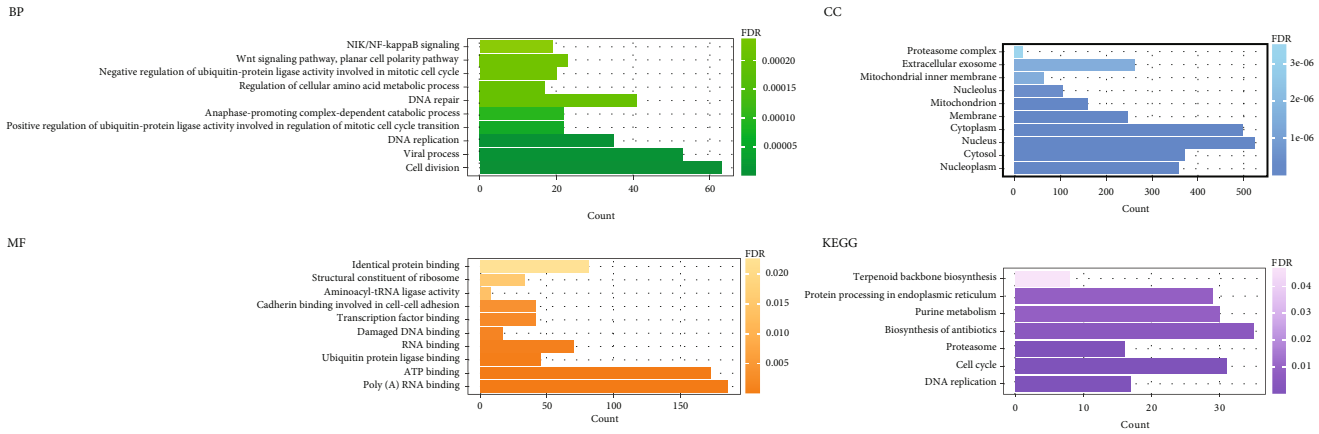

Figure 3: GO function and KEGG pathway enrichment results of DEGs regulated by DEMRGs.

obtained. GO enrichment analysis revealed that differential m6A regulatory-related genes were mainly enriched in cell division, viral process, nucleoplasm, cytosol, poly(A) RNA binding, ATP binding, etc. Overall, more functions were enriched in the translation process and cell division stage. In the KEGG pathway, differential m6A regulatory-related genes were enriched in DNA replication, cell cycle, proteasome biosynthesis of antibiotics, purine metabolism, protein processing in endoplasmic reticulum, and terpenoid backbone biosynthesis (Figure 3 and Table 1).

3.3. Association Network of Exosome and Programmed Cell Death-Related Genes. A total of 418 oxidative stress-related genes were obtained from the GO database. Then, we got the oxidative stress-related genes among the differential m6A regulatory-related genes in AD. An interaction network

Table 1: GO function and KEGG pathway enrichment results of DEGs regulated by DEMRGs.

ID	Description	Count	FDR
BP			
GO:0051301	Cell division	63	$1.29E-07$
GO:0016032	Viral process	53	$4.91E-06$
GO:0006260	DNA replication	35	$5.03E-06$
GO:0051437	Positive regulation of ubiquitin-protein ligase activity involved in the regulation of mitotic cell cycle transition	22	$5.45E-05$
GO:0031145	Anaphase-promoting complex-dependent catabolic process	22	$9.07E-05$
GO:0006281	DNA repair	41	$1.75E-04$
GO:0006521	Regulation of cellular amino acid metabolic process	17	$1.75E-04$
GO:0051436	Negative regulation of ubiquitin-protein ligase activity involved in mitotic cell cycle	20	$1.91E-04$
GO:0060071	Wnt signaling pathway, planar cell polarity pathway	23	$1.91E-04$
GO:0038061	NIK/NF-kappaB signaling	19	$2.38E-04$
CC			
GO:0005654	Nucleoplasm	359	$2.27E-34$
GO:0005829	Cytosol	371	$3.79E-23$
GO:0005634	Nucleus	525	$1.40E-20$
GO:0005737	Cytoplasm	498	$1.46E-17$
GO:0016020	Membrane	247	$3.51E-14$
GO:0005739	Mitochondrion	161	$4.36E-11$
GO:0005730	Nucleolus	106	$2.07E-07$
GO:0005743	Mitochondrial inner membrane	64	$1.35E-06$
GO:0070062	Extracellular exosome	263	$1.35E-06$
GO:0000502	Proteasome complex	19	$3.52E-06$
MF			
GO:0044822	Poly(A) RNA binding	186	$4.37E-25$
GO:0005524	ATP binding	173	$7.19E-08$
GO:0031625	Ubiquitin protein ligase binding	45	$4.40E-04$
GO:0003723	RNA binding	70	$7.82E-04$
GO:0003684	Damaged DNA binding	17	0.001372238
GO:0008134	Transcription factor binding	42	0.002543152
GO:0098641	Cadherin binding involved in cell-cell adhesion	42	0.003669701
GO:0004812	Aminoacyl-tRNA ligase activity	8	0.01359803
GO:0003735	Structural constituent of ribosome	33	0.015456237
GO:0042802	Identical protein binding	81	0.022626324
KEGG			
hsa03030	DNA replication	17	$1.13E-06$
hsa04110	Cell cycle	31	$3.92E-06$
hsa03050	Proteasome	16	$7.54E-05$
hsa01130	Biosynthesis of antibiotics	35	0.005013539
hsa00230	Purine metabolism	30	0.008102754
hsa04141	Protein processing in the endoplasmic reticulum	29	0.008102754
hsa00900	Terpenoid backbone biosynthesis	8	0.046861012

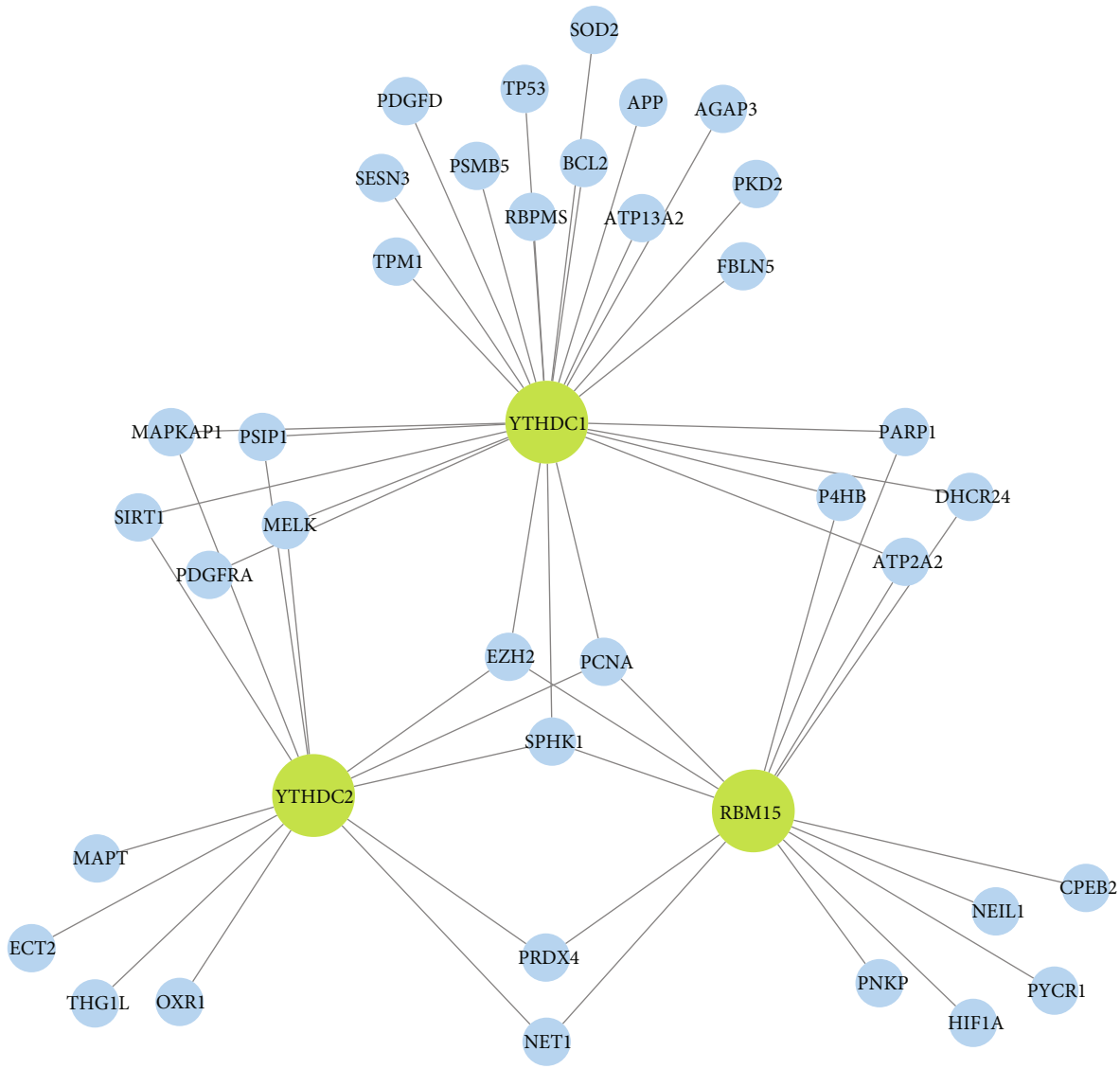

(a)

Figure 4: Continued.

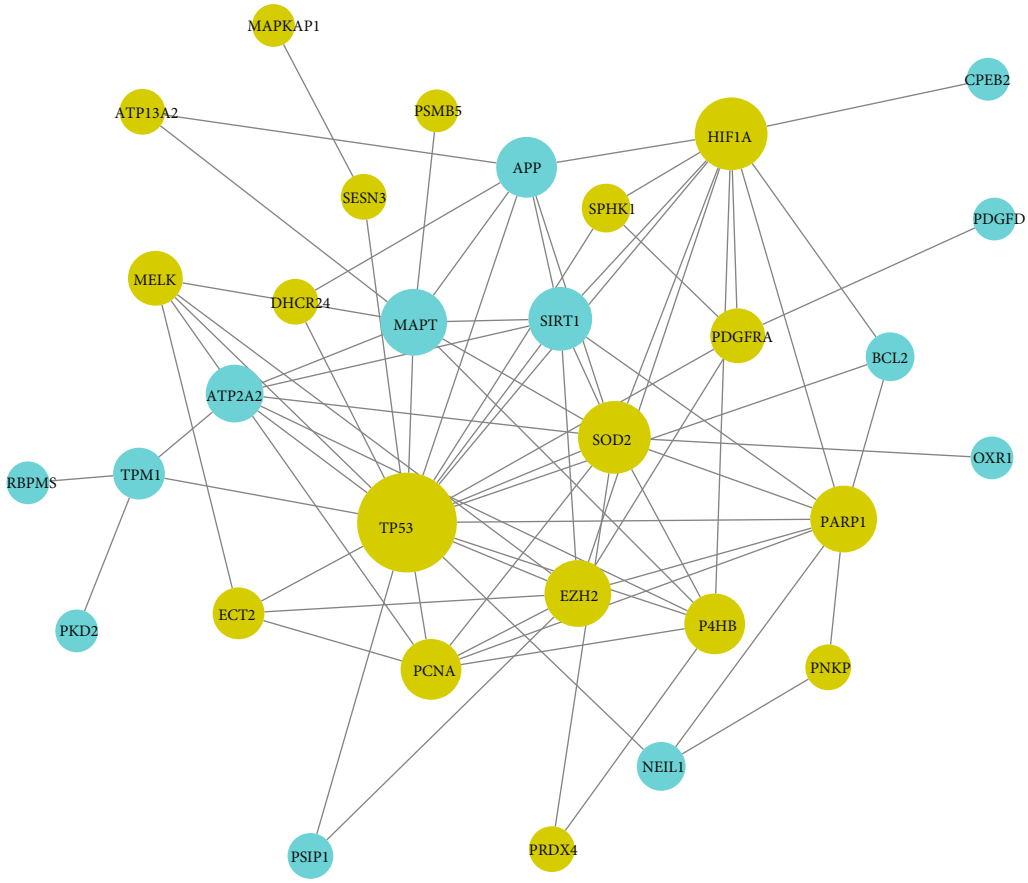

(b)

Figure 4: The network of oxidative stress-related genes regulated by DEMRGs. (a) Network of the relationship between DEMRGs and oxidative stress-related genes. (b) PPI network of oxidative stress-related genes: genes in yellow were upregulated, and genes in blue were downregulated.

was constructed to elucidate the association of DEMRGs with oxidative stress (Figure 4(a)). SOD2 was interacted with YTHDC1. Then, the PPI network of these genes was also constructed to further show the association of oxidative stress (Figure 4(b)).

3.4. ceRNA Network Construction for DEMRGs. After differential expression analysis, 16 DE-lncRNAs were screened. lncRNA-miRNA interaction pairs were predicted by the starBase database. Then, we selected the DEMRG target miRNA predicted by starBase database and miRDB database jointly. The ceRNA network of mRNA-miRNA-lncRNA for AD-related m6A regulators was constructed with 3 m6A regulators, 65 miRNAs, and 10 lncRNAs (42 miRNAs for YTHDC1, 21 miRNAs for YTHDC2, and 8 miRNAs for RBM15) (Figure 5).

3.5. Establishment of the LASSO Model and Assessment of the ROC Curve. The gene signature of YTHDC1, YTHDC2, and RBM15 was all determined by LASSO regression analysis (Figures 6(a) and 6(b)). Then, the ROC curve was used to determine the accuracy of the LASSO model by the AUC value. Consequently, the diagnostic accuracy (AUC) of YTHDC1, YTHDC2, and RBM15 for AD was 100, 96, and 100, respectively, in the GSE52093 dataset (Figure 6(c)).

3.6. Identification and Analysis of Key m6A Oxidative Stress-Related Genes. A total of six differentially m6A methylated DEGs regulated by m6A regulators were involved in oxidative stress function. Three of the genes also had the same trend of expression differences in GSE153434, namely, DHCR24, P4HB, and PDGFRA (Figure 7(a)). Three key genes were all upregulated in AD. The calibration curve indicated that the error between the actual AD risk and the predicted risk is very small, suggesting that the nomo-diagram-logistic model owns high accuracy to predict AD (Figures 7(b) and 7(c)). Decision curve analysis indicated that the nomo-diagram-logistic curve was higher than the gray line, "DHCR24" curve, "P4HB" curve, and "PDGFRA" curve (Figures 7(d) and 7(e)). Drugs that interact with P4HB and PDGFRA were found in DGIdb (Figure 8).

3.7. Correlations between DEMRGs and Immune Cells. The CIBERSORTx database is based on the expression matrix of GSE52093 and LM22 to analyze immune cell infiltration. The percentage of immune cells in each sample was

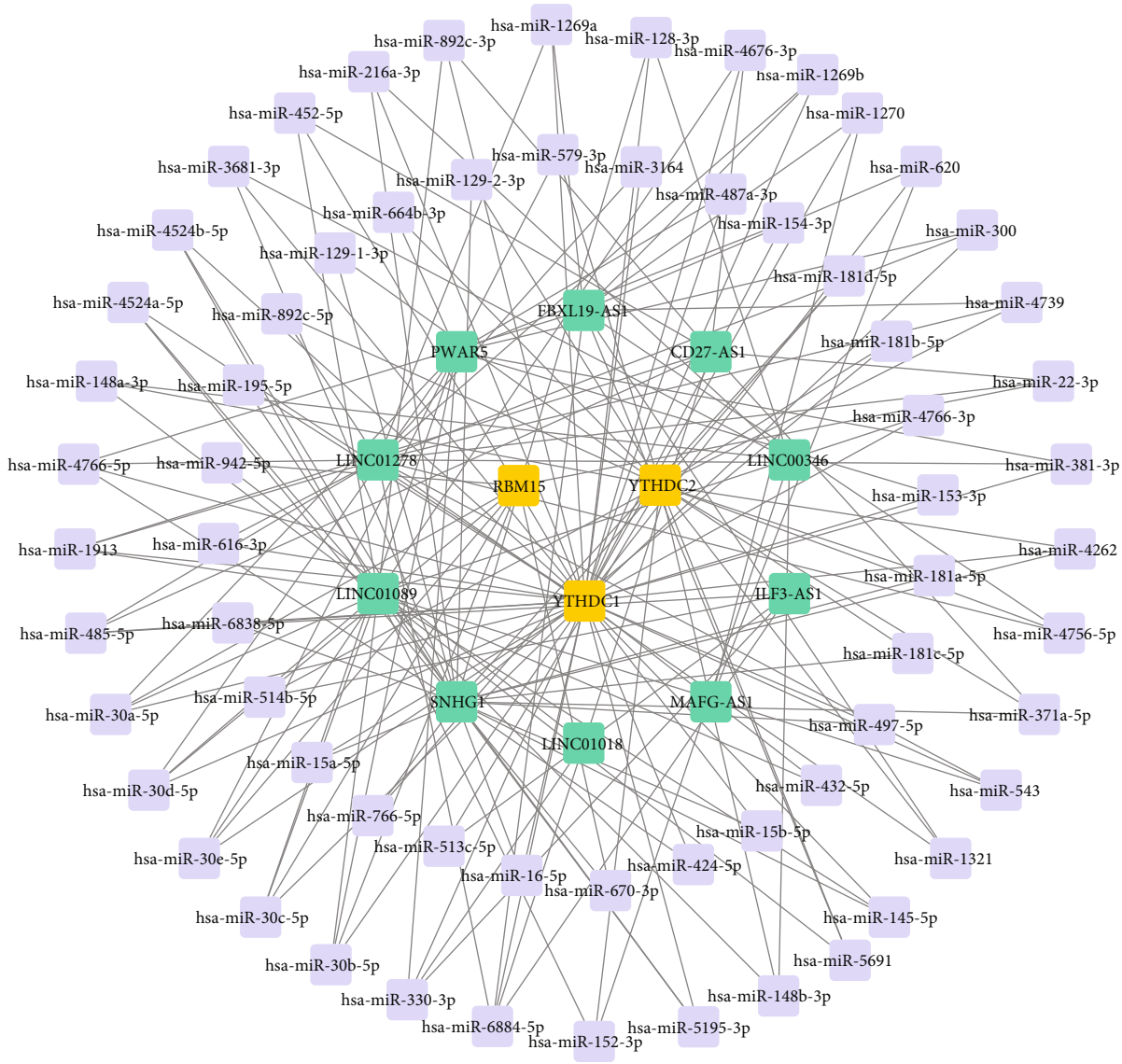

Figure 5: The ceRNA network of mRNA-miRNA-lncRNA for DEMRGs: yellow stands for DEMRGs, purple stands for miRNAs, and green stands for ceRNAs (lncRNAs).

evaluated (Supplementary File 2). According to the expression of DEMRGs and immune cell content in each sample, the correlation of DEMRGs and key genes with immune cells was calculated by the Pearson correlation analysis (Figures 9(a) and 9(b)). DHCR24 and P4HB were regulated by YTHDC1 and RBM15, and PDGFRA was regulated by YTHDC1 and YTHDC2 (Figure 9(c)). Then, the Pearson correlation between DEMRGs and key genes was also analyzed (Figure 9(d)).

3.8. Validation of DEMRGs in Human Aortic Tissue Level. We performed qRT-PCR to detect the mRNA expression of YTHDC1, YTHDC2, and RBM15 in human aorta specimens. The primer sequences are shown in Table 2. YTHDC1 and YTHDC2 mRNA was confirmed to be significantly downregulated in AD samples in comparison with control aortas. The P value of Mann–Whitney test of YTHDC1 and YTHDC2 was 0.0148 and 0.0499, respectively (Figure 10). We also detected the mRNA levels of other m6A regulators (YTHDF1, YTHDF2, YTHDF3, RRP8, ALKBF1, and ALKBF3) in aortic tissue by qRT-PCR (Supplementary File 3). We selectively performed western blot analysis for YTHDC1 in AD and normal aorta tissues. The blot images of YTHDC1 and its relative expression levels measured were displayed through western blotting in all samples (Figures 11(a) and 11(b)). The results of IF staining of paraffin sections of AD tissue showed that the fluorescent double staining of YTHDC1 and CD31 had obvious colocalization and often coexpressed in the same cell (Figure 12). At the same time, we noticed that YTHDC1 was expressed in the intima, media, and adventitia of AD, and CD31 was more expressed in the intima.

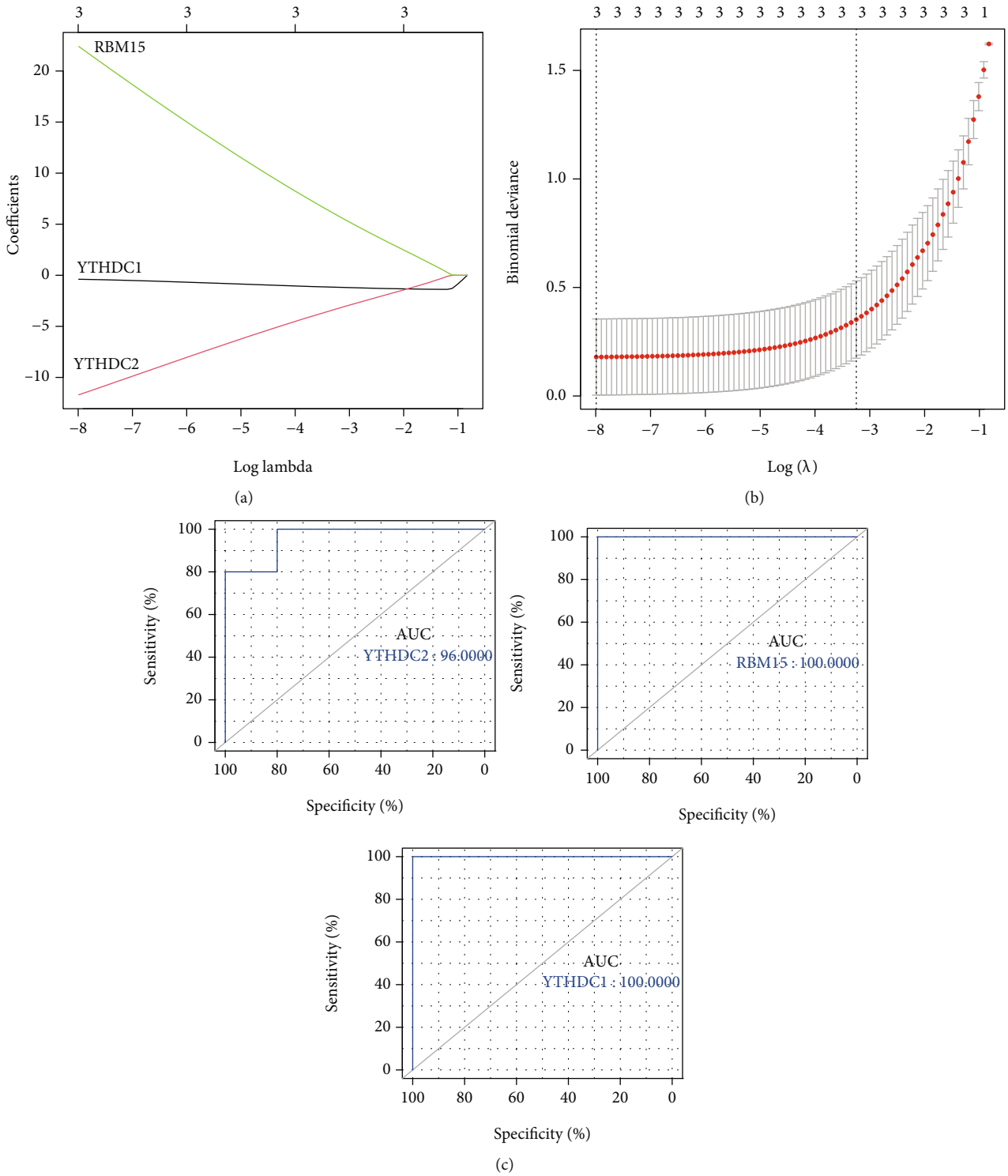

Figure 6: Identification of DEMRGs. (a) Coefficient plot of LASSO regression. (b) Cross verification curve of LASSO regression. (c) ROC curve analysis of DEMRGs.

3.9. Effect of YTHDC1 Knockdown on ROS Levels and Inflammation in HUVEC. The average knockdown efficiency of YTHDC1 detected by qRT-PCR was 73% (Figure 13(a)). Compared with that of the si-NC group, the signal intensity of the si-YTHDC1 group had a tendency to increase (Figure 13(b)). The decreased expression of YTHDC1 may lead to the increase of ROS. In qRT-PCR of human tissues, SOD2 expression was downregulated in AD (Supplementary File 4). Then, we found that the mRNA expression quantity of peroxide dismutase SOD2 was significantly reduced in the si-YTHDC1 groups compared with the si-NC groups (Figure 13(c)). In the same way, NOD2

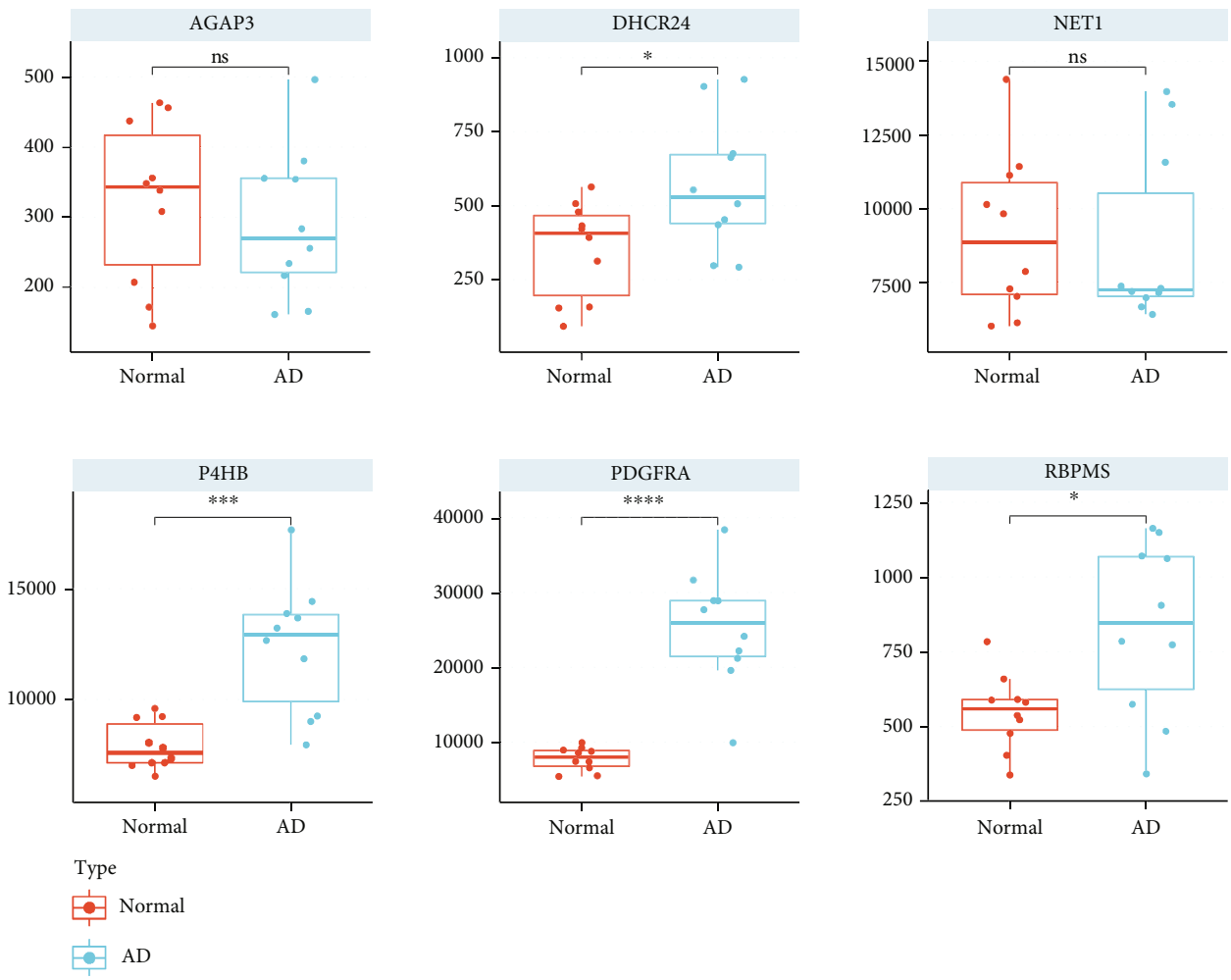

(a)

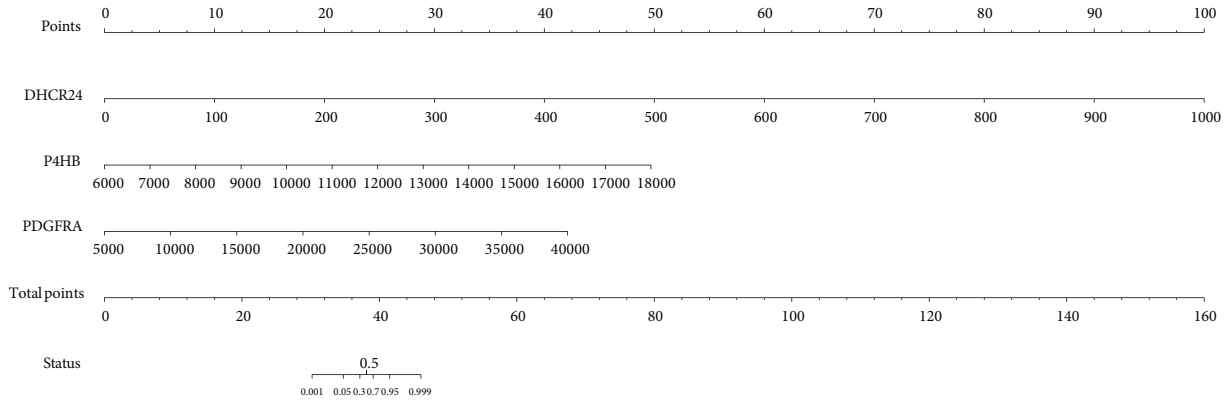

(b)

Figure 7: Continued.

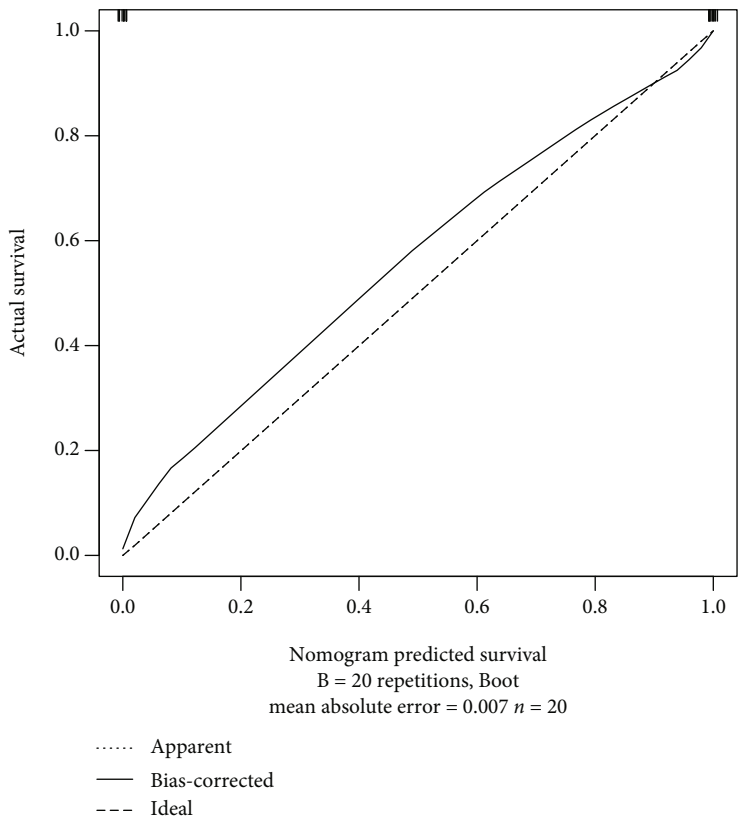

(c)

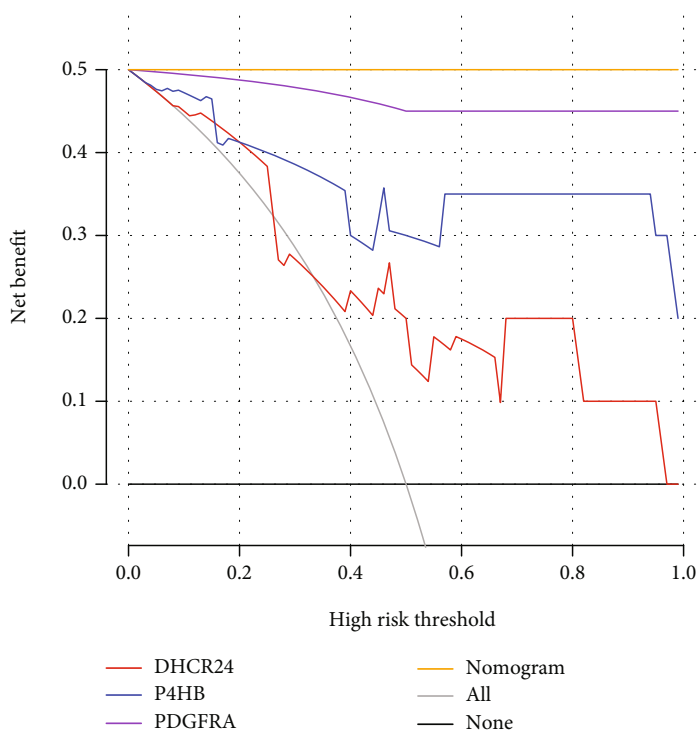

(d)

Figure 7: Continued.

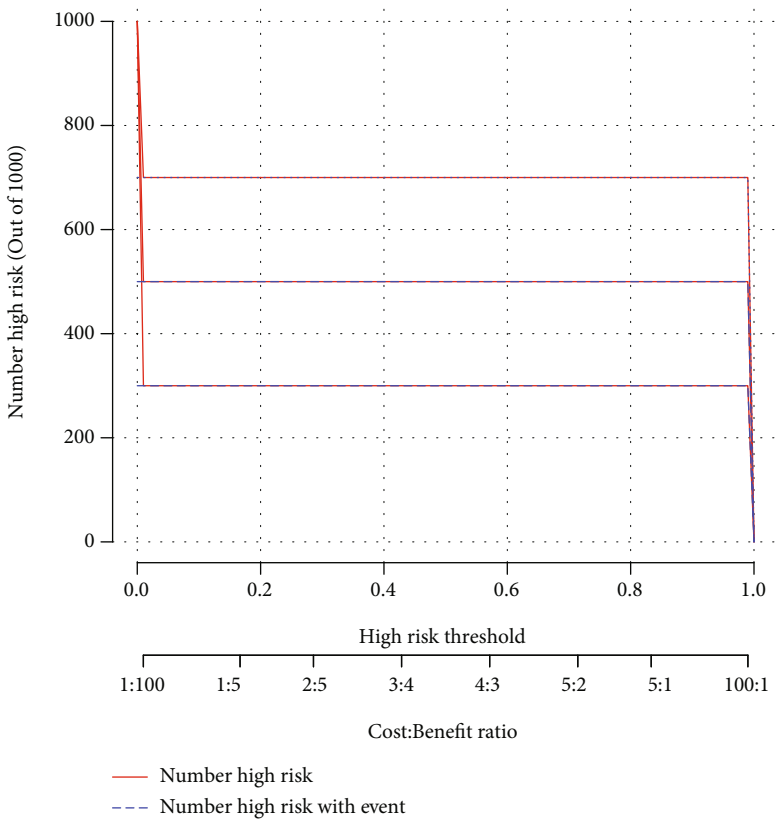

(e)

Figure 7: Identification of key m6A oxidative stress-related genes. (a) Boxplot of expression of key m6A oxidative stress-related genes in GSE153434: "*" means $P < 0.05$, "***" means $P < 0.001$, and "****" means $P < 0.0001$. (b) Nomo-diagram-logistic model. (c) Calibration curve analysis. (d) Decision curve analysis. (e) Clinical impact analysis.

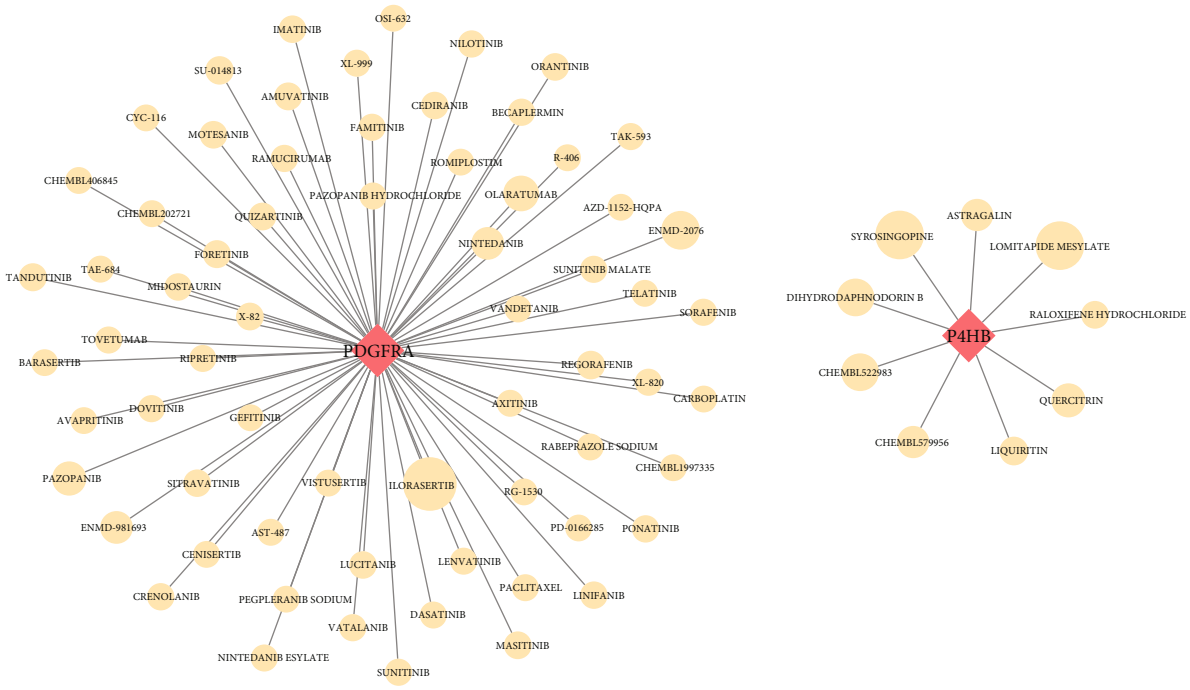

Figure 8: Interaction of drugs with P4HB and PDGFRA: the size of the shape represents the degree of interaction.

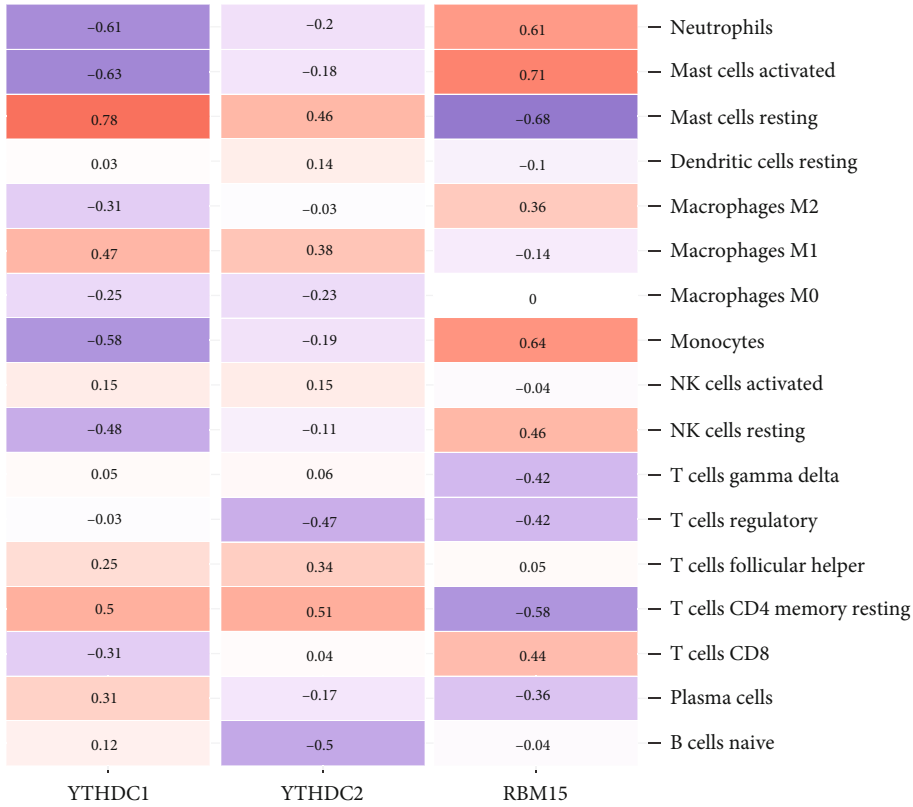

(a)

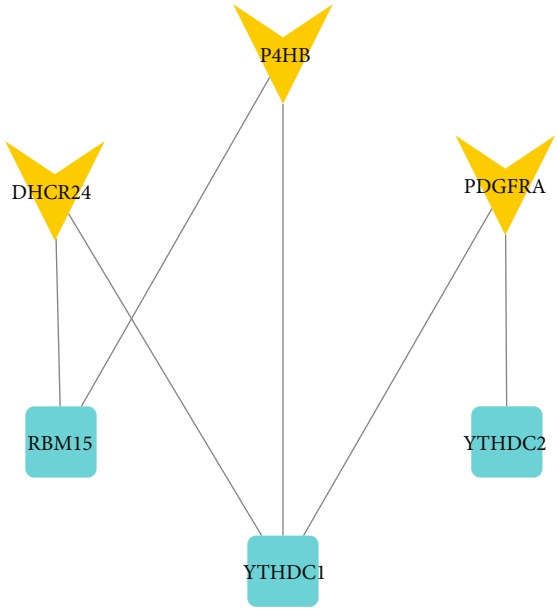

(b)

Figure 9: Continued.

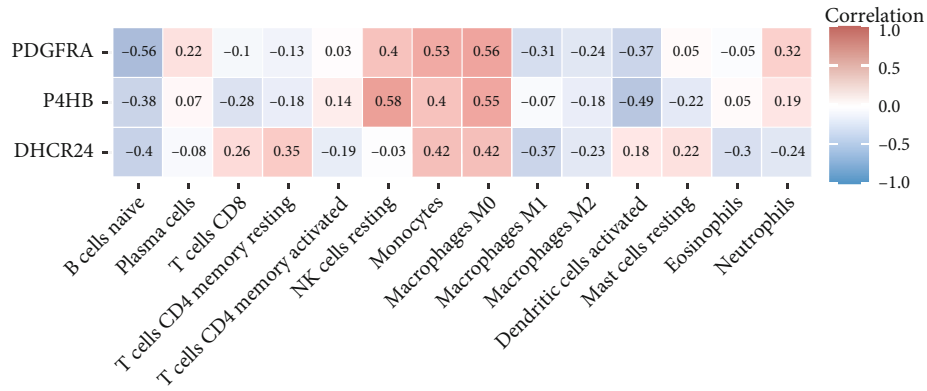

(c)

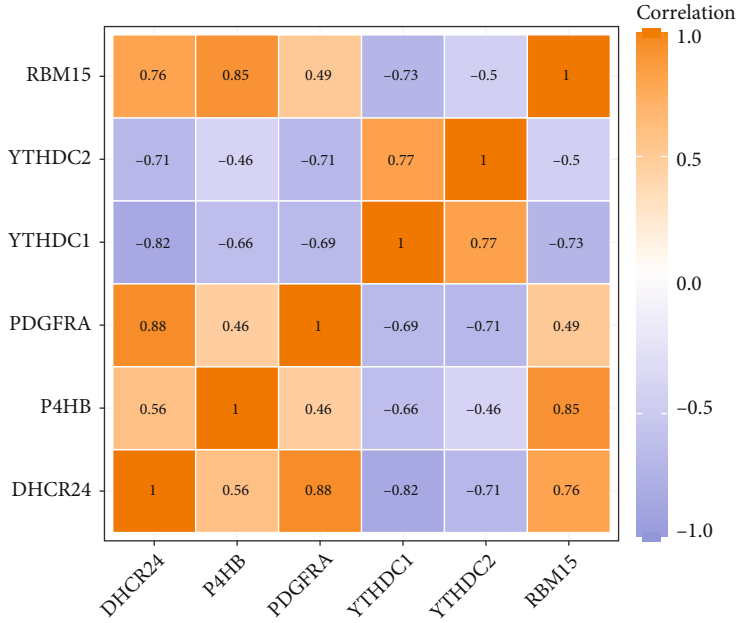

(d)

Figure 9: Correlations between genes and immune cells. (a) Correlation between DEMRGs and immune cells. (b) The correlation between key genes and immune cells. (c) The regulatory relationship between DEMRGs and key genes. (d) Correlation between DEMRGs and key genes.

expression was significantly increased after YTHDC1 knockdown, but NLPR3 moved towards low expression (Figure 13(d)).

4. Discussion

Although many studies have demonstrated that m6A methylation and oxidative stress play an important role in the occurrence of CVDs, the molecular mechanism of their joint effect on AD is rarely reported. Based on AD samples and normal aortic samples, we used bioinformatics and molecular biology experimental methods to study the potential molecular mechanism of m6A and oxidative stress in AD. Three DEMRGs in AD tissue and normal aortic tissue were analyzed by the GSE52093 dataset. YTHDC1 and YTHDC2 were downregulated in AD, while RBM15 was upregulated. Subsequent ROC analysis also showed that YTHDC1, YTHDC2, and RBM15 have good diagnostic capabilities. We found DEGs regulated by three DEMRGs, and then, the function and pathway enrichment of these genes were analyzed. Cell division and viral process in biological process were more prominent. The cellular components in which they reside were abundantly enriched in the nucleoplasm, nucleus, and cytoplasm. Molecular functions mainly included poly(A) RNA binding and ATP binding. KEGG enrichment results showed that these genes were involved in the periodic division of cells. According to the DE-lncRNAs and DEMRGs in GSE52093 to predict miRNAs, the ceRNA-miRNA-mRNA relationship chain was obtained, and the ceRNA network was constructed. The oxidative stress-related genes were obtained from the GO database, and DEGs regulated by DEMRGs with oxidative stress-related functions were obtained through Venn diagram analysis. Then, the protein interaction network of these genes was constructed, and the upregulated genes with high degree values such as TP53 and SOD2 were found. Three of these

Table 2: qRT-PCR primer sequences.

Gene	Primer	Sequence (5′ to 3′)
YTHDC1	Forward primer	TCT TCC GTT CGT GCT GTC C
	Reverse primer	GGA CCA TAC ACC CTT CGC TT
YTHDC2	Forward primer	GAG AAT TGG GCT GTC GTT AAA G
	Reverse primer	TGA AGC AGG ATG AAA TCG TAC T
RBM15	Forward primer	CCT TGT GAG TTC TCC CAG CAG TTC
	Reverse primer	GGA CGC ACC ACG GAC AAT GAT C
YTHDF1	Forward primer	TGG ACA CCC AGA GAA CAA AAG G
	Reverse primer	TGA GGT ATG GAA TCG GAG GGT
YTHDF2	Forward primer	AGT GTC AGG GAC AAA AGC CTC C
	Reverse primer	TTT TGG TCT CTG CTC CAA GAG G
YTHDF3	Forward primer	TAG GGA GTC TGT CCG CCA TT
	Reverse primer	GAC ATT CTT CAC CGC AAC CC
RRP8	Forward primer	CAG TGG TAA GAG GTT GCT CCA T
	Reverse primer	TGG TAT GCT CTT CCC TCT GC
ALKBH3	Forward primer	AGA GAA CCG AGA GTC AAC CTG ACC
	Reverse primer	CTA GCA GCA CCA GCC TCT TGA AG
ALKBH1	Forward primer	TCA GCA GAT CAT TAC ACA CCT T
	Reverse primer	CTA GCT CAG ATC TGT CTA CGT G

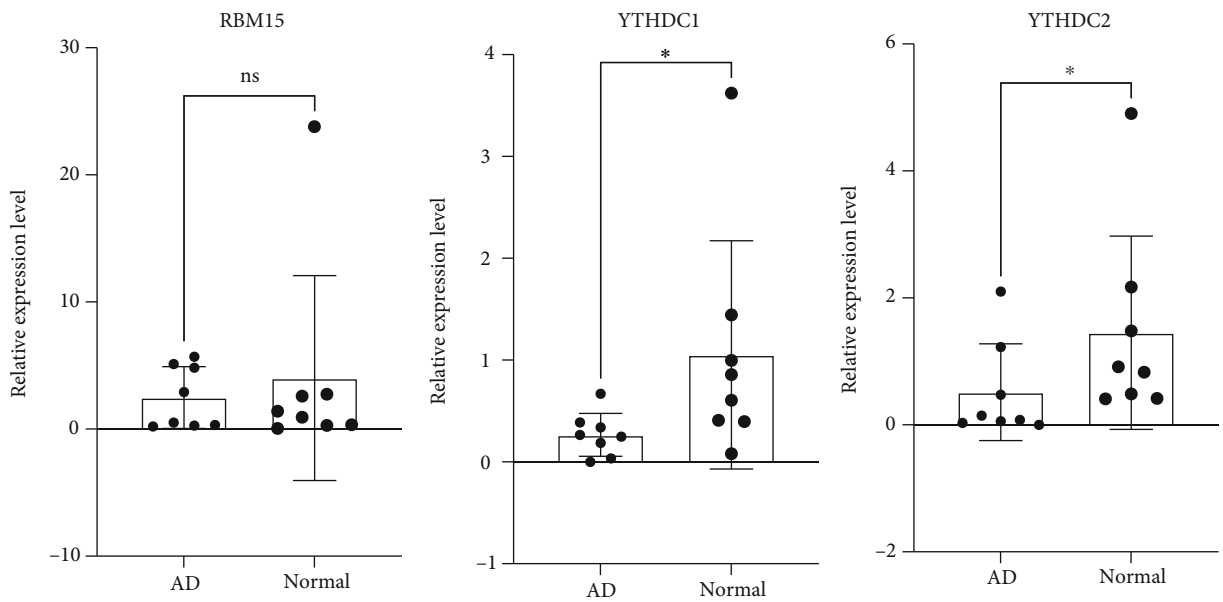

Figure 10: Human aortic tissue validation, qRT-PCR results of DEMRGs: "*" means $P < 0.05$.

genes were significantly different in the degree of m6A methylation in AD and normal tissues, namely, DHCR24, P4HB, and PDGFRA, and they were significantly upregulated in two different datasets. In the gene-cell correlation analysis, both YTHDC1 and RBM15 were strongly associated with resting and activated mast cells, and DHCR24, P4HB, and PDGFRA were generally associated with macrophage M0. Finally, we found that the expression of YTHDC1 was obvious in endothelial cells, and the decreased expression of YTHDC1 had an effect on ROS.

The molecular mechanism of m6A regulators is the core of the scientific question of this study. YTHDC1, whose full name is YTH domain containing 1, is a type of m6A "reader" protein. Roundtree et al. found that YTHDC1 mediates nuclear-to-cytoplasmic transport of m6A methylated mRNAs. They knocked down YTHDC1, which resulted

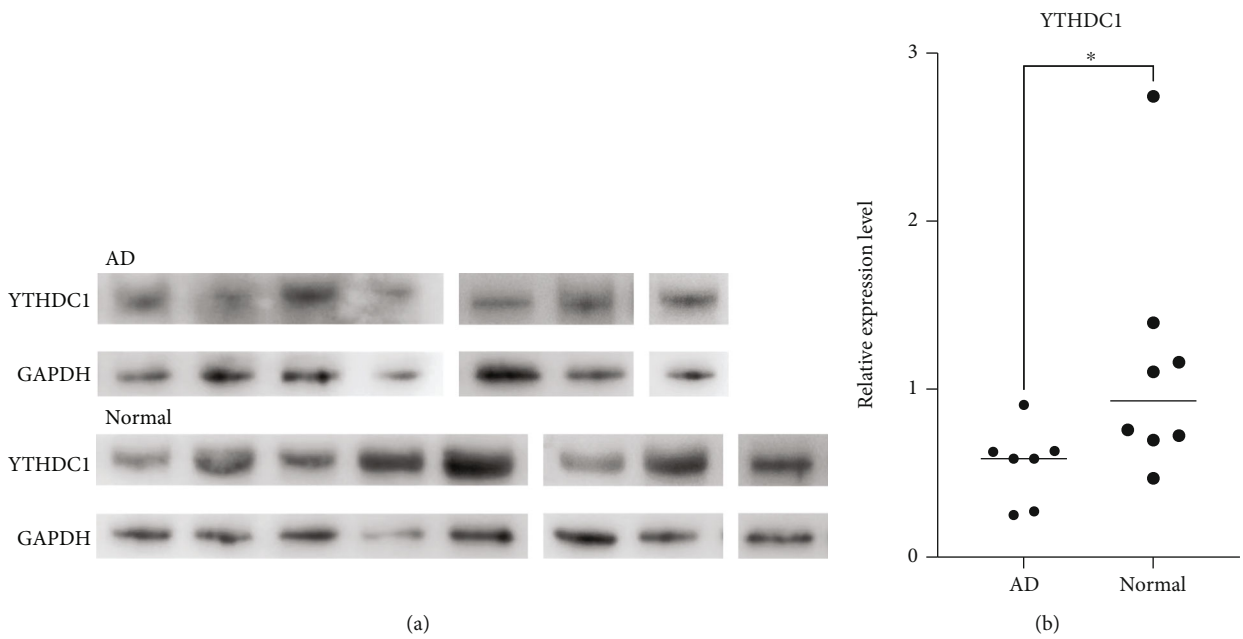

Figure 11: Human aortic tissue validation, WB results of YTHDC1. (a) Western blot in AD and normal. (b) Significance test of difference: "*" means $P < 0.05$.

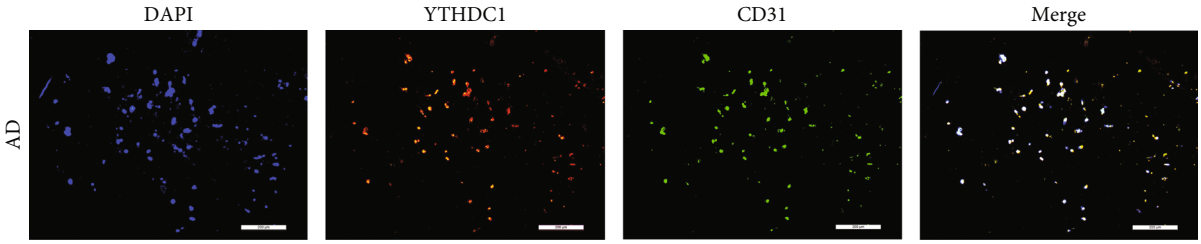

Figure 12: IF staining of DAPI, YTHDC1, and CD31 and their merged images.

in boosted signal intensity around the nuclear region and decreased in the cytoplasmic region [31]. This suggests that YTHDC1 plays an active role in nuclear mRNA export. They also found that overexpression of YTHDC1 reduced m6A levels of nuclear mRNA, whereas our study found that YTHDC1 was underexpressed in AD, in line with the conclusion that m6A levels are elevated in AD. Gao et al. demonstrated in a mouse model that Ythdc1 knockout resulted in left ventricular enlargement and systolic dysfunction, as well as decreased cardiomyocyte contractility and disordered sarcomere arrangement at the cellular level [32]. YTHDC1 affects mRNA splicing through recruitment and regulation of pre-mRNA splicing factors, which may be the underlying cause of aberrant splicing of titin in Ythdc1-deficient cardiomyocytes and thus aberrant sarcomere contraction [33]. m6A modification of Ythdc1 directs promoter-proximal RNA polymerase II to suspend work, which is also critical for precise control of gene expression [34]. YTHDC2 contains multiple domains that can bind to RNAs with different nucleotide preferences, and when YTHDC2 binds to RNA helicase, m6A modification of the coding region can promote the translation of structured mRNA [35, 36]. In the YTH-binding domains of YTHDC1 and YTHDC2, a1, a2, and the coils preceding a1, a2, and b4 could constitute the m6A-binding pocket that can recognize cavity-inserted methyl groups, and the m6A-binding surface is highly conserved in evolution, compared to other YTH domains [37, 38]. This is an important molecular mechanism of YTH domain binding to m6A nucleotides. As a special RNA-binding protein, m6A methyltransferase RBM15 plays an important role in cell growth and apoptosis by regulating various signaling pathways such as Notch and Wnt [39]. However, the role of RBM15 in CVDs was rarely reported, and only a few studies linked it to some blood disorders.

GO-BP results showed that these genes were extensively involved in cell cycle-related processes, as well as Wnt signaling pathway and planar cell polarity pathway. A bioinformatics study found that cell cycle-related genes were significantly upregulated in thoracic aortic aneurysm and dissection tissues in a mouse model, and they were essential for cell proliferation [40]. In response to changes in the local vascular environment, vascular smooth muscle cells proliferate to alter the differentiation/contraction phenotype [41]. These genes might play a role in VSMC proliferation and phenotypic changes. The Wnt signaling pathway may be involved in ventricular hypertrophy, and the planar cell

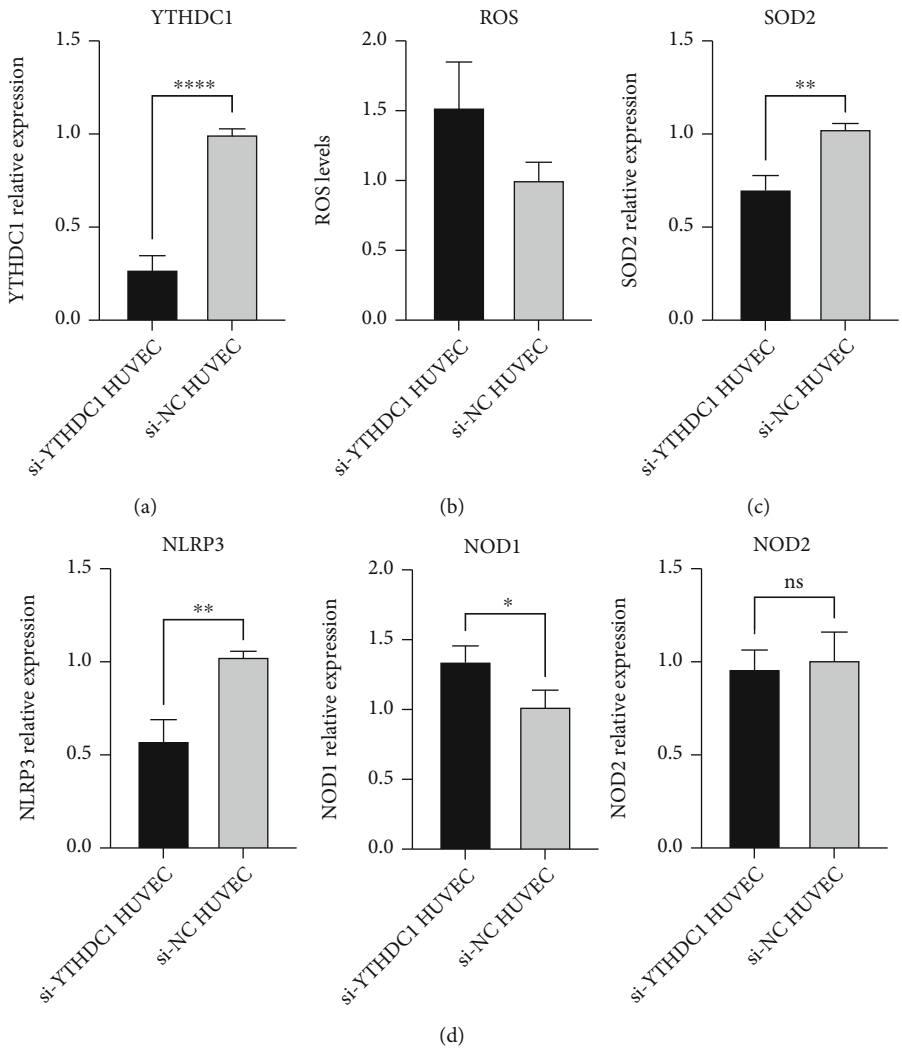

Figure 13: Effects of YTHDC1 on ROS and inflammation. "*" means $P < 0.05$, "**" means $P < 0.01$, and "****" means $P < 0.0001$. (a) YTHDC1 knockdown efficiency. (b) ROS levels of the si-YThDC1 groups and si-NC groups. (c) SOD2 relative expression of the si-YTHDC1 groups and si-NC groups. (d) PRR (NOD1, NOD2, and NLRP3) relative expression of the si-YTHDC1 groups and si-NC groups.

polarity pathway has the function of regulating the morphology of polarization, helping the development of the poles of the arteries and veins of the heart [42, 43]. As indicated by GO-CC, these DEGs are mainly enriched around the nucleoplasm or nucleus. This is strongly associated with nuclear mRNA export of YTHDC1. These DEGs were also enriched for molecular functions related to transcription, such as damaged DNA, ATP, transcription factor, poly(A) RNA, and RNA binding. KEGG analysis also showed their high correlation with cell cycle.

In our study, we found three oxidative stress-related DEGs with m6A differences and regulated by DEMRGs, namely, DHCR24, P4HB, and PDGFRA. DHCR24 plays a vital role in lipid metabolism and is an enzyme that catalyzes conversion of the bioactive metabolite desmosterol to cholesterol [44]. Desmosterol is an endogenous agonist of the liver X receptor which plays an important role in the regulation of lipid metabolism and is involved in atherosclerosis and inflammation. Inhibition of DHCR24 leads to accumulation of desmosterol, and depletion of desmosterol in myeloid cells by overexpression of DHCR24 promotes the progression of atherosclerosis [45, 46]. DHCR24 is also one of the host markers of oxidative stress, and it has been reported that the expression of DHCR24 was upregulated in the acute response to oxidative stress and, in contrast, downregulated in the chronic response [47, 48]. High expression of DHCR24 gene is associated with apoptosis induced by antioxidative stress [49]. P4HB protein is an endoplasmic reticulum molecular chaperone that contributes to the maintenance of endoplasmic reticulum protein homeostasis [50]. PDIA1 encoded by it participates in vascular redox cell signaling. The expression of P4HB splice variants was elevated in smooth muscle cells, especially isoforms P4HB-02 and P4HB-021 [51]. Increased P4HB expression was also produced in the serum of the Kawasaki disease causing systemic vasculitis [52]. A possible effect of P4hb in regulating oxidative stress in middle cerebral ischemia/reperfusion has been reported in mouse models [53].

PDGFRA has a relevant functional role in vascular remodeling; its expression can characterize aortic-derived telocytes, and telocyte-mediated regulation of aortic remodeling may promote aortic repair and prevent adverse remodeling [54, 55]. In mouse model studies, it was demonstrated that PDGFRA cell populations were functionally capable of promoting differentiation into cardiomyocytes, and silencing of PDGFRA suppressed this ability [56]. We found that PDGFRA was highly correlated with ILORASERTIB in drug interactions. ILORASERTIB is an ATP-competitive, multitargeted kinase inhibitor that inhibits cellular autophosphorylation [57]. cGMP-dependent protein kinase 1 (PKG1) can help regulate vascular tone and smooth muscle cell phenotype, and cGMP-PKG1 increases the degree of autophosphorylation in PRKG1 gene mutations that cause thoracic AD [58].

In the analysis of the correlation between DEMRGs and immune cells, we found that YTHDC1 was positively correlated with macrophage M1 and negatively correlated with macrophage M2, and it was also positively correlated with resting mast cells and negatively correlated with activated mast cells. The presence of aortic inflammatory cell infiltration and elastic fiber destruction in AD undoubtedly highlights the involvement of macrophages [59]. M1 macrophages can promote inflammation, while M2 macrophages can eliminate inflammation [60]. Macrophages are central to aortic wall inflammation, and angiotensin II regulates macrophages leading to AD development. Thrombospondin 1, which can be induced by angiotensin II, is markedly elevated in AD patients and may be involved in AD by promoting M1 macrophage planning and vascular smooth muscle apoptosis [61, 62]. M2 macrophages act as a protective factor with phenotype repair cell function in the study of blood blister-like aneurysms [63]. Macrophages may not only participate in the onset of AD but also in the repair of AD. m6A methylation modifies and facilitates macrophage pyroptosis and inflammation in atherosclerosis [64]. Another study found that important m6A "writers"-METTL3 promote M1 macrophage programming through m6A methylation [65]. Therefore, whether YTHDC1 can induce the polarization of M0 macrophages is a question worthy of our further study.

Elevated ROS levels are a feature of most vascular diseases, and their occurrence in endothelial cells has been found to contribute to susceptibility to aortic dissection [66]. As a manganese-containing superoxide dismutase located in mitochondria, SOD2 scavenge ROS to protect cells from oxidative stress [67]. Our conclusion found that the downregulation of YTHDC1 may cause the increase of ROS level and the decrease of SOD2 expression, which was consistent with the above molecular mechanism. Therefore, the decreased expression of YTHDC1 may disrupt the homeostasis of endothelial cells. However, the specific mechanism of ROS elevation and the influence of other factors on ROS in AD need to be further studied.

This study is aimed at providing help in discovering the role of m6A regulators in AD, but our findings still need more in vivo experiments to confirm and further research to explore deeper molecular mechanisms.

5. Conclusions

YTHDC1, YTHDC2, and RBM15, as m6A regulators, had significant differences in expression in AD. m6A methylation and oxidative stress mediated by these three factors may be associated with the onset of AD. Among them, YTHDC1 was also found to be related to the polarization of macrophages and the activation of mast cells in correlation with immune cells. We also verified the significant downregulation of YTHDC1 and YTHDC2 in subsequent human tissues including AD tissue and healthy aortic tissue. In addition, we found three oxidative stress-related DEGs with differential m6A modification, namely, DHCR24, P4HB, and PDGFRA. The expression of YTHDC1 in endothelial cells was verified by IF, and the ROS level increased after the expression of YTHDC1 decreased, while the expression of SOD2 decreased. These findings may further advance the discovery of the molecular mechanisms of AD, helping to aid subsequent research and the development of treatments.

Data Availability

The datasets used or analyzed during the current study are available from the corresponding author on reasonable request. The names of the repository/repositories and accession number(s) can be found in the article/Supplementary Material.

Conflicts of Interest

The authors declare that they have no conflict of interests.

Authors' Contributions

Fanxing Yin and Kun Liu contributed equally.

Acknowledgments

We would like to thank the Gene Expression Omnibus (GEO) database for the precious data used for free in the scientific research. This work was supported by the Fundamental Research Funds for the Central Universities (grant number: DUT22YG107), the National Natural Science Foundation of China (grant numbers: 82260100 and 81600370), and the China Postdoctoral Science Foundation (grant number: 2018M640270).

Supplementary Materials

Supplementary material 1: differential expression analysis of genes in GSE52093. Supplementary material 2: immune infiltration analysis of GSE52093. Supplementary material 3: qRT-PCR results of additional m6A regulators (YTHDF1, YTHDF2, YTHDF3, RRP8, ALKBF1, and ALKBF3) in human aortic dissection tissue and healthy aortic tissue, "*" represents $P < 0.05$; "***" represents $P < 0.001$. Supplementary material 4: the mRNA expression of SOD2 in human AD samples and normal samples. *(Supplementary Materials)*

References

[1] K. Buivydaite, V. Semenaite, J. Brazdzionyte, and A. Macas, "Aortic dissection," *Medicina*, vol. 44, no. 3, pp. 247–255, 2008.

[2] P. Chiu and D. C. Miller, "Evolution of surgical therapy for Stanford acute type A aortic dissection," *Annals of Cardiothoracic Surgery*, vol. 5, no. 4, pp. 275–295, 2016.

[3] A. Sayed, M. Munir, and E. I. Bahbah, "Aortic dissection: a review of the pathophysiology, management and prospective advances," *Current Cardiology Reviews*, vol. 17, no. 4, article e230421186875, 2021.

[4] T. Zeng, L. Shi, Q. Ji et al., "Cytokines in aortic dissection," *Clinica Chimica Acta*, vol. 486, pp. 177–182, 2018.

[5] E. Allaire, F. Schneider, F. Saucy et al., "New insight in aetiopathogenesis of aortic diseases," *European Journal of Vascular and Endovascular Surgery*, vol. 37, no. 5, pp. 531–537, 2009.

[6] E. Niinimak, V. Pynnonen, I. Kholova, T. Paavonen, and A. Mennander, "Neovascularization with chronic inflammation characterizes ascending aortic dissection," *Anatolian Journal of Cardiology*, vol. 20, no. 5, pp. 289–295, 2018.

[7] V. Tchana-Sato, N. Sakalihasan, and J. O. Defraigne, "Aortic dissection," *Revue Médicale de Liège*, vol. 73, no. 5-6, pp. 290–295, 2018.

[8] J. Gawinecka, F. Schonrath, and A. von Eckardstein, "Acute aortic dissection: pathogenesis, risk factors and diagnosis," *Swiss Medical Weekly*, vol. 147, article w14489, 2017.

[9] A. S. Jassar and T. M. Sundt III, "How should we manage type A aortic dissection?," *General Thoracic and Cardiovascular Surgery*, vol. 67, no. 1, pp. 137–145, 2019.

[10] H. Gao, X. Sun, Y. Liu et al., "Analysis of hub genes and the mechanism of immune infiltration in Stanford type a aortic dissection," *Front Cardiovasc Med.*, vol. 8, article 680065, 2021.

[11] A. S. Beam and K. Moore, "Familial thoracic aortic dissection," *Radiologic Technology*, vol. 92, no. 5, pp. 428–434, 2021.

[12] J. Tong, R. A. Flavell, and H. B. Li, "RNA m6A modification and its function in diseases," *Frontiers in Medicine*, vol. 12, no. 4, pp. 481–489, 2018.

[13] C. Zhang, J. Fu, and Y. Zhou, "A review in research progress concerning m6A methylation and immunoregulation," *Frontiers in Immunology*, vol. 10, p. 922, 2019.

[14] Y. Qin, L. Li, E. Luo et al., "Role of m6A RNA methylation in cardiovascular disease (review)," *International Journal of Molecular Medicine*, vol. 46, no. 6, pp. 1958–1972, 2020.

[15] J. Lin, Q. Zhu, J. Huang, R. Cai, and Y. Kuang, "Hypoxia promotes vascular smooth muscle cell (VSMC) differentiation of adipose-derived stem cell (ADSC) by regulating Mettl3 and paracrine factors," *Stem Cells International*, vol. 2020, Article ID 2830565, 11 pages, 2020.

[16] S. Zaccara, R. J. Ries, and S. R. Jaffrey, "Reading, writing and erasing mRNA methylation," *Nature Reviews. Molecular Cell Biology*, vol. 20, no. 10, pp. 608–624, 2019.

[17] M. Lee, B. Kim, and V. N. Kim, "Emerging roles of RNA modification: m^6A and U-tail," *Cell*, vol. 158, no. 5, pp. 980–987, 2014.

[18] L. He, H. Li, A. Wu, Y. Peng, G. Shu, and G. Yin, "Functions of N6-methyladenosine and its role in cancer," *Molecular Cancer*, vol. 18, no. 1, p. 176, 2019.

[19] L. Hu, J. Wang, H. Huang et al., "YTHDF1 regulates pulmonary hypertension through translational control of MAGED1," *American Journal of Respiratory and Critical Care Medicine*, vol. 203, no. 9, pp. 1158–1172, 2021.

[20] Z. Han, X. Wang, Z. Xu et al., "ALKBH5 regulates cardiomyocyte proliferation and heart regeneration by demethylating the mRNA of YTHDF1," *Theranostics*, vol. 11, no. 6, pp. 3000–3016, 2021.

[21] D. Jian, Y. Wang, L. Jian et al., "METTL14 aggravates endothelial inflammation and atherosclerosis by increasing FOXO1 N6-methyladeosine modifications," *Theranostics*, vol. 10, no. 20, pp. 8939–8956, 2020.

[22] X. Zhou, Z. Chen, J. Zhou, Y. Liu, R. Fan, and T. Sun, "Transcriptome and N6-methyladenosine RNA methylome analyses in aortic dissection and normal human aorta," *Frontiers in Cardiovascular Medicine*, vol. 8, article 627380, 2021.

[23] A. van der Pol, W. H. van Gilst, A. A. Voors, and P. van der Meer, "Treating oxidative stress in heart failure: past, present and future," *European Journal of Heart Failure*, vol. 21, no. 4, pp. 425–435, 2019.

[24] R. Rodrigo, J. Gonzalez, and F. Paoletto, "The role of oxidative stress in the pathophysiology of hypertension," *Hypertension Research*, vol. 34, no. 4, pp. 431–440, 2011.

[25] T. Senoner and W. Dichtl, "Oxidative stress in cardiovascular diseases: still a therapeutic target?," *Nutrients*, vol. 11, no. 9, p. 2090, 2019.

[26] N. Sinha and P. K. Dabla, "Oxidative stress and antioxidants in hypertension-a current review," *Current Hypertension Reviews*, vol. 11, no. 2, pp. 132–142, 2015.

[27] A. Magenta, S. Greco, C. Gaetano, and F. Martelli, "Oxidative stress and microRNAs in vascular diseases," *International Journal of Molecular Sciences*, vol. 14, no. 9, pp. 17319–17346, 2013.

[28] B. Yang and Q. Chen, "Cross-talk between oxidative stress and m^6A RNA methylation in cancer," *Oxidative Medicine and Cellular Longevity*, vol. 2021, Article ID 6545728, 26 pages, 2021.

[29] X. Li, Y. Jiang, X. Sun, Y. Wu, and Z. Chen, "METTL3 is required for maintaining β-cell function," *Metabolism*, vol. 116, article 154702, 2021.

[30] P. B. Chen, G. X. Shi, T. Liu et al., "Oxidative stress aggravates apoptosis of nucleus pulposus cells through m^6A modification of MAT2A pre-mRNA by METTL16," *Oxidative Medicine and Cellular Longevity*, vol. 2022, Article ID 4036274, 15 pages, 2022.

[31] I. A. Roundtree, G. Z. Luo, Z. Zhang et al., "YTHDC1 mediates nuclear export of N6-methyladenosine methylated mRNAs," *eLife*, vol. 6, p. 6, 2017.

[32] S. Gao, H. Sun, K. Chen et al., "Depletion of m6A reader protein YTHDC1 induces dilated cardiomyopathy by abnormal splicing of Titin," *Journal of Cellular and Molecular Medicine*, vol. 25, no. 23, pp. 10879–10891, 2021.

[33] W. Xiao, S. Adhikari, U. Dahal et al., "Nuclear m^6A reader YTHDC1 regulates mRNA splicing," *Molecular Cell*, vol. 61, no. 4, pp. 507–519, 2016.

[34] J. Akhtar, Y. Renaud, S. Albrecht et al., "m^6A RNA methylation regulates promoter- proximal pausing of RNA polymerase II," *Molecular Cell*, vol. 81, no. 16, pp. 3356–3367.e6, 2021.

[35] D. P. Patil, C. K. Chen, B. F. Pickering et al., "m^6A RNA methylation promotes _XIST_ -mediated transcriptional repression," *Nature*, vol. 537, no. 7620, pp. 369–373, 2016.

[36] Y. Mao, L. Dong, X. M. Liu et al., "m^6A in mRNA coding regions promotes translation via the RNA helicase-containing YTHDC2," *Nature Communications*, vol. 10, no. 1, p. 5332, 2019.

[37] C. Ma, S. Liao, and Z. Zhu, "Crystal structure of human YTHDC2 YTH domain," *Biochemical and Biophysical Research Communications*, vol. 518, no. 4, pp. 678–684, 2019.

[38] X. Y. Dai, L. Shi, Z. Li, H. Y. Yang, J. F. Wei, and Q. Ding, "Main N6-methyladenosine readers: YTH family proteins in cancers," *Frontiers in Oncology*, vol. 11, article 635329, 2021.

[39] M. Hu, Y. Yang, Z. Ji, and J. Luo, "RBM15 functions in blood diseases," *Current Cancer Drug Targets*, vol. 16, no. 7, pp. 579–585, 2016.

[40] X. Zhang, Z. Yang, X. Li et al., "Bioinformatics analysis reveals cell cycle-related gene upregulation in ascending aortic tissues from murine models," *Frontiers in Genetics*, vol. 13, article 823769, 2022.

[41] A. Frismantiene, M. Philippova, P. Erne, and T. J. Resink, "Smooth muscle cell-driven vascular diseases and molecular mechanisms of VSMC plasticity," *Cellular Signalling*, vol. 52, pp. 48–64, 2018.

[42] D. Li and J. Wang, "Planar cell polarity signaling in mammalian cardiac morphogenesis," *Pediatric Cardiology*, vol. 39, no. 5, pp. 1052–1062, 2018.

[43] S. M. Yuan, "Institute name," *Revista Brasileira de Cirurgia Cardiovascular*, vol. 27, no. 1, p. 173, 2012.

[44] E. J. Zerenturk, L. J. Sharpe, E. Ikonen, and A. J. Brown, "Desmosterol and DHCR24: unexpected new directions for a terminal step in cholesterol synthesis," *Progress in Lipid Research*, vol. 52, no. 4, pp. 666–680, 2013.

[45] C. Muller, E. Hank, M. Giera, and F. Bracher, "Dehydrocholesterol reductase 24 (DHCR24): medicinal chemistry, pharmacology and novel therapeutic options," *Current Medicinal Chemistry*, vol. 29, no. 23, pp. 4005–4025, 2022.

[46] X. Zhang, J. G. McDonald, B. Aryal et al., "Desmosterol suppresses macrophage inflammasome activation and protects against vascular inflammation and atherosclerosis," *Proceedings of the National Academy of Sciences of the United States of America*, vol. 118, no. 47, 2021.

[47] K. Rebbani and K. Tsukiyama-Kohara, "HCV-induced oxidative stress: battlefield-winning strategy," *Oxidative Medicine and Cellular Longevity*, vol. 2016, Article ID 7425628, 7 pages, 2016.

[48] K. Kuehnle, A. Crameri, R. E. Kälin et al., "Prosurvival effect of DHCR24/Seladin-1 in acute and chronic responses to oxidative stress," *Molecular and Cellular Biology*, vol. 28, no. 2, pp. 539–550, 2008.

[49] D. Di Stasi, V. Vallacchi, V. Campi et al., "*DHCR24* gene expression is upregulated in melanoma metastases and associated to resistance to oxidative stress-induced apoptosis," *International Journal of Cancer*, vol. 115, no. 2, pp. 224–230, 2005.

[50] Y. Wu, Y. Peng, B. Guan et al., "P4HB: a novel diagnostic and prognostic biomarker for bladder carcinoma," *Oncology Letters*, vol. 21, no. 2, p. 95, 2021.

[51] D. Kajihara, C. C. Hon, A. N. Abdullah et al., "Analysis of splice variants of the human protein disulfide isomerase (P4HB) gene," *BMC Genomics*, vol. 21, no. 1, p. 766, 2020.

[52] M. Xu, Q. Qi, L. Men et al., "Berberine protects Kawasaki disease-induced human coronary artery endothelial cells dysfunction by inhibiting of oxidative and endoplasmic reticulum stress," *Vascular Pharmacology*, vol. 127, article 106660, 2020.

[53] Q. Ma, C. Wang, M. Wang et al., "Investigation of brain damage mechanism in middle cerebral artery occlusion/reperfusion rats based on i-TRAQ quantitative proteomics," *Experimental Brain Research*, vol. 239, no. 4, pp. 1247–1260, 2021.

[54] B. Liu, M. Pjanic, T. Wang et al., "Genetic regulatory mechanisms of smooth muscle cells map to coronary artery disease risk loci," *American Journal of Human Genetics*, vol. 103, no. 3, pp. 377–388, 2018.

[55] T. Aschacher, K. Schmidt, O. Aschacher et al., "Telocytes in the human ascending aorta: characterization and exosome-related KLF-4/VEGF-A expression," *Journal of Cellular and Molecular Medicine*, vol. 25, no. 20, pp. 9697–9709, 2021.

[56] B. J. Kim, Y. H. Kim, Y. A. Lee et al., "Platelet-derived growth factor receptor-alpha positive cardiac progenitor cells derived from multipotent germline stem cells are capable of cardiomyogenesis in vitro and in vivo," *Oncotarget*, vol. 8, no. 18, pp. 29643–29656, 2017.

[57] K. B. Glaser, J. Li, P. A. Marcotte et al., "Preclinical characterization of ABT-348, a kinase inhibitor targeting the aurora, vascular endothelial growth factor receptor/platelet-derived growth factor receptor, and Src kinase families," *The Journal of Pharmacology and Experimental Therapeutics*, vol. 343, no. 3, pp. 617–627, 2012.

[58] M. H. Chan, S. Aminzai, T. Hu et al., "A substitution in cGMP-dependent protein kinase 1 associated with aortic disease induces an active conformation in the absence of cGMP," *The Journal of Biological Chemistry*, vol. 295, no. 30, pp. 10394–10405, 2020.

[59] G. Lian, X. Li, L. Zhang et al., "Macrophage metabolic reprogramming aggravates aortic dissection through the HIF1α-ADAM17 pathway☆," *eBioMedicine*, vol. 49, pp. 291–304, 2019.

[60] C. Yunna, H. Mengru, W. Lei, and C. Weidong, "Macrophage M1/M2 polarization," *European Journal of Pharmacology*, vol. 877, article 173090, 2020.

[61] X. Wang, H. Zhang, L. Cao, Y. He, A. Ma, and W. Guo, "The role of macrophages in aortic dissection," *Frontiers in Physiology*, vol. 11, p. 54, 2020.

[62] T. Naito, T. Masaki, D. J. Nikolic-Paterson, C. Tanji, N. Yorioka, and N. Kohno, "Angiotensin II induces thrombospondin-1 production in human mesangial cells via p38 MAPK and JNK: a mechanism for activation of latent TGF-beta1," *American Journal of Physiology. Renal Physiology*, vol. 286, no. 2, pp. F278–F287, 2004.

[63] D. Wen, R. Chen, H. Li et al., "Reduced M2 macrophages and adventitia collagen dampen the structural integrity of blood blister–like aneurysms and induce preoperative rerupture," *Cell Proliferation*, vol. 55, no. 2, article e13175, 2022.

[64] M. Guo, R. Yan, Q. Ji et al., "IFN regulatory factor-1 induced macrophage pyroptosis by modulating m6A modification of circ_0029589 in patients with acute coronary syndrome," *International Immunopharmacology*, vol. 86, article 106800, 2020.

[65] Y. Liu, Z. Liu, H. Tang et al., "The N^6-methyladenosine (m^6A)-forming enzyme METTL3 facilitates M1 macrophage

polarization through the methylation of *STAT1* mRNA," *American Journal of Physiology. Cell Physiology*, vol. 317, no. 4, pp. C762–C775, 2019.

[66] L. M. Fan, G. Douglas, J. K. Bendall et al., "Endothelial cell-specific reactive oxygen species production increases susceptibility to aortic dissection," *Circulation*, vol. 129, no. 25, pp. 2661–2672, 2014.

[67] H. Xu, C. Gan, Z. Gao et al., "Caffeine targets SIRT3 to enhance SOD2 activity in mitochondria," *Frontiers in Cell and Development Biology*, vol. 8, p. 822, 2020.

Hindawi
Oxidative Medicine and Cellular Longevity
Volume 2023, Article ID 8134027, 20 pages
https://doi.org/10.1155/2023/8134027

Research Article

m6A Modification Mediates Endothelial Cell Responses to Oxidative Stress in Vascular Aging Induced by Low Fluid Shear Stress

Zhijue Xu,[1,2] Peng Qiu,[1,2] Yihong Jiang,[1] Jiateng Hu,[1] Zhaoyu Wu,[1] Jiahao Lei,[1] Hongji Pu,[1] Qun Huang,[1] Xin Wang,[1] Bo Li,[1] Kaichuang Ye,[1,2] Xinwu Lu,[1,2,3] and Guang Liu[1,3]

[1]*Department of Vascular Surgery, Shanghai Ninth People's Hospital, Shanghai Jiao Tong University School of Medicine, Shanghai 200011, China*
[2]*Vascular Center of Shanghai Jiao Tong University, Shanghai 200011, China*
[3]*Department of Vascular Surgery, Fengcheng Hospital of Fengxian District, Shanghai 200011, China*

Correspondence should be addressed to Kaichuang Ye; ykaichuang@163.com, Xinwu Lu; luxinwu@shsmu.edu.cn, and Guang Liu; liug112050@sh9hospital.org.cn

Received 27 September 2022; Revised 5 November 2022; Accepted 24 November 2022; Published 27 January 2023

Academic Editor: Yanshuo Han

N6-methyladenosine (m6A) is one of the most prevalent, abundant, and internal transcriptional modification and plays essential roles in diverse cellular and physiological processes. Low fluid shear stress (FSS) is a key pathological factor for many cardiovascular diseases, which directly forces on the endothelial cells of vessel walls. So far, the alterations and functions of m6A modifications in vascular endothelial cells at the low FSS are still unknown. Herein, we performed the transcriptome-wide m6A modification profiling of HUVECs at different FSS. We found that the m6A modifications were altered earlier and more sensitive than mRNA expressions in response to FSS. The low FSS increased the m6A modifications at CDS region but decreased the m6A modifications at 3′ UTR region and regulated both the mRNA expressions and m6A modifications of the m6A regulators, such as the RBM15 and EIF3A. Functional annotations enriched by the hypermethylated and hypomethylated genes at low FSS revealed that the m6A modifications were clustered in the aging-related signaling pathways of mTOR, PI3K-AKT, insulin, and ERRB and in the oxidative stress-related transcriptional factors, such as HIF1A, NFAT5, and NFE2L2. Our study provided a pilot view of m6A modifications in vascular endothelial cells at low FSS and revealed that the m6A modifications driven by low FSS mediated the cellular responses to oxidative stress and cell aging, which suggested that the m6A modifications could be the potential targets for inhibiting vascular aging at pathological low FSS.

1. Introduction

N6-methyladenosine (m6A) is one of the most prevalent, abundant, and internal transcriptional modification. More than 25% of human mRNAs are modified with m6A [1]. It is the methylation at the N6 position of adenosine in RNAs and has been discovered with diverse functions in cellular and physiological processes, and in many diseases such as cancer and obesity [2, 3]. The m6A is controlled by the m6A regulators including m6A methyltransferases (also called as the "writers"), demethylases (also called as the "erasers"), and m6A-binding proteins (also called as the "readers") [4]. These regulators ensure m6A modifications as a dynamic and reversible process. In mRNAs, m6A was found enriched around 5′ untranslated terminal region (UTR), stop codon, and 3′ UTR [5]. Thus, m6A can regulate mRNA splicing, processing, translation, and stabilities [6, 7]. Recent studies revealed that m6A also plays essential roles in hypertension and cardiovascular diseases [8].

Shear force is particularly essential in the cardiovascular system [9]. It is the frictional force from blood flow and parallel to the vessel wall, therefore also called the fluid shear stress (FSS) [10]. Quantitatively, the FSS is defined as the force per unit area with the dyne/cm^2 as unit [11]. Vascular

endothelial cells are the direct objective cells of FSS in vessel walls [12]. Physiologically, persistent FSS maintains the viability of vascular cells and the integrity of vessel walls by inducing the release of vascular factors from endothelial cells [13, 14]. However, in many pathological conditions such as in the atherosclerosis, the major cause for coronary and peripheral artery diseases, FSS is decreased significantly [15]. Low FSS was reported to induce the inflammations, cell apoptosis, and oxidation stress, which could further remodel and aggravate the pathological changes of vessel walls [16, 17]. Thus, low FSS was considered as one of the key pathological factors for many cardiovascular diseases [18].

Aging is one of the major risk factors for the occurrence of cardiac-cerebral vascular diseases (CCVD) [19]. About 1/3 of all deaths at the age of 65 were caused by CCVD in the United States, while the data increased to 2/3 at the age of 85 [20]. Vascular aging is initialed with the endothelial dysfunction and the morphological changes of vessel walls [21]. Endothelial dysfunction is caused by many pathophysiological processes in endothelial cells, such as oxidative stress, epigenetic alterations, chronic inflammation, genomic instability stress, and disorder of proteomic homeostasis [22]. For example, the role of oxidative stress such as increasing of superoxide anion (O^{2-}) in vascular disease is widely accepted [23]. Activation of Nrf2 (nuclear factor erythroid 2-related factor 2), a well-known inhibitor of oxidative stress, could inhibit the reactive oxygen species (ROS) generation and reduce the diabetes-induced vascular aging [24]. Low FSS is also associated with vascular aging and oxidative stress in endothelial cells. Recent studies reported that the FSS-driven sialic acid glycosylation regulated the Nrf2-mediated signaling and modulated oxidative stress in human endothelial cells [25].

So far, however, less studies have reported the relationship between m6A modifications and low FSS, and whether the alterations of m6A modifications driven by low FSS play roles in vascular aging is also unclear. Herein, to determine how low FSS regulates m6A modifications in vascular endothelial cells, we performed the transcriptome-wide m6A modification profiling of HUVECs at different FSS including high FSS, low FSS, and the stationary culture with no FSS. Comparative analysis and bioinformatics analysis were executed for the overall view of the functions of m6A at low FSS and discovering the relationship of m6A modifications with the cell aging and cellular response to oxidative stress at low FSS.

2. Materials and Methods

2.1. Cell Culture. The Human Umbilical Vein Endothelial Cells (HUVECs) were purchased from the Shanghai Cell Bank of the Chinese Academy of Sciences. HUVECs were cultured in High Glucose Dulbecco's Modified Eagle Medium, supplemented with 10% fetal bovine serum, 100 μg/ml streptomycin, and 100 U/ml penicillin and incubated in a 5% CO_2 atmosphere at 37°C.

2.2. Shear Stress. The fluid flow shear stress was performed on the Flexcell Flow System (Burlington, Ontario, Canada). In brief, the HUVECs were seeded on the CS-C culture Slips—collagen type I (Flexcell, Burlington, Ontario, Canada) for 12 h at 37°C. The fluid flow shear stress was applied using a Flexcell FX-4000 strain unit (Flexcell, Burlington, Ontario, Canada) with loading of 0, 5, and 15 dyne/cm^2 for 12 h.

2.3. Phalloidin Staining. The HUVECs were treated with shear stress with loading of 0, 5, and 15 dyne/cm^2 for 12 h, followed by fixing with 4% paraformaldehyde for 30 min. The fixed cells were permeabilized by methanol for 30 min, and then washed with PBS for 3 times. The cells were stained with 0.5 μg/ml of iFluor™ 488-labeled phalloidin for 1 h, followed by washing with PBS for 3 times. The cells were further stained with 5 μg/ml of DAPI for 30 min, followed by washing with PBS for 3 times. After that, the cells were imaged by Nikon A1Si laser-scanning confocal microscope (Tokyo, Japan).

2.4. RNA-Sequencing and m6A-Sequencing. The shear-stressed HUVECs were lysed via TRIzol regent (Thermo Fisher, USA) as soon as the shear stress finished. The total RNA was extracted by the RNeasy Mini Kit (QIAGEN, Germany) in accordance with the manufacturer's procedure. Chemically fragmented RNA (~100 nucleotides) was incubated with m6A antibody for immunoprecipitation according to the standard protocol of the magna-methylated RNA immune-precipitation (MeRIP) m6A kit (Merck Millipore). Library preparation and high-throughput sequencing were performed by SHBIO (Shanghai, China). The transcriptome and purified RNA fragments from m6A-MeRIP were sequenced with Illumina HiSeq4000.

2.5. Data Analysis and Statistics. The quality visualization of all raw reads was accomplished by FastQC (version 0.11.9). Sequencing reads were aligned to the human genome GRCh38/hg38 using HISAT2 with default parameters. For the input libraries, the FPKMs were calculated and the differential gene expression analysis was performed using the R package DESeq2 (version 1.36.0). The $|\log 2FC| > 1$ and P-adjusted < 0.05 were used. For the m6A-modified peaks, the mapped reads were provided for the R package exomePeak (version 3.1) to identify the m6A peaks, followed by visualizing with IGV software. All called peaks were annotated by intersection with gene architecture using R package ChIPseeker (version 1.32.0). The peaks with fold enrichment of pooled to input >1 were considered as m6A-modified peaks. The fold changes of fold enrichments >2 or <0.5, and P-adjusted < 0.05 were used for differentially m6A-modified gene screening. Comparisons between two groups were performed using Student's t tests (two–tailed) or the Mann–Whitney U test.

2.6. Bioinformatics Analysis. The volcano plot was performed using GraphPad Prism 5.0 software (San Diego, CA, USA) with the fold changes and adjust P values. PCA analysis was conducted using the R package factoextra (version 1.0.7) and visualized using scatterplot3d (version 0.3-41). Venn diagram was conducted using the R package ggplot2 (version 3.3.3). The distribution of m6A modifications on genes was

visualized via metageneplot. The motifs were analyzed using HOMER. Heatmaps were drawn using the R package ComplexHeatmap (version 2.12.0). The enrichment analysis of gene ontology (GO) and Kyoto Encyclopedia of Genes and Genomes (KEGG) was implemented by the R package clusterProfiler based on the package of http://org.Hs.eg.db and GOplot. The top five annotations of each database were shown in bar plot. The top 12 annotations with adjusted P values were shown in circle plot. The enrichment analysis of Reactome was conducted using the online database (https://reactome.org/). The top five annotations of hypermethylated genes and hypomethylated genes were shown in bar plot, respectively. Protein–protein interaction networks were constructed using STRING (version 11.5). The cutoff value of confidence interaction score was used >0.99. The networks were visualized with Cytoscape (version 3.8.2) and clustered with the Molecular Complex DEtection (MCODE) plugin. The total of 962 oxidative stress-related genes were obtained from the GeneCards® The Human Gene Database (downloaded on July 11, 2022), and the total of 1,509 human aging-related genes were obtained from the Human Aging Genomic Resources (downloaded on July 11, 2022).

3. Results

3.1. The m6A Modifications Were Regulated by Shear Stress. To determine the relationship between m6A modifications and shear stress, the HUVECs were treated with low FSS (5 dyne/cm^2), high FSS (15 dyne/cm^2), and no FSS (0 dyne/cm^2), followed by MeRIP sequencing analysis (Figure 1(a)). Along with the dose of FSS from 0 to 15 dyne/cm^2, cell alignments displayed more and more parallel (Figure 1(b)), confirming the cells at different FSS. After sequencing, compared to the no FSS, 891 genes were high-expressed at high FSS, and 2108 genes were high-expressed at low FSS (Figure S1). In the comparison of gene expressions at high and low FSS, 795 genes were upregulated at low FSS, while 196 genes were downregulated at low FSS (Figure S1). Moreover, 588 peaks were hypermethylated at low FSS and 732 peaks were hypomethylated at low FSS (Figure 1(c)). While by comparing to no FSS, less peaks were hypermethylated at both high and low FSS (Figure 1(c)).

Both gene expressions and m6A modifications revealed that the three groups of cells treated by no, low, and high FSS were separated significantly (Figures 2(a) and S2). Interestingly, the high FSS-treated cells fall in between no FSS and low FSS-treated cells (Figure 2(a)), suggesting that the differences between low FSS and no FSS were larger than that between high FSS and no FSS. We next used Venn diagram to analyze the overlapping among differently expressed or m6A-modified genes between high and low FSS and low and no FSS (Figure 2(b)). There was only one gene, MEGF6, displaying a significantly increasing expression from 0 to 15 dyne/cm^2 shear stress (left panel of Figure 2(b), and Figure 2(c)). While there were 10 genes with increasing m6A modifications and 61 genes with decreasing m6A modification corresponding to the changes of 0 to 15 dyne/cm^2 shear stress (right panel of Figure 2(b)). The top three of the increasing and decreasing m6A-modified genes were ARHGEF12, CBL, and KMT2E and RBM12, TRIP12, and ADGRG6, respectively (Figure 2(d)). This result indicated that in addition to the gene expressions, the m6A modifications displayed a better dose response to FSS. The gene expression of MEGF6 and those m6A modifications on the identified genes might be considered as biosensors of HUVECs in response to FSS.

3.2. Low FSS Altered the Distribution of m6A Peaks. Venn diagrams revealed that the overlapping m6A-modified peaks between low FSS and high FSS, low FSS and no FSS, and high FSS and no FSS were 4620, 4072, and 4529, respectively (Figure 3(a)). Using these overlapping peaks, we analyzed the distribution of m6A modifications stimulated by low and high FSS. Compared to no FSS, low FSS reduced the m6A modifications in CDS region of mRNAs and increased the m6A modifications in 3′ UTR regions. While high FSS altered a fat lot of m6A distributions to no FSS (Figure 3(b)). Moreover, compared to high FSS, low FSS reduced the m6A modifications in CDS region from 43.3% to 33.4% and increased the m6A modifications in 3′ UTR region from 35.8% to 49.6% (Figures 3(b) and 3(c)), indicating that the low FSS could enhanced the m6A deposition on 3′ UTR region. To validate the m6A sites, we performed de novo motif search of the m6A peaks with HOMER and identified the first motif of all three groups were GGACC (Figure 3(d)), which was consistent with the m6A consensus DRACH motif. Compared to high FSS, low FSS showed the motif with enrichment of uracil (Figure 3(d)), further suggesting that low FSS altered the distribution and sequence preference of m6A modifications.

3.3. Low FSS Modulates the m6A Regulators. To determine the correlation between mRNA expressions and m6A modifications under FSS treatments, we performed the four-quadrant diagrams as shown in Figure 4(a). In comparation between low and high FSS, only 7 genes of high FSS group were high-expressed and differentially modified by m6A with 6 of them hypermethylated and one of them hypomethylated. But in low FSS group, 215 genes were high-expressed and differentially modified by m6A with 42 genes hypermethylated and 173 genes hypomethylated. It indicated that low FSS dramatically altered m6A modification in HUVECs.

To explore the mechanism of low FSS in regulation on m6A, we analyzed the expressions and m6A modifications of the m6A regulators including 8 writers, two erasers, and 25 readers (Figure 4(b)). Among the 35 m6A regulators, 6 of them were differential expressed (Figure 4(c)), and 11 of them were differentially modified by m6A (Figure 4(d)). The 6 differential expressed regulators were all upexpressed in low FSS, in which the writer of RBM15 was hypomethylated and the reader of EIF3A was four-sites of methylation with one hypomethylated and one hypermethylated. These results indicated that low FSS altered the m6A modification and expression of the m6A regulators especially RBM15 and EIF3A, which further regulated the m6A modifications on the other mRNAs.

3.4. Low FSS Modulated the m6A Modifications of the Aging-Related Genes. To determine the biofunctions of the m6A-

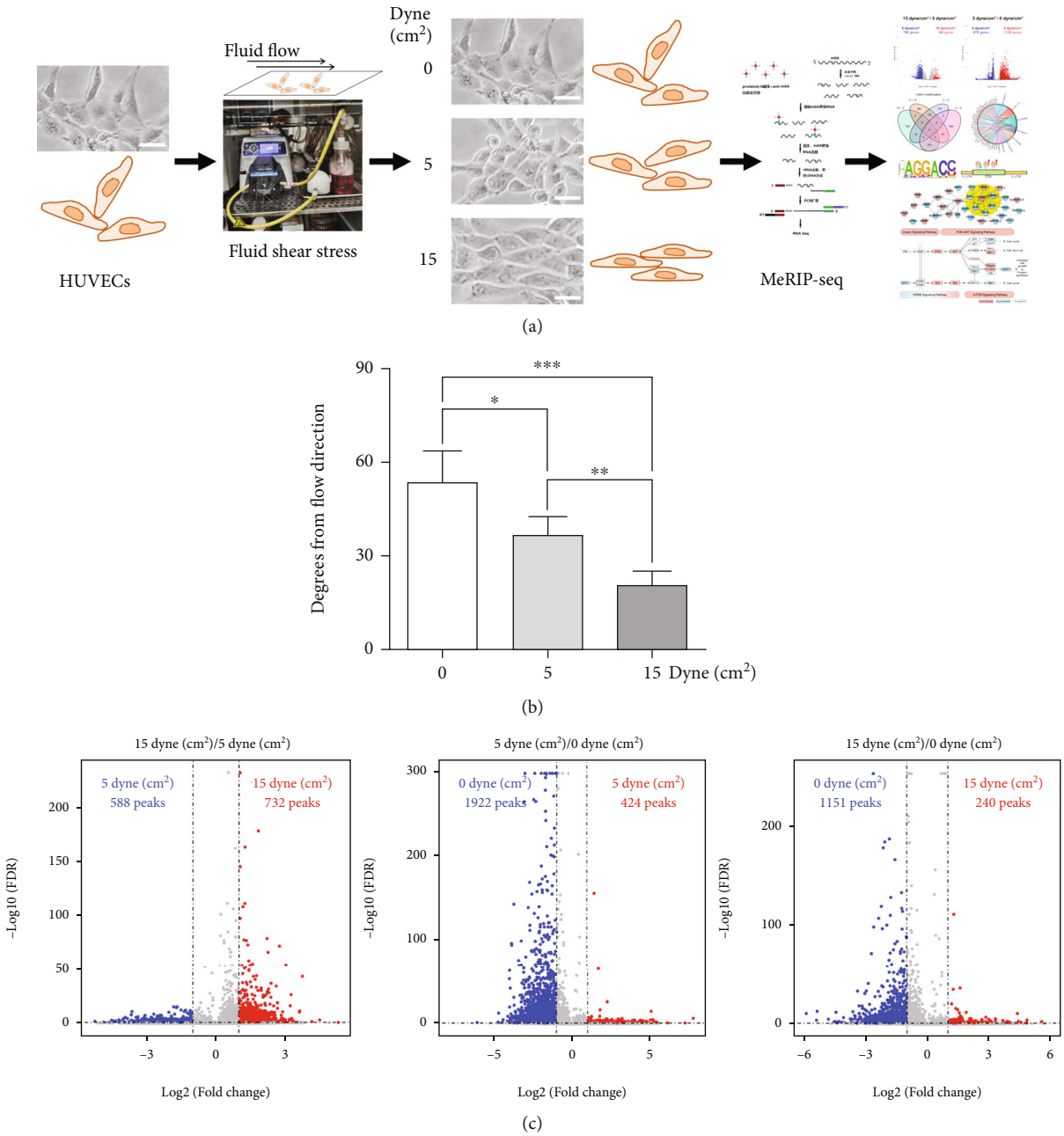

Figure 1: Fluid shear stress dramatically regulates the m6A modifications on mRNA. (a) Schematic of the MeRIP sequencing analysis of HUVECs induced by fluid shear stress. The HUVECs were stimulated by fluid shear stress for 12 h. (b) Quantitation of the angles between long cell axis and flow direction. (c) Volcano plots of the hypermethylated and hypomethylated peaks regulated by different fluid shear stress.

modified genes regulated by low FSS, we comparatively analyzed the enriched annotations of the m6A modified genes and the differentially expressed genes in according to GO and KEGG databases (Figure 5(a)). There were 110 annotations enriched in both two gene sets. Among them, 32 annotations displayed the consistent changes with 31 of them upregulated in both two gene sets, and one of them was downregulated which was the GO annotation of establishment or maintenance of cell polarity. On the other hand, 78 of annotations were upregulated in mRNA expression set but were downregulated in m6A modification set. It indicated that the m6A modifications modulated by low FSS were dramatically upregulated many processes in HUVECs, no matter hypermethylation nor hypomethylation. We next focused on the annotations enriched by m6A-modified gene set. In the integrated analysis of both hypermethylated and hypomethylated gene sets, most of the enriched annotations were with negative z-scores (Figure 5(b)). It suggested that the low FSS might play more functions via hypomethylation rather than hypermethylation. GO analysis revealed that low FSS-hypomethylated genes were enriched in the biological processes of RNA splicing, histone modification, and

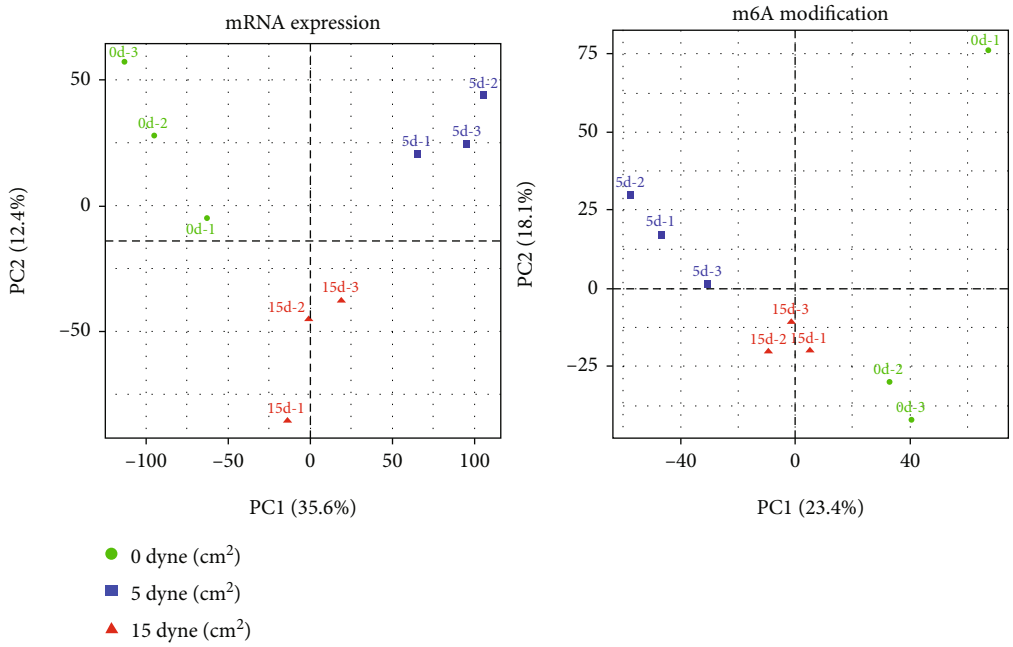

(a)

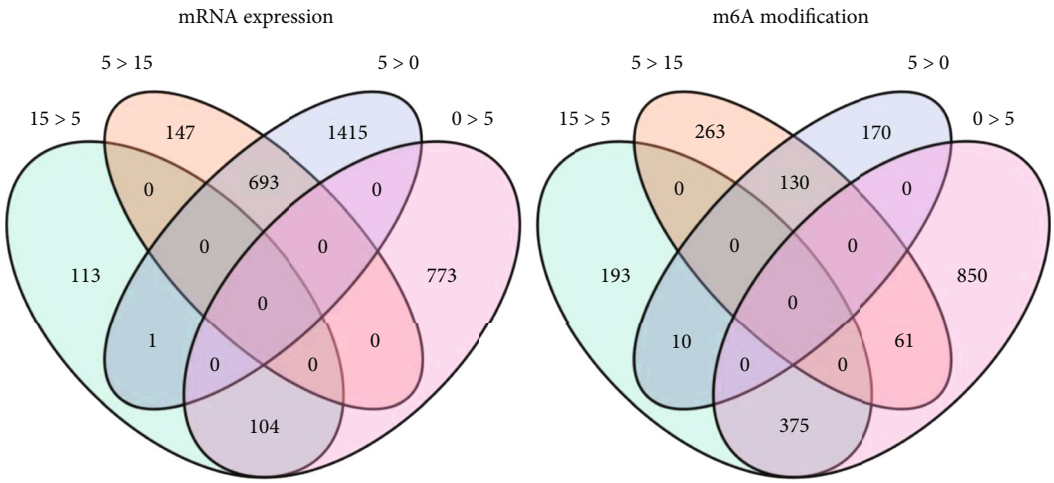

(b)

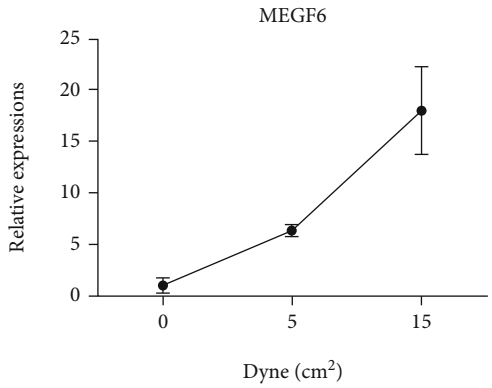

(c)

Figure 2: Continued.

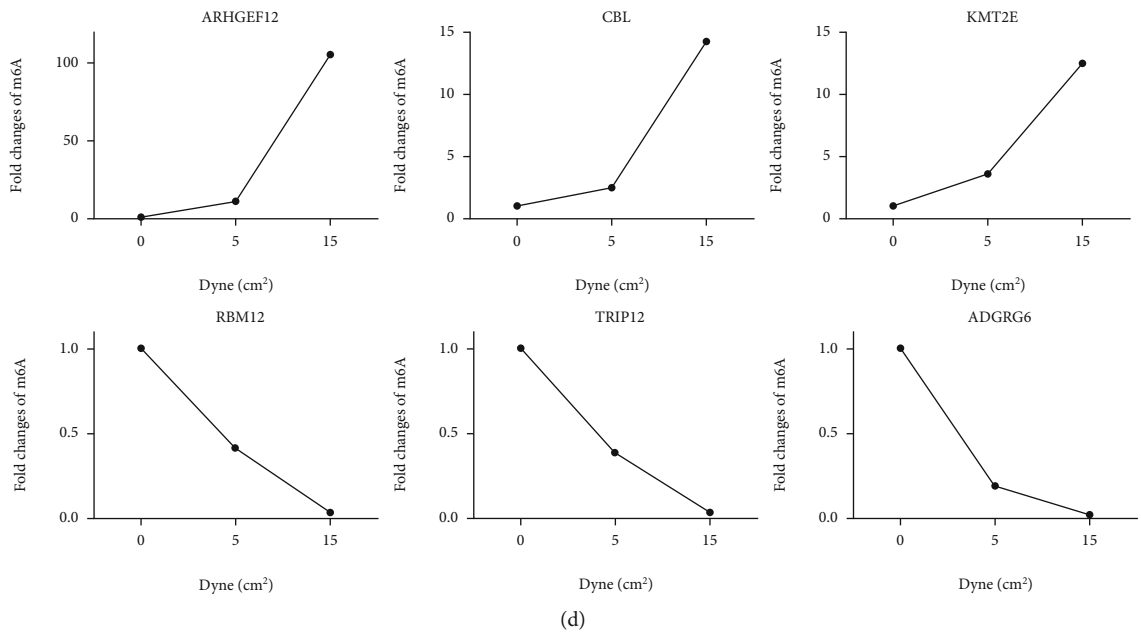

Figure 2: The m6A modifications displayed a better dose response to fluid shear stress. (a) PCA plots of the repeated cells exposed to different fluid shear stress. (b) Venn diagrams between differential expressed genes and hypermethylated/hypomethylated genes, respectively. (c) The gene expression of MEGF6 corresponding to different fluid shear stress. (d) Fold changes of m6A modifications on the mRNA of ARHEF12, CBL, KMT2E, RBM12, TRIP12, and ADGRG6, which were corresponding to different fluid shear stress.

covalent chromatin modification (Figure 5(c)). The proteins translated by those genes were located in nuclear speck, spindle, spliceosomal complex, methyltransferase complex, and pronucleus and played molecular functions of thyroid hormone receptor binding, basal transcription machinery binding, basal RNA polymerase II transcription machinery binding, and transcription coactivator activity (Figure 5(c)). It indicated that low FSS played roles in gene transcriptions and RNA processing, which were all important in cell proliferation and survival. We further performed the interaction network of the m6A-modified genes using the STRING database. The low FSS-driven hypermethylated and hypomethylated genes displayed strong interactions, and the network under the confidence interaction score of 0.99 as cutoff value was shown (Figure 5(d)). The top five of MCODE clusters were lined with the score of 6.86, 5.60, 5.60, 4.50, and 4.0, respectively. The first clusters contained the genes of JUN, HIF1A, SP1, MYC, SMAD3, EP300, KAT2B, and CREBBP, which were transcriptional factors or cofactors and all played roles in aging-related processes such as cell cycles, stress response, and senescence. Taken together, these results all indicated that the low FSS-driven m6A modifications were enriched in the aging-related genes.

3.5. The Differential m6A Modifications Regulated Cell Response to Oxidative Stress. To determine the functional role of the m6A modifications in response to oxidative stress at low FSS, we compared the literature oxidative stress-related genes with our detected m6A-modified genes (Figure 6(a)). Among the 962 oxidative stress-related genes, 210 of them were modified with m6A with 30 hypermethylated genes and 41 hypomethylated genes at low FSS (Figures 6(b) and 6(c)). Functional enrichment analysis indicated that most of the enriched annotations were with negative z-score (Figure 6(d)), suggesting that the functions of hypomethylated genes at low FSS were more assembled than that of the hypermethylated genes. The hypomethylated genes were enriched in G1/S transition, TF complex, TF activity, TF binding, ErbB signaling, and processing in ER, and the hypermethylated genes were enriched in the RNA process, PI3K activity, apoptosis, and drug resistance (Figure 6(e)). These annotations were important for aging-related processes, such as cell cycle, protein synthesis, and cell survival. Moreover, the protein-protein interaction network revealed that the first MCODE cluster with a score of 6.67 contained the transcriptional factors of JUN, SP1, HIF1A, MYC, EP300, SMAD2, and SMAD3 (Figure 6(f)), which were also important for cell cycle and survival. In the Reactome database analysis, the hypomethylated genes were enriched in intrinsic pathway for apoptosis, apoptosis, and transcriptional regulation by TP53, SMAC (DIABLO) binds to IAPs, and FOXO-mediated transcription, and the hypermethylated genes were enriched in the signaling by NOTCH, Pre-NOTCH transcription and translation, cellular responses to stimuli, estrogen-dependent gene expression, and cellular responses to stress (Figure 6(g)). Taken together, these results confirmed that the m6A modifications on the oxidative stress-related genes driven by low FSS could play essential roles in aging process.

3.6. The m6A Modifications Regulated Aging Process at Low FSS. To determine how the m6A modifications regulates the aging process at low FSS, we performed the functional enrichment analysis of the overlapping genes of aging-related genes with our detected m6A-modified genes. There were 1,509

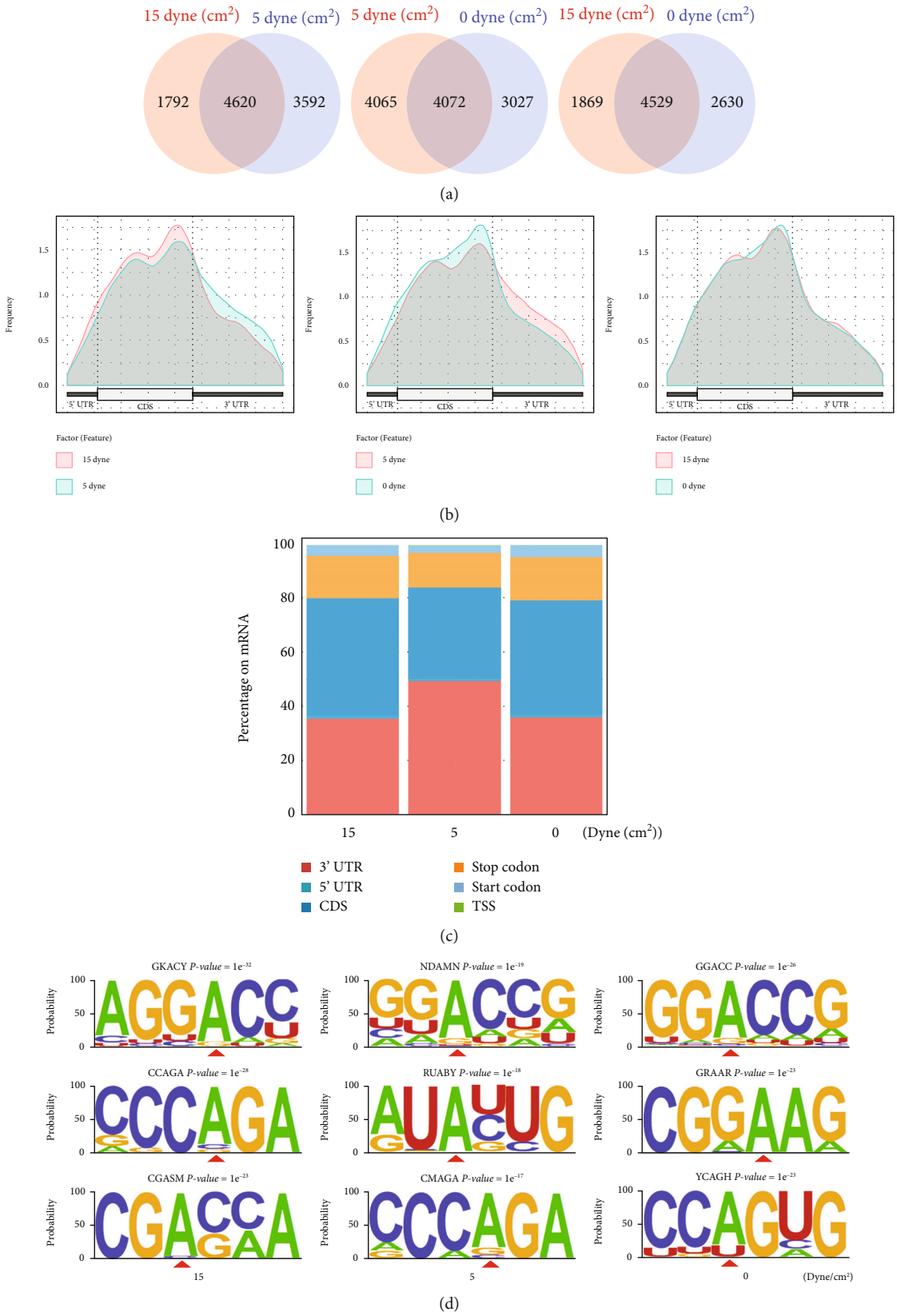

Figure 3: Low FSS altered the distribution of m6A peaks. (a) Venn diagrams of m6A modified peaks between no, low, and high FSS-treated cells. (b) Metageneplot of the m6A-modified peaks on mRNA. (c) Distribution of the m6A peaks to the respective input read coverage for mRNA. (d) Motifs at nucleotide positions around the m6A peaks. The top three motifs were displayed. The modified positions of adenine were labeled with red triangles.

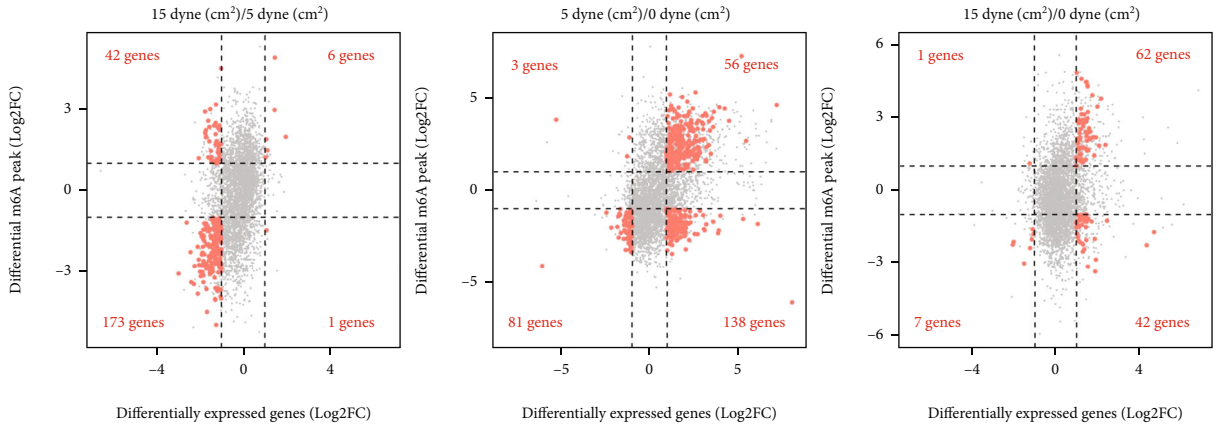

(a)

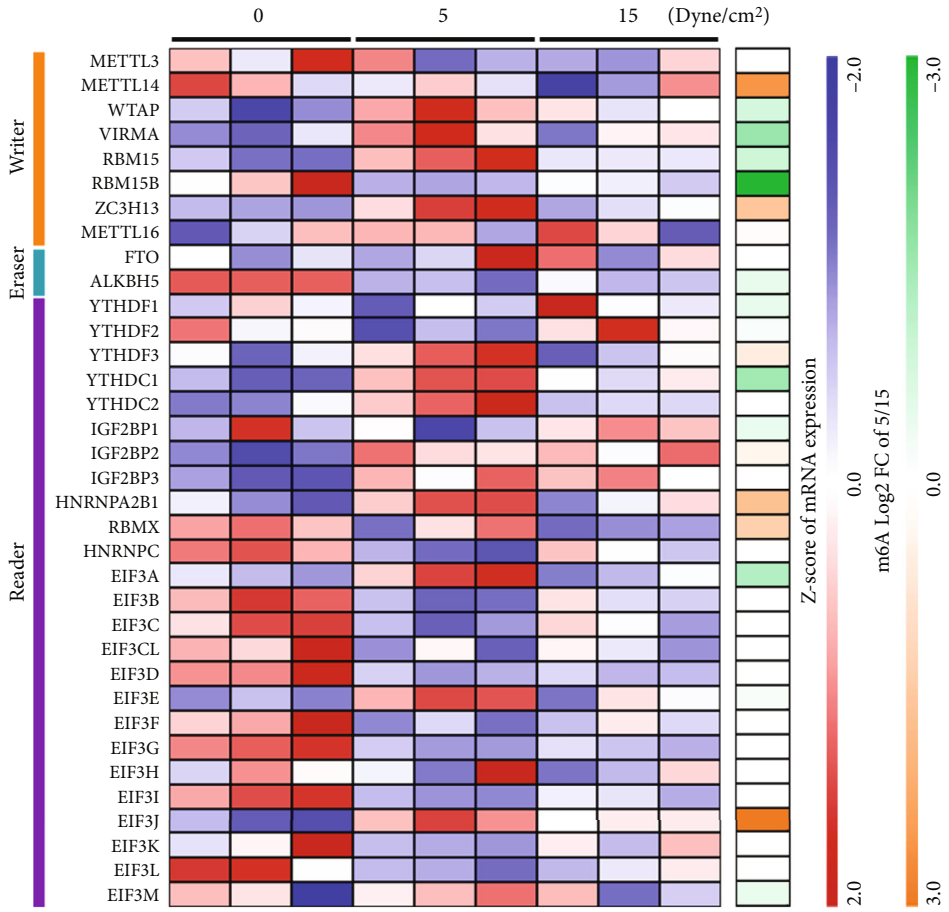

(b)

Figure 4: Continued.

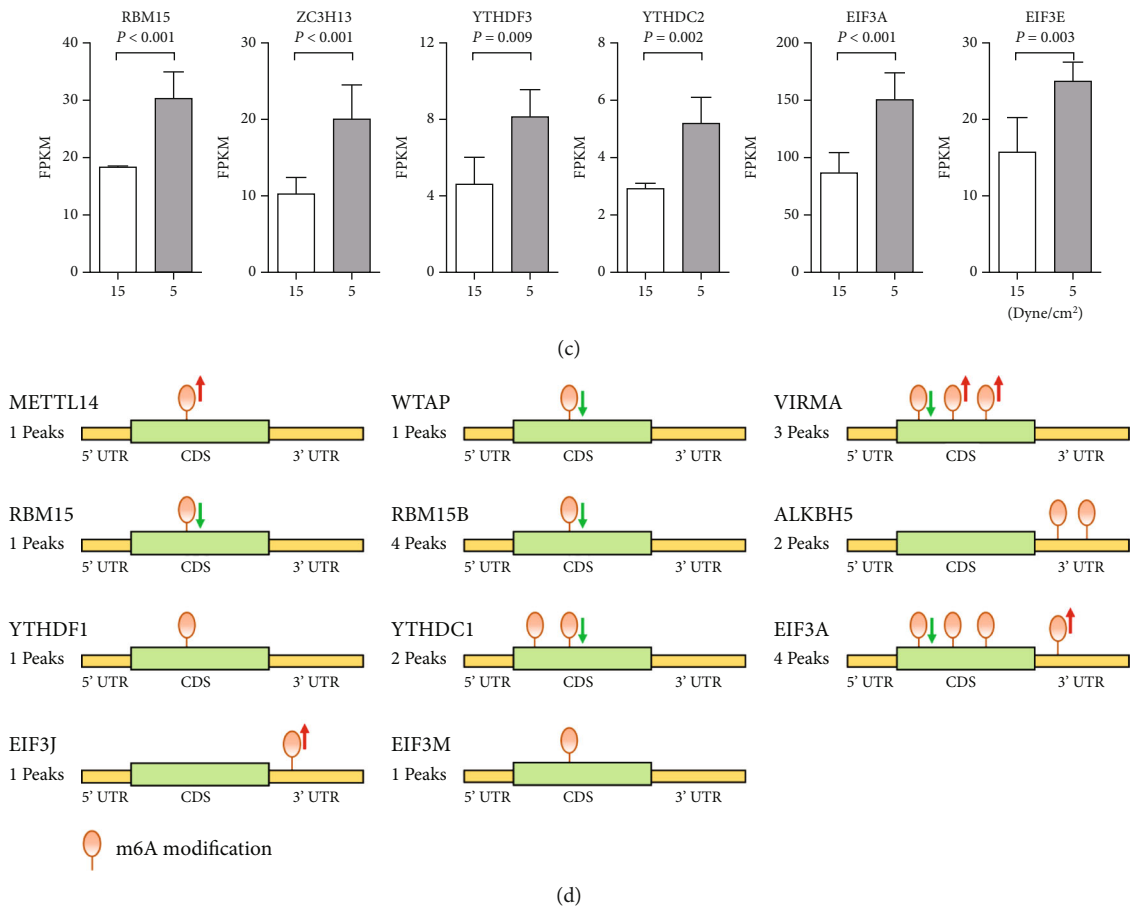

Figure 4: Low FSS modulates the m6A regulators. (a) Four-quadrant diagram of the differentially expressed genes and differentially m6A-modified genes. (b) Heatmap of the m6A regulators in mRNA expressions and m6A modifications. (c) RNA expressions of six differentially expressed m6A regulators. |FoldChange| > 1.5, *P*-adjusted < 0.05. (d) Distributions and counts of m6A modifications on differentially modified m6A regulators. *P*-adjusted < 0.05. The hypermethylated and hypomethylated peaks were labeled with red and green arrows, respectively.

aging-related genes in the Human Aging Genomic Resources. Among them, 384 of them were modified with m6A (Figure 7(a)), with 47 hypermethylated genes and 65 hypomethylated genes at low FSS (Figure 7(b) and Figure S3). GO analysis indicated that the hypomethylated genes were enriched in the cellular response to oxygen, TF complex, and choline metabolism (Figures 7(c) and 7(d)), which were assistant with the annotations in the response to oxidative stress (Figure 6(e)). And the hypermethylated genes were enriched in mTOR signaling, β-catenin complex, and TOR complex (Figures 7(c) and 7(d)). KEGG pathway analysis further indicated that the m6A at low FSS was upregulated in mTOR signaling pathway, insulin signaling pathway, and PI3K-AKT signaling pathway and were abnormal in ERRB signaling pathway (Figure 7(e)). In detail, the PI3K, AKT, Mcl-1, Sos, Raf, Raptor, and mTORC1 were hypermethylated, and the NRG1, TSC1, Myc, 4EBP1, and CDK were hypomethylated. These pathways played essential roles in cell cycle, cell survival, inhibition of cell growth, and protein synthesis, which were the core pathways of cell aging. Thus, the low FSS might regulate the aging process via altering the m6A of mTOR, PI3K-AKT, insulin, and ERRB signaling pathways.

We further comprehensively analyzed the oxidative stress-related genes, aging-related genes, and the low FSS-driven m6A differentially modified genes. There were 20 of m6A differentially modified genes which were related with both the response to oxidative stress and the aging (Figure 7(f)), including many important transcriptional factors such as HIF1A, SP1, JUN, MYC, and NFAT5 (Figure 7(g)). Nine of the 20 genes were differentially expressed at mRNA level with *P* value < 0.05 (Figure 7(h)), with seven upexpressed genes and two downexpressed genes. Eight of them were hypomethylated and one was hypermethylated. The transcriptional factors of NFAT5, HIF1A, and NFE2L2 were all hypomethylated and upexpressed (Figure 7(h)). Taken together, these results indicated that the low FSS might regulate the aging process via hypomethylating the key transcriptional factors and signaling pathway in the response to oxidative stress.

4. Discussion

Low FSS and m6A modifications were both widely studied in the aging process, but the internal relationship between the two is unknown so far. In this study, we performed the

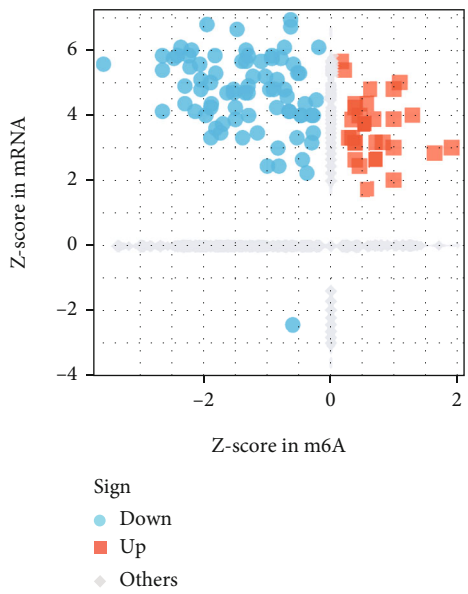

(a)

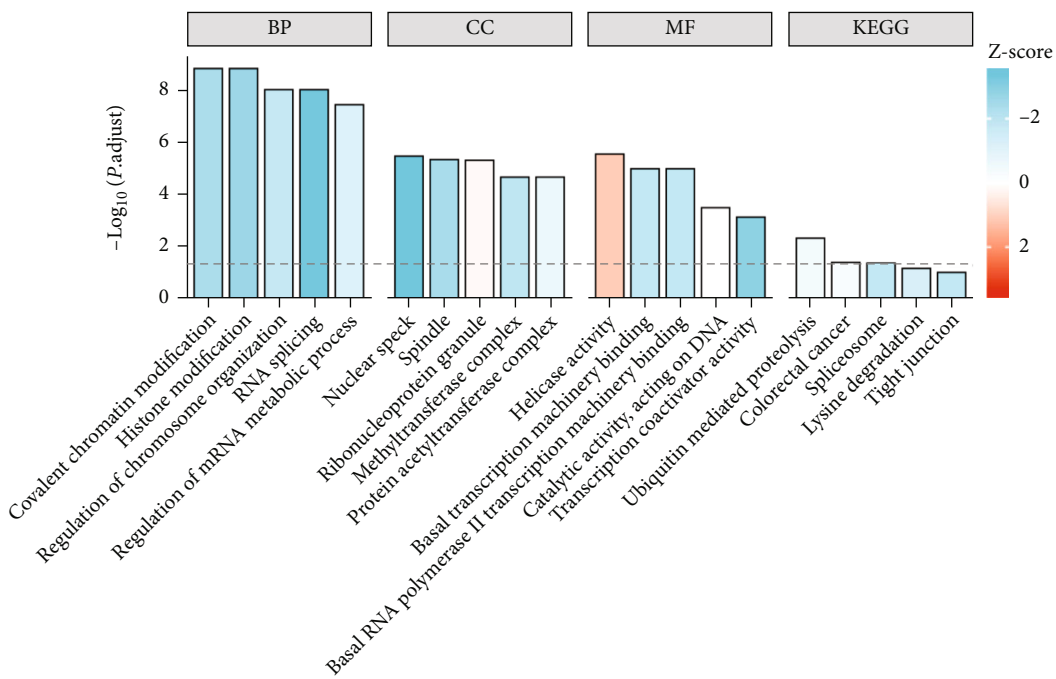

(b)

Figure 5: Continued.

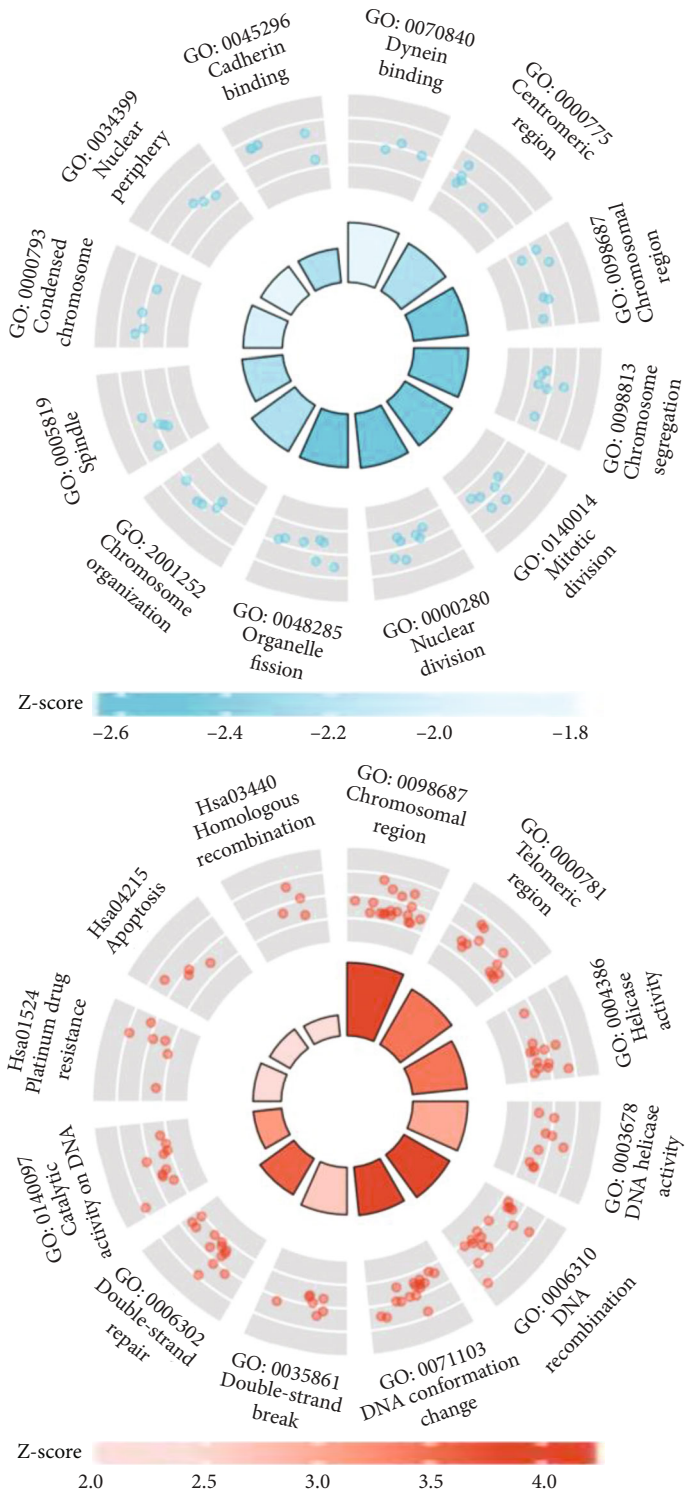

(c)

Figure 5: Continued.

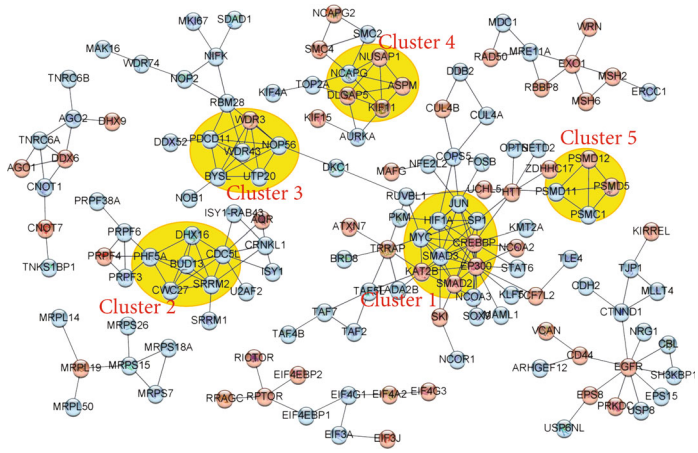

(d)

Figure 5: Low FSS modulated the m6A modifications on aging-related genes. (a) Scatter plot of the annotation enrichment analysis (GO and KEGG databases) based on fold changes in the m6A modification (x-axis) and transcriptome (y-axis). The annotations upregulated in m6A-modified genes were colored in red, and annotations downregulated in m6A-modified genes were colored in blue. (b) Bar plot of the annotation enrichment analysis (GO and KEGG databases) of m6A-modified genes. (c) Circle plot of GO analysis of m6A-modified genes. The hypermethylated and hypomethylated genes were analyzed separately. (d) Interaction network of m6A-modified genes, analyzed by STRING and visualized with Cytoscape software. The hypermethylated and hypomethylated genes were colored in red and blue, respectively. The top five functional clusters were defined *via* the MCODE plugin.

transcriptome-wide m6A modification profiling of HUVECs at different FSS and compared the alteration of m6A at the physiological high FSS and the pathological low FSS. Functional annotations were enriched more in the gene set with hypomethylation at low FSS, which were clustered in the processes of cell cycle, apoptosis, and cellular senescence, and in the genes of transcriptional factors and RNA processing. Our results revealed that the m6A modifications driven by low FSS could mediate the cellular responses to oxidative stress and cell aging.

Changes in m6A modifications have been found with close interactions and relationships with oxidative stress in many physiological and pathological processes [26]. In human keratinocyte cells, high level of m6A modification in human HaCaT cells promoted cell survivals through inhibiting oxidative stress [27]. In the development of Parkinson's disease, inhibition of m6A modification was found to elevate oxidative stress and Ca^{2+} influx that resulted in the cell death of dopaminergic neuron [28]. We found that low FSS-modulated oxidative stress-related processes including hypermethylated RNA process, cell apoptosis, and drug resistant genes and hypomethylated cell cycle, protein process, and transcriptional factor genes. Noteworthy, a group of oxidative stress-related transcriptional factors were highly enriched, including HIF1A, MYC, and SP1. The HIF1A (hypoxia inducible factor 1α) is a critical factor in oxidative stress, which is induced by hypoxia and many other oxidative stress inducers, and regulated cellular responses to modulate oxidative stress [29]. A recent study reported that hypermethylation of HIF1A mRNA facilitated the mRNA translation and increased HIF1A protein abundance [30]. In our results, low FSS hypomethylated the HIF1A mRNA. It indicated that the protein abundance of HIF1A in endothelial cells might be inhibited at low FSS, suggesting that low FSS could induce oxidative stress. The MYC is also essential for the cellular response to oxidative stress [31]. Increasing global m6A RNA modification in leukemia cells could decrease the stability of MYC and result in the suppression of MYC pathways [32]. At low FSS, the global of m6A was preferred to hypomethylation, which might active the MYC pathways in response to oxidative stress, also suggesting that low FSS induced oxidative stress. Furthermore, the SP1 was found inducible by oxidative stress for negative feedback of antideath role [33]. And inhibition of m6A on SP1 was found to decrease SP1 expression and inhibit cell proliferation [34]. Our results indicated that low FSS also hypomethylated SP1, suggesting that low FSS inhibit the antioxidative stress functions of SP1. Taken together, the hypomethylations of all the three transcriptional factors of HIF1A, MYC, and SP1 revealed a consistent cellular fate that low FSS promoted oxidative stress in vascular endothelial cells. Therefore, increasing the m6A modifications might be a potential target for modulating the low FSS-driven oxidative stress in vessels.

On the other hand, oxidative stress can also mediate the change of m6A modification via regulating the expression of m6A regulators. In cobalt-induced oxidative stress, the expressions of the m6A demethylase FTO were inhibited, which further regulated caspase activation, G1/S cell cycle arrest, and cell apoptosis in an m6A-dependent manner [35]. In placenta trophoblast, another m6A demethylase of ALKBH5 was found upexpressed in preeclamptic placental tissues and mediated the m6A modification of peroxisome proliferator-activated receptor PPARG, which alleviates hypoxia-induced oxidative stress and apoptosis [36]. In our case of low FSS, the expressions of FTO and ALKBH5 were found with no significant changes, while the methyltransferase of RBM15 and the m6A binding proteins of EIF3A were

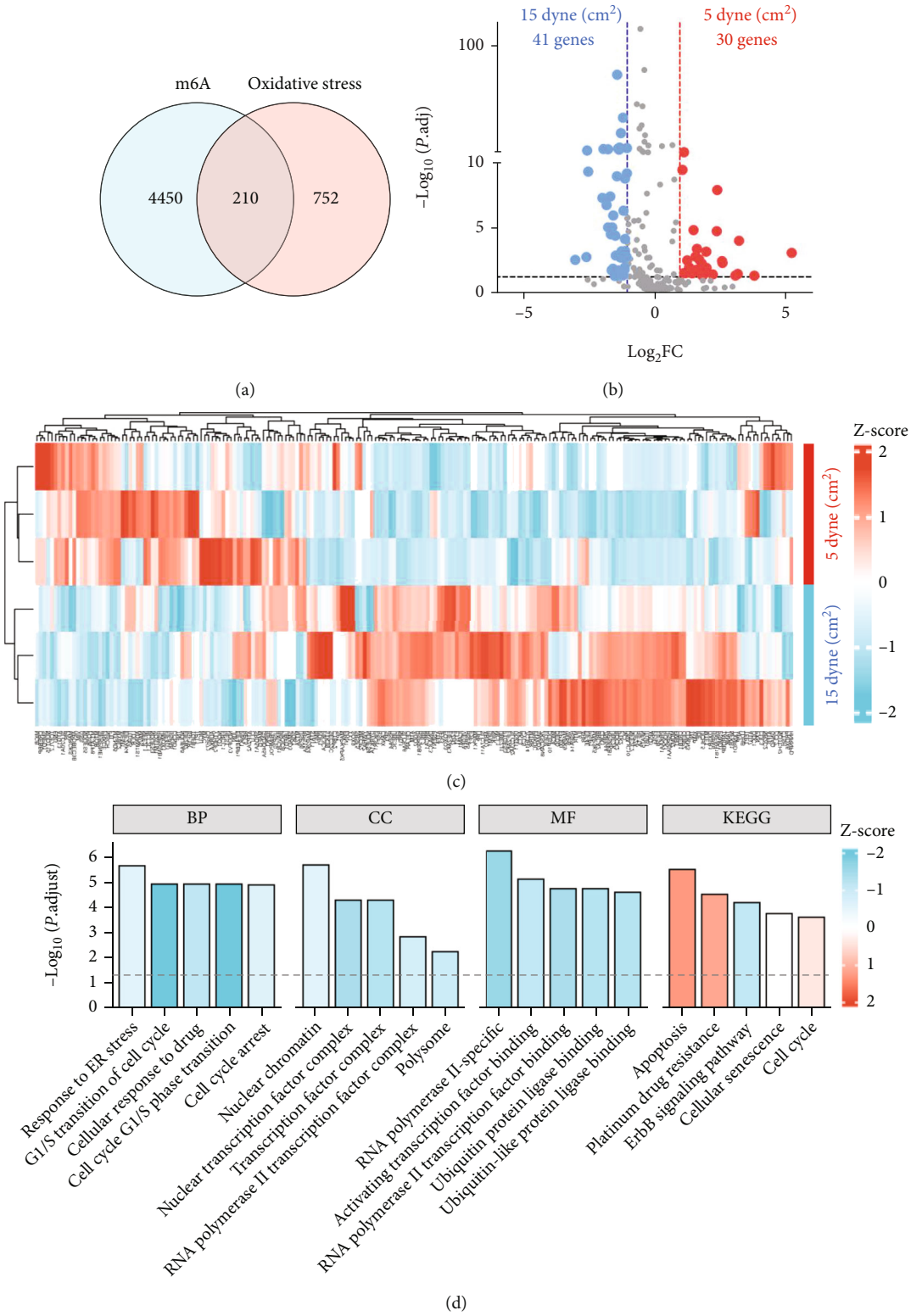

Figure 6: Continued.

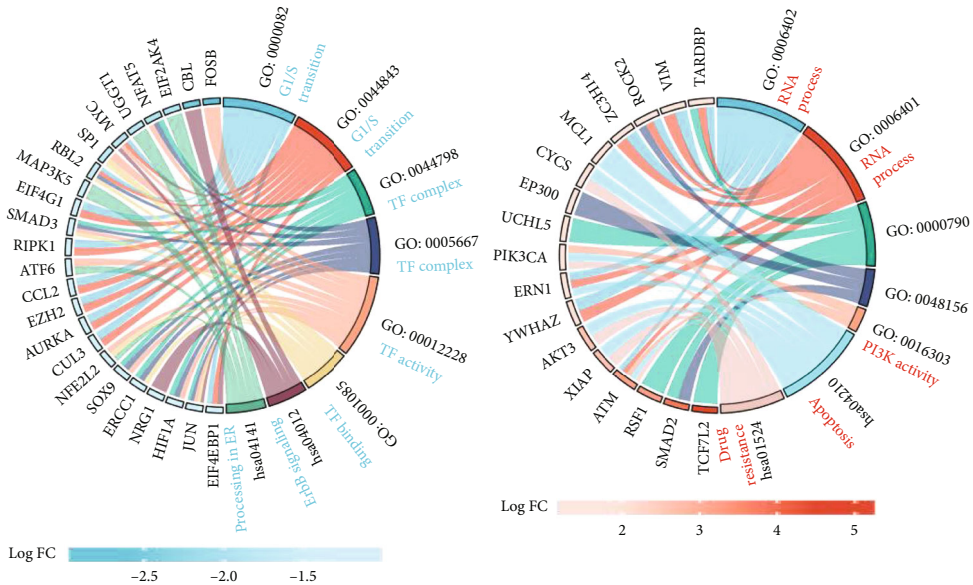

(e)

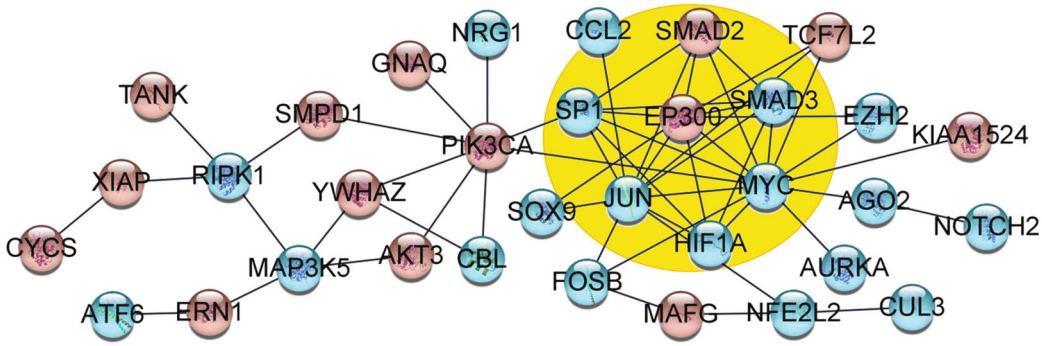

(f)

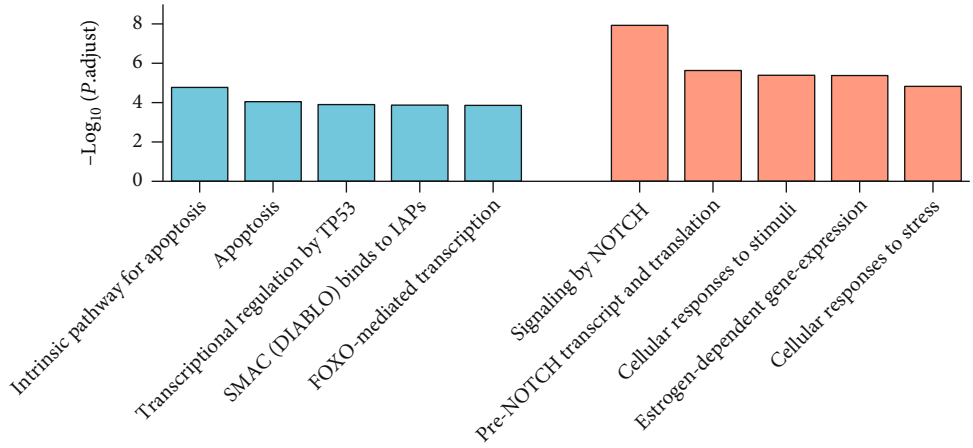

(g)

Figure 6: Essential roles of the m6A modifications at low FSS in response to oxidative stress. (a) Venn diagram of m6A-modified genes and oxidative stress-related genes. (b) Volcano plots of the m6A-modified oxidative stress-related genes. (c) Heatmap of the m6A-modified oxidative stress-related genes. (d) Bar plot of GO and KEGG database analyses. (e) Circle plot of GO and KEGG database analyses. The hypermethylated and hypomethylated genes were analyzed separately. The annotations of hypermethylated genes were colored in red, and annotations of hypomethylated genes were colored in blue. (f) Interaction network of differentially m6A-modified oxidative stress-related genes. The hypermethylated and hypomethylated genes were colored in red and blue, respectively. The first functional clusters were circled out in yellow. (g) Bar plot of Reactome database analysis. The annotations of hypermethylated genes were colored in red, and annotations of hypomethylated genes were colored in blue.

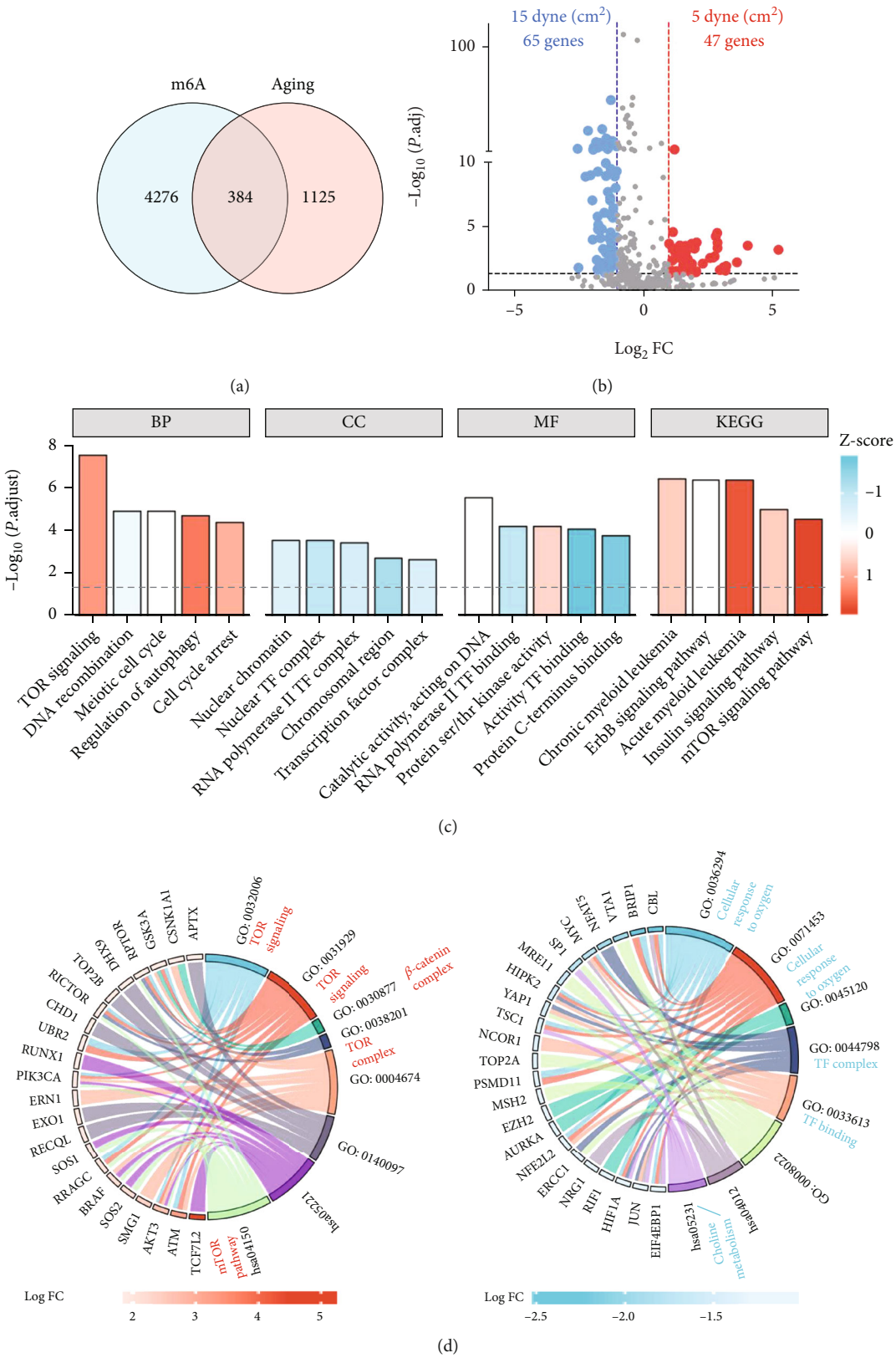

(d)

Figure 7: Continued.

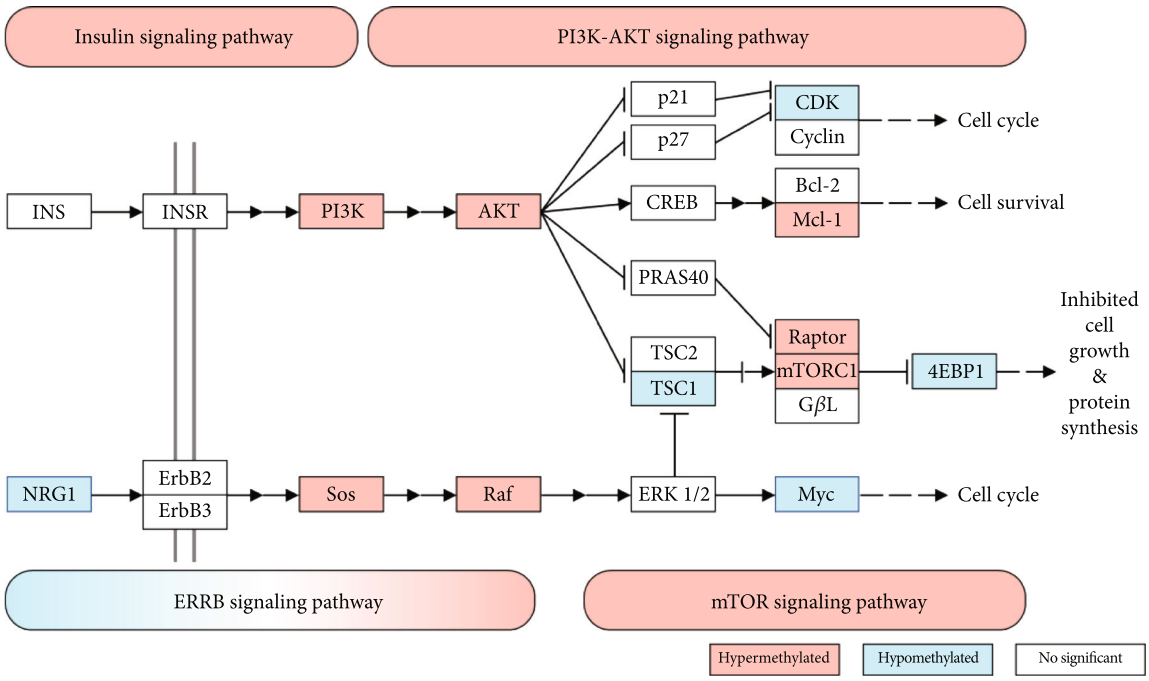

(e)

(f)

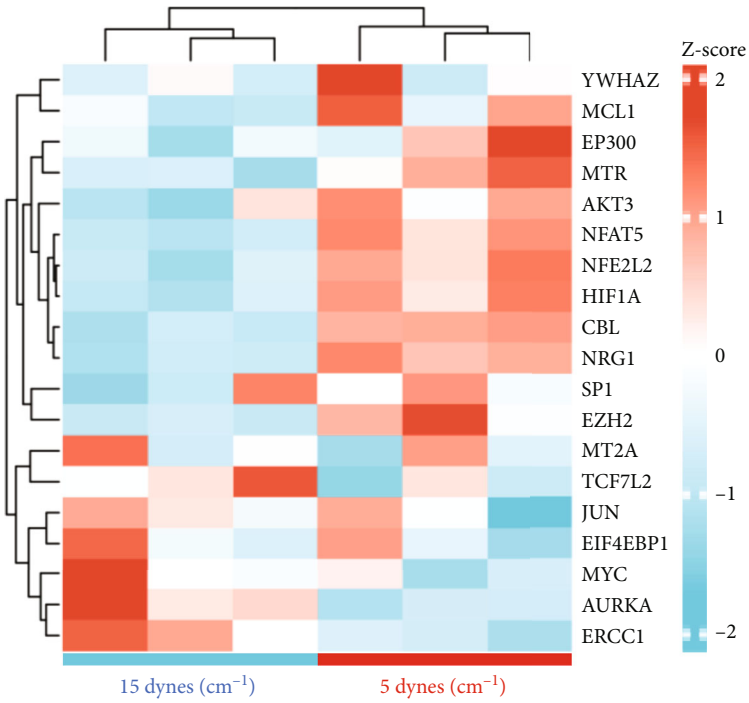

(g)

Figure 7: Continued.

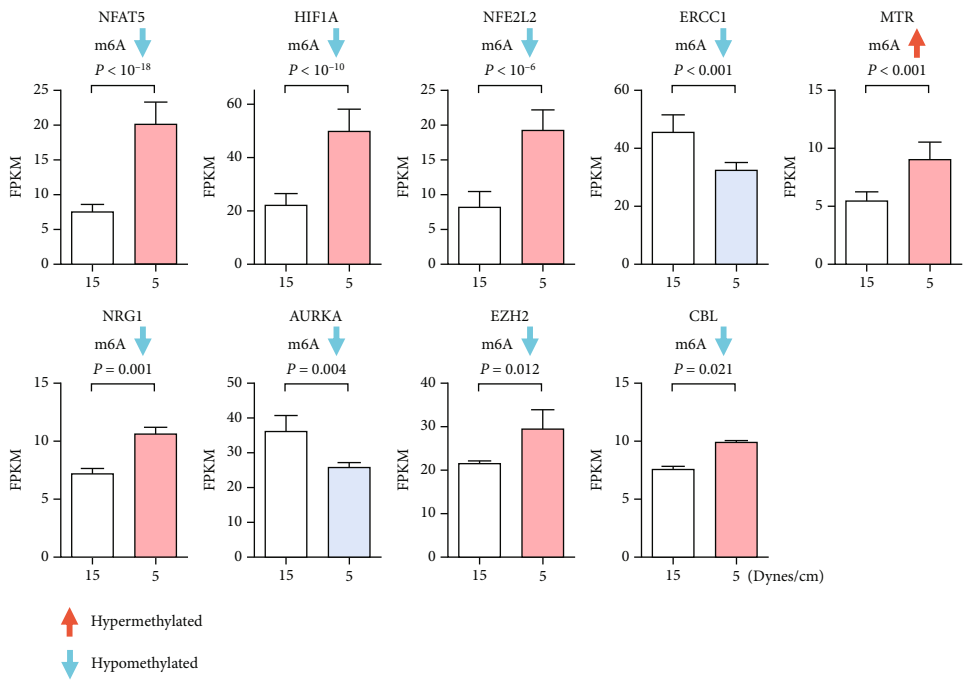

(h)

Figure 7: The low FSS-driven m6A modifications regulated aging process. (a) Venn diagram of m6A-modified genes and aging-related genes. (b) Volcano plots of the m6A-modified aging-related genes. (c) Bar plot of GO and KEGG database analyses. (d) Circle plot of GO and KEGG database analyses. The hypermethylated and hypomethylated genes were analyzed separately. (e) KEGG pathway enriched by m6A-modified aging-related genes. The full maps of the four KEGG pathways were shown in Figure S4 and S5. (f) Venn diagram of m6A differentially modified genes, oxidative stress-related genes, and aging-related genes. (g) Heatmap of the m6A differentially modified genes which was both oxidative stress and aging-related genes. (h) RNA expressions of the genes in Figure 7(g) with adjust P value < 0.05.

upexpressed and m6A differentially modified. Both RBM15 and EIF3A were crucial in cell cycle and cell survival [37, 38]. RBM15-mediated m6A was found playing roles in the insulin signaling pathway [39], which was also enriched in our results at low FSS. EIF3A was found to directly bind with 5′ UTR of ATF4, a critical antagonizing factor of oxidative stress in cardiovascular disease [40], and regulated the protein expression of ATF4 in a m6A dependent-manner [41]. Thus, low FSS might use RBM15 and EIF3A as handles to modulate m6A modifications in vascular endothelial cells and to mediate oxidative stress.

Low FSS is a profound pathological inducer for endothelial dysfunction and vascular aging [42]. We identified that the low FSS-driven m6A modifications were closely associated with aging-related processes such as cell cycle and several signaling pathways including mTOR signaling pathway, PI3K-AKT signaling pathway, insulin signaling pathway, and ERBB signaling pathway. Low FSS mediated the arrest of cell cycle in both endothelial cell and tumor cells via the functions of p21 and SMAD family [43, 44]. The phosphorylation of SAMD2/3 was recently reported being activated at low FSS to mediate artery remodeling [45]. We found that the m6A of SMAD2/3 mRNAs were also differentially modified at low FSS, suggesting that low FSS regulated the SMAD signaling at not only posttranslational modification level but also posttranscriptional modification level. m6A was found to modulate mTOR and PI3K-AKT signaling pathway in many cancer cells, and the hypermethylation-mediated via METTL14 deactivated the PI3K-AKT and mTOR signaling and suppressed gastric cancer cell proliferation and aggression [46]. In our vascular endothelial cells, the mTOR and PI3K-AKT signaling genes were hypermethylated at low FSS, suggesting that it might inhibit the pathway activations and the cell proliferation as well as the roles in cancer cells. Therefore, the low FSS-driven m6A modifications might induce the cell cycle arrest and proliferation suppression. Together with the roles of m6A in oxidative stress, low FSS might promote endothelial cell aging via mediating abnormal modifications of m6A.

Mechanosensors for FSS such as protein of cytoskeleton, proteoglycan of heparan sulfate, and transmembrane of Ca^{2+} ions have been widely studied in last decades [47, 48]. Dynamic modifications, not only posttranslational modification but also posttranscriptional modification, were changed more immediately in cellular stress responses than their protein and mRNA backbones [49]. In our study, at the mRNA level and m6A modification level, we found that only one gene, MEGF6, shown a consistent trend of mRNA expression to the changes of FSS, while the m6A of 71 genes has the consistent trends to the changes of FSS. It suggested the m6A modifications were more suitable as biosensors of FSS than mRNA expressions. The changes of m6A modifications might be one of the initiated steps for vascular endothelial cells in response to abnormal FSS.

Aging is one of the key risk factors for cardiovascular disease [42]. As a pathological inducer for aging, low FSS mediated the endothelial dysfunctions and the development of almost all kinds of cardiovascular diseases such as atherosclerosis and abdominal aortic aneurysm [50, 51]. The relationship of low FSS with many conventional pathways has been intensively studied, while that with the posttranslational or transcriptional modifications were investigated just at the beginning step. Dynamic modifications provide the functional diversities for the modified backbones and play fine-tuning roles in many cellular processes [52]. Our study provided a proof-of-concept that low FSS mediated the dynamic changes of m6A in vascular endothelial cells which might participate in the regulating of oxidative stress and aging. Further experimental evidences were needed in future studies.

5. Conclusion

In summary, we performed the transcriptome-wide m6A modification profiling of HUVECs at different FSS. In comparison of the mRNA expressions, m6A modifications displayed a better linear relationship with the increasing of FSS, indicating that the m6A modifications were altered earlier and more sensitive than mRNA expressions in response to FSS. Compared to the physiological high FSS of 15 dyne/cm^2, the pathological low FSS of 5 dyne/cm^2 increased the m6A modifications at CDS region but decreased the m6A modifications at 3′ UTR region. Among the m6A regulators, the writer of RBM15 and the reader of EIF3A were both differentially expressed and differentially m6A-modified at low FSS. Functional enrichment analysis revealed that the annotations were enriched more by the hypomethylated genes at low FSS. In cellular response to oxidative stress, the m6A modifications were clustered at the cell cycle, apoptosis, and cellular senescence, which were aging-related processes. Further analysis confirmed that low FSS might regulate the aging process via altering the m6A modification of mTOR, PI3K-AKT, insulin, and ERRB signaling pathways and via hypomethylating the key transcriptional factors in the response to oxidative stress, such as HIF1A, NFAT5, and NFE2L2. Our study provided a pilot view of the dynamic changes of m6A modifications in vascular endothelial cells at low FSS and revealed that the m6A modifications driven by low FSS mediated the cellular responses to oxidative stress and cell aging, which also suggested that m6A modifications could be the potential targets for regulating vascular aging at pathological low FSS.

Abbreviations

CDS: Coding sequence
FSS: Flow shear stress
GO: Gene ontology
HUVECs: Human umbilical vein endothelial cells
KEGG: Kyoto encyclopedia of genes and genomes
m6A: N6-methyladenosine
MCODE: Molecular complex detection
MeRIP: Methylated RNA immunoprecipitation
mTOR: Mammalian target of rapamycin
ROS: Reactive oxygen species
UTR: Untranslated region.

Data Availability

The datasets are available from the corresponding authors upon reasonable request.

Conflicts of Interest

The authors declare that there is no conflict of interest regarding the publication of this paper.

Authors' Contributions

ZX, KY, XL, and GL designed the research. ZX, PQ, JH, and ZW carried out the experiment. ZX, PQ, YJ, JL, and HP analyzed the data. QH and XW collected the data. BL provided technical support. ZX and PQ wrote the manuscript. KY, XL, and GL reviewed and edited the manuscript. All authors provided final approval of the version to be submitted. Zhijue Xu, Peng Qiu, and Yihong Jiang have contributed equally to this work.

Acknowledgments

We thank Prof. Kaili Lin (Shanghai Ninth People's Hospital, Shanghai Jiao Tong University School of Medicine) for his kind support of the Flexcell Flow System and suggesting of the experimental design. This work was supported by the National Natural Science Foundation of China (Nos. 22007065, 82170509, 82170411, 81900410, and 81870346), the Open Research Program of National Facility for Translational Medicine (Shanghai) (No. TMSK-2021-121), the Chinese Postdoctoral Science Foundation (No. 2021M692117), the Shanghai Science and Technology Innovation Action Plan (Nos. 21Y11909500, 20Y11909600, and 21S31904300), the Shanghai Municipal Health Bureau Project (Nos. 202040434, 20224Y0170, and 202240145), and the Clinical Research Plan of SHDC (No. SHDC2020CR6016-003).

Supplementary Materials

Supplementary File. Figure S1: volcano plots of the differential expressed genes regulated by different flow shear stress. Figure S2: 3D and 2D PCA plots of the repeated cells exposed to different flow shear stress. (a) The gene mRNA expression level. (b) The m6A modification level. Figure S3: heatmap of the m6A-modified aging-related genes. Figure S4: the intact KEGG map of the insulin signaling pathway (up panel) and the PI3K-AKT signaling pathway (bottom panel). The ugregulated genes were colored in red, and the downregulated genes were colored in green. Figure S5: The intact KEGG map of the ERBB signaling pathway (up panel) and the mTOR signaling pathway (bottom panel). The ugregulated genes were colored in red, and the downregulated genes were colored in green. (Supplementary Materials). *(Supplementary Materials)*

References

[1] D. Dominissini, S. Moshitch-Moshkovitz, S. Schwartz et al., "Topology of the human and mouse m^{6}A RNA methylomes revealed by m^{6}A-seq," *Nature*, vol. 485, no. 7397, pp. 201–206, 2012.

[2] X. Y. Chen, J. Zhang, and J. S. Zhu, "The role of m(6)a RNA methylation in human cancer," *Molecular Cancer*, vol. 18, no. 1, p. 103, 2019.

[3] R. Winkler, E. Gillis, L. Lasman et al., "m^{6}A modification controls the innate immune response to infection by targeting type I interferons," *Nature Immunology*, vol. 20, no. 2, pp. 173–182, 2019.

[4] K. D. Meyer and S. R. Jaffrey, "Rethinking m(6)a readers, writers, and erasers," *Annual Review of Cell and Developmental Biology*, vol. 33, no. 1, pp. 319–342, 2017.

[5] K. D. Meyer, Y. Saletore, P. Zumbo, O. Elemento, C. E. Mason, and S. R. Jaffrey, "Comprehensive analysis of mRNA methylation reveals enrichment in 3′ UTRs and near stop codons," *Cell*, vol. 149, no. 7, pp. 1635–1646, 2012.

[6] X. Jiang, B. Liu, Z. Nie et al., "The role of m6A modification in the biological functions and diseases," *Signal Transduction and Targeted Therapy*, vol. 6, no. 1, p. 74, 2021.

[7] R. J. Ries, S. Zaccara, P. Klein et al., "m^{6}A enhances the phase separation potential of mRNA," *Nature*, vol. 571, no. 7765, pp. 424–428, 2019.

[8] A. Paramasivam, J. Vijayashree Priyadharsini, and S. Raghunandhakumar, "N6-adenosine methylation (m6A): a promising new molecular target in hypertension and cardiovascular diseases," *Hypertension Research*, vol. 43, no. 2, pp. 153-154, 2020.

[9] N. Baeyens, C. Bandyopadhyay, B. G. Coon, S. Yun, and M. A. Schwartz, "Endothelial fluid shear stress sensing in vascular health and disease," *The Journal of Clinical Investigation*, vol. 126, no. 3, pp. 821–828, 2016.

[10] D. E. Conway, M. T. Breckenridge, E. Hinde, E. Gratton, C. S. Chen, and M. A. Schwartz, "Fluid shear stress on endothelial cells modulates mechanical tension across VE-cadherin and PECAM-1," *Current Biology*, vol. 23, no. 11, pp. 1024–1030, 2013.

[11] C. L. Yankaskas, K. Bera, K. Stoletov et al., "The fluid shear stress sensor TRPM7 regulates tumor cell intravasation," *Science Advances*, vol. 7, no. 28, 2021.

[12] P. A. Galie, D. H. Nguyen, C. K. Choi, D. M. Cohen, P. A. Janmey, and C. S. Chen, "Fluid shear stress threshold regulates angiogenic sprouting," *Proceedings of the National Academy of Sciences of the United States of America*, vol. 111, no. 22, pp. 7968–7973, 2014.

[13] Y. Han, M. He, T. Marin et al., "Roles of KLF4 and AMPK in the inhibition of glycolysis by pulsatile shear stress in endothelial cells," *Proceedings of the National Academy of Sciences of the United States of America*, vol. 118, no. 21, 2021.

[14] S. M. Swain and R. A. Liddle, "Piezo1 acts upstream of TRPV4 to induce pathological changes in endothelial cells due to shear stress," *The Journal of Biological Chemistry*, vol. 296, article 100171, 2021.

[15] E. Tzima, M. Irani-Tehrani, W. B. Kiosses et al., "A mechanosensory complex that mediates the endothelial cell response to fluid shear stress," *Nature*, vol. 437, no. 7057, pp. 426–431, 2005.

[16] D. Meza, B. Musmacker, E. Steadman, T. Stransky, D. A. Rubenstein, and W. Yin, "Endothelial cell biomechanical responses are dependent on both fluid shear stress and tensile strain," *Cellular and Molecular Bioengineering*, vol. 12, no. 4, pp. 311–325, 2019.

[17] N. Baeyens, S. Nicoli, B. G. Coon et al., "Vascular remodeling is governed by a VEGFR3-dependent fluid shear stress set point," *eLife*, vol. 4, 2015.

[18] J. R. Moonen, E. S. Lee, M. Schmidt et al., "Endothelial-to-mesenchymal transition contributes to fibro-proliferative vascular disease and is modulated by fluid shear stress," *Cardiovascular Research*, vol. 108, no. 3, pp. 377–386, 2015.

[19] K. L. Nowak, M. J. Rossman, M. Chonchol, and D. R. Seals, "Strategies for achieving healthy vascular aging," *Hypertension*, vol. 71, no. 3, pp. 389–402, 2018.

[20] Z. Ungvari, S. Tarantini, A. J. Donato, V. Galvan, and A. Csiszar, "Mechanisms of vascular aging," *Circulation Research*, vol. 123, no. 7, pp. 849–867, 2018.

[21] V. M. Barodka, B. L. Joshi, D. E. Berkowitz, C. W. Hogue Jr., and D. Nyhan, "Review article: implications of vascular aging," *Anesthesia and Analgesia*, vol. 112, no. 5, pp. 1048–1060, 2011.

[22] G. G. Camici, G. Savarese, A. Akhmedov, and T. F. Luscher, "Molecular mechanism of endothelial and vascular aging: implications for cardiovascular disease," *European Heart Journal*, vol. 36, no. 48, pp. 3392–3403, 2015.

[23] T. J. Guzik and R. M. Touyz, "Oxidative stress, inflammation, and vascular aging in hypertension," *Hypertension*, vol. 70, no. 4, pp. 660–667, 2017.

[24] R. Alves-Lopes, K. B. Neves, A. C. Montezano et al., "Internal pudental artery dysfunction in diabetes mellitus is mediated by NOX1-derived ROS-, Nrf2-, and rho kinase-dependent mechanisms," *Hypertension*, vol. 68, no. 4, pp. 1056–1064, 2016.

[25] P. M. Psefteli, P. Kitscha, G. Vizcay et al., "Glycocalyx sialic acids regulate Nrf2-mediated signaling by fluid shear stress in human endothelial cells," *Redox Biology*, vol. 38, article 101816, 2021.

[26] B. Yang and Q. Chen, "Cross-talk between oxidative stress and m(6)A RNA methylation in cancer," *Oxidative Medicine and Cellular Longevity*, vol. 2021, Article ID 6545728, 26 pages, 2021.

[27] H. Chen, T. Zhao, D. Sun, M. Wu, and Z. Zhang, "Changes of RNA N^6-methyladenosine in the hormesis effect induced by arsenite on human keratinocyte cells," *Toxicology In Vitro*, vol. 56, pp. 84–92, 2019.

[28] X. Chen, C. Yu, M. Guo et al., "Down-regulation of m6A mRNA methylation is involved in dopaminergic neuronal death," *ACS Chemical Neuroscience*, vol. 10, no. 5, pp. 2355–2363, 2019.

[29] M. W. Dewhirst, "Relationships between cycling hypoxia, HIF-1, angiogenesis and oxidative stress," *Radiation Research*, vol. 172, no. 6, pp. 653–665, 2009.

[30] R. Wu, Y. Chen, Y. Liu et al., "m6A methylation promotes white-to-beige fat transition by facilitating Hif1a translation," *EMBO Reports*, vol. 22, no. 11, article e52348, 2021.

[31] B. Benassi, M. Fanciulli, F. Fiorentino et al., "C-Myc phosphorylation is required for cellular response to oxidative stress," *Molecular Cell*, vol. 21, no. 4, pp. 509–519, 2006.

[32] R. Su, L. Dong, C. Li et al., "R-2HG exhibits anti-tumor activity by targeting FTO/m(6)A/MYC/CEBPA signaling," *Cell*, vol. 172, no. 1-2, pp. 90–105 e23, 2018.

[33] H. Ryu, J. Lee, K. Zaman et al., "Sp1 and Sp3 are oxidative stress-inducible, antideath transcription factors in cortical

neurons," *The Journal of Neuroscience*, vol. 23, no. 9, pp. 3597–3606, 2003.

[34] E. Yankova, W. Blackaby, M. Albertella et al., "Small-molecule inhibition of METTL3 as a strategy against myeloid leukaemia," *Nature*, vol. 593, no. 7860, pp. 597–601, 2021.

[35] J. Tang, Q. Su, Z. Guo et al., "N6-methyladenosine(m(6)a) demethylase FTO regulates cellular apoptosis following cobalt-induced oxidative stress," *Environmental Pollution*, vol. 297, article 118749, 2022.

[36] Y. Guo, W. Song, and Y. Yang, "Inhibition of ALKBH5-mediated m6A modification of PPARG mRNA alleviates H/R-induced oxidative stress and apoptosis in placenta trophoblast," *Environmental Toxicology*, vol. 37, no. 4, pp. 910–924, 2022.

[37] M. Liu, Q. Yang, and J. Han, "Transcriptomic analysis reveals that coxsackievirus B3 Woodruff and GD strains use similar key genes to induce FoxO signaling pathway activation in HeLa cells," *Archives of Virology*, vol. 167, no. 1, pp. 131–140, 2022.

[38] Z. Dong, Z. Liu, P. Cui et al., "Role of eIF3a in regulating cell cycle progression," *Experimental Cell Research*, vol. 315, no. 11, pp. 1889–1894, 2009.

[39] X. Cai, Y. Chen, D. Man et al., "RBM15 promotes hepatocellular carcinoma progression by regulating N6-methyladenosine modification of YES1 mRNA in an IGF2BP1-dependent manner," *Cell Death Discovery*, vol. 7, no. 1, p. 315, 2021.

[40] X. Wang, G. Zhang, S. Dasgupta et al., "ATF4 protects the heart from failure by antagonizing oxidative stress," *Circulation Research*, vol. 131, no. 1, pp. 91–105, 2022.

[41] J. Wang, J. Zhang, Y. Ma et al., "WTAP promotes myocardial ischemia/reperfusion injury by increasing endoplasmic reticulum stress via regulating m(6)A modification of ATF4 mRNA," *Aging (Albany NY)*, vol. 13, no. 8, pp. 11135–11149, 2021.

[42] C. Collins and E. Tzima, "Hemodynamic forces in endothelial dysfunction and vascular aging," *Experimental Gerontology*, vol. 46, no. 2-3, pp. 185–188, 2011.

[43] K. Lin, P. P. Hsu, B. P. Chen et al., "Molecular mechanism of endothelial growth arrest by laminar shear stress," *Proceedings of the National Academy of Sciences of the United States of America*, vol. 97, no. 17, pp. 9385–9389, 2000.

[44] S. F. Chang, C. A. Chang, D. Y. Lee et al., "Tumor cell cycle arrest induced by shear stress: roles of integrins and Smad," *Proceedings of the National Academy of Sciences of the United States of America*, vol. 105, no. 10, pp. 3927–3932, 2008.

[45] H. Deng, E. Min, N. Baeyens et al., "Activation of Smad2/3 signaling by low fluid shear stress mediates artery inward remodeling," *Proceedings of the National Academy of Sciences of the United States of America*, vol. 118, no. 37, 2021.

[46] X. Liu, M. Xiao, L. Zhang et al., "The m6A methyltransferase METTL14 inhibits the proliferation, migration, and invasion of gastric cancer by regulating the PI3K/AKT/mTOR signaling pathway," *Journal of Clinical Laboratory Analysis*, vol. 35, no. 3, article e23655, 2021.

[47] Y. X. Qi, Y. Han, and Z. L. Jiang, "Mechanobiology and vascular remodeling: from membrane to nucleus," *Advances in Experimental Medicine and Biology*, vol. 1097, pp. 69–82, 2018.

[48] Y. X. Qi, J. Jiang, X. H. Jiang et al., "PDGF-BB and TGF-{beta}1 on cross-talk between endothelial and smooth muscle cells in vascular remodeling induced by low shear stress," *Proceedings of the National Academy of Sciences of the United States of America*, vol. 108, no. 5, pp. 1908–1913, 2011.

[49] X. Wang and C. He, "Dynamic RNA modifications in post-transcriptional regulation," *Molecular Cell*, vol. 56, no. 1, pp. 5–12, 2014.

[50] E. Cecchi, C. Giglioli, S. Valente et al., "Role of hemodynamic shear stress in cardiovascular disease," *Atherosclerosis*, vol. 214, no. 2, pp. 249–256, 2011.

[51] A. J. Boyd, D. C. Kuhn, R. J. Lozowy, and G. P. Kulbisky, "Low wall shear stress predominates at sites of abdominal aortic aneurysm rupture," *Journal of Vascular Surgery*, vol. 63, no. 6, pp. 1613–1619, 2016.

[52] J. Y. Roignant and M. Soller, "m^6A in mRNA: an ancient mechanism for fine-tuning gene expression," *Trends in Genetics*, vol. 33, no. 6, pp. 380–390, 2017.

Hindawi
Oxidative Medicine and Cellular Longevity
Volume 2023, Article ID 6237960, 17 pages
https://doi.org/10.1155/2023/6237960

Research Article

Mitochondrial Dysfunction and Increased DNA Damage in Vascular Smooth Muscle Cells of Abdominal Aortic Aneurysm (AAA-SMC)

Bengi S. Tavris,[1] **Andreas S. Peters**,[1,2] **Dittmar Böckler**,[1] **and Susanne Dihlmann**[1]

[1]*Klinik für Gefäßchirurgie und Endovaskuläre Chirurgie, Universitätsklinik Heidelberg, Im Neuenheimer Feld 420, 69120 Heidelberg, Germany*
[2]*Vaskuläre Biomaterialbank Heidelberg, Universitätsklinik Heidelberg, Im Neuenheimer Feld 420, 69120 Heidelberg, Germany*

Correspondence should be addressed to Susanne Dihlmann; susanne.dihlmann@med.uni-heidelberg.de

Received 9 August 2022; Revised 30 September 2022; Accepted 24 November 2022; Published 25 January 2023

Academic Editor: Ana Cipak Gasparovic

There is increasing evidence for enhanced oxidative stress in the vascular wall of abdominal aortic aneurysms (AAA). Mitochondrial damage and dysfunction are hypothesized to be actors in altered production of reactive oxygen species (ROS) and oxidative stress. However, the role of mitochondria and oxidative stress in vascular remodelling and progression of AAA remains uncertain. We here addressed whether mitochondrial dysfunction is persistently increased in vascular smooth muscle cells (VSMCs) isolated from AAA compared to healthy VSMC. AAA-derived VSMC cultures (AAA-SMC, $n = 10$) and normal VSMC cultures derived from healthy donors ($n = 7$) were grown *in vitro* and analysed for four parameters, indicating mitochondrial dysfunction: (i) mitochondrial content and morphology, (ii) ROS production and antioxidative response, (iii) NADP+/NADPH content and ratio, and (iv) DNA damage, in the presence or absence of angiotensin II (AngII). AAA-SMC displayed increased mitochondrial circularity (rounded shape), reduced mitochondrial area, and reduced perimeter, indicating increased fragmentation and dysfunction compared to healthy controls. This was accompanied by significantly increased O_2^- production, reduced NADP+/NADPH levels, a lower antioxidative response (indicated by antioxidative response element-(ARE-) driven luciferase reporter assays), more DNA damage (determined by percentage of γ-H2A.X-positive nuclei), and earlier growth arrest in AAA-SMC. Our data suggest that mitochondrial dysfunction and oxidative stress are persistently increased in AAA-SMC, emphasizing their implication in the pathophysiology of AAA.

1. Introduction

Vascular smooth muscle cells (VSMCs) are the major cell type in the vascular wall of the blood vessels and participate in both normal vascular function and pathologic processes such as atherosclerosis and aneurysms. They maintain vascular contractility and mechanical integrity of the vessel wall; regulate vascular tone; synthesize extracellular matrix proteins, such as elastin and collagens; and ensure normal vascular repair. For this purpose, VSMCs show a high plasticity and may change their cellular characteristics in response to many acute and chronic stimuli [1].

Within the aortic media, VSMCs ensure the dynamic properties of the aorta, which must withstand the constant mechanical stress of pulsatile blood flow. When the structural integrity of the aortic media is compromised, their VSMCs respond by inadequate or abnormal connective tissue synthesis, cytokine production, and recruitment of inflammatory cells. Aneurysms occur when the capacity of normal repair by VSMC is exhausted. More and more VSMCs change from a contractile to a synthetic phenotype, proliferate, and migrate, which results in thickening of the aortic wall. The increasing diffusion distance from the lumen and the luminal narrowing of the vasa vasorum (i.e., caused

by hypertension) cause ischemia of the media, resulting in VSMC loss as well as aortic degenerative changes. In addition, excessive connective tissue degradation by infiltrating leukocytes contributes to progressive weakening of the vessel wall [2, 3].

Abdominal aortic aneurysm (AAA) is the most common form of aneurysmal disease with chronic dilation typically presenting in the infrarenal region. It is positively associated with male sex, advanced age (above 60 years) and smoking habits [4]. In the absence of treatment, the main complication of AAA is rupture, which is life-threatening and still leads to death in up to 50% of the affected patients, despite modern, minimal invasive treatment modalities [5]. The treatment of progressing AAA before rupture comprises open surgical or endovascular strategies, which are associated with high physical stress and morbidity for the patients [6]. Notably, no specific drugs are available so far to decelerate AAA growth or prevent rupture [7], which is why more research is needed to investigate contribution of cellular processes to AAA progression.

According to histological analyses of human AAA samples, leukocytic infiltration, degradation of extracellular matrix, and disruption of VSMC plasticity and function are the main pathophysiological hallmarks of AAA [4]. Moreover, elevated amounts of reactive oxygen species (ROS) and oxidative stress have been described in histological AAA samples [8–11], particularly within the thrombus-covered aneurysm wall [12]. Because overproduction of ROS and oxidative stress are known to induce inflammation, VSMC apoptosis, and degradation of extracellular matrix in the vascular wall [4, 9], they are particularly interesting targets for pharmaceutical interventions to decelerate AAA growth and prevent rupture. However, the dynamics of ROS production and oxidative stress during AAA pathophysiology are incompletely understood.

Recent studies suggest the involvement of mitochondria and mitochondria-derived oxidative stress in the development of AAA. Using an established animal model of angiotensin II- (AngII-) induced aortic aneurysm, mitochondrial stress in macrophages was identified as a driving force of aneurysm growth [13]. In addition, mitochondria in other cell types, i.e., in VSMC and endothelial cells, might also be involved in AAA, because they are known to control numerous physiological processes in the blood vessels. Endothelial cell mitochondria are involved in calcium homeostasis, apoptosis/necrosis, response to cell stress, and regulation of inflammatory signalling pathways [14]. Mitochondria are also involved in cellular signalling pathways in VSMC. Via physiological ROS production, especially H_2O_2, they control essential functions of these cells such as proliferation, migration, differentiation to the contractile or synthetic phenotype, and vascular resistance induced by contraction [15].

Notably, we recently demonstrated that mice with a deficiency of the mitochondrial enzyme nicotinamide-nucleotide-transhydrogenase (Nnt) are more susceptible to AngII-induced aortic aneurysms than their Nnt-proficient counterparts. According to our results, the Nnt-deficient VSMC displayed increased oxidative stress, oxidative DNA damage, and a stronger inflammatory phenotype [16]. This led us to speculate that also the mitochondria of aortic VSMC may be important players in AAA growth. Our assumption is supported by further observations. For example, excess ROS production in mitochondria, resulting in vascular oxidative stress, is associated with two of the main risk factors for AAA: aging and smoking [4, 17]. Tobacco smoke contains several reactive oxygen and nitride species and causes indirect ROS production through toxicants, carcinogens, and metals found in the smoke [18]. Both might affect mitochondrial dynamics and function in VSMC of the aneurysm wall. Finally, AngII, a potential contributor to AAA, was recently shown to induce dysregulation of the mitochondrial life cycle, characterized by excess fission relative to fusion of damaged vascular mitochondria [19].

Given the broad functional range of tasks in aortic VSMC, mitochondrial function and its interaction with ROS production in AAA-derived VSMC (AAA-SMC) are promising targets for future therapeutics. Previous studies have analysed oxidative stress by histological analysis in tissues derived from AAA [8, 10–12]. However, mitochondrial life cycle and ROS-induced damage are dynamic processes, which are continuously counterbalanced in living cells. Because AAA tissues undergo ischemic stress when removed from the patients and are immediately fixed by cryopreservation or chemical agents for further analysis, tissue analysis does not allow to investigate mitochondrial function in living VSMC. Therefore and in contrast to previous studies, we here addressed mitochondrial dysfunction and oxidative stress in AAA-SMC cultures versus healthy controls in *in vitro* studies. Our data present evidence that mitochondrial dysfunction and oxidative stress are persistently increased in AAA-SMC when compared with healthy VSMC, which further supports their implication in the pathophysiology of AAA.

2. Materials and Methods

2.1. Vascular Smooth Muscle Cell (VSMC) Cultures. Human VSMCs derived from male healthy donors ($n = 5$, age 13-68 years) were purchased from PromoCell (Heidelberg, Germany). In addition, primary vascular smooth muscle cells were isolated from healthy carotid arteries ($n = 2$, age 67 and 82). AAA-SMCs were isolated from human abdominal aortic aneurysm biopsies that were obtained during open surgery ($n = 10$, age 49-74). All procedures were performed according to the standard operating procedures of the Vascular Biobank Heidelberg (VBBH), as previously described [20]. Details of the cell cultures are described in supplementary table S1. All patients gave their written informed consent to the study, which was approved by the ethical committee of the University of Heidelberg (S-301/2013 and amendments; S-091/2021). Briefly, aneurysmatic tissue samples were obtained from apparently noncalcified areas of male adult patients undergoing elective open surgery for repair of their AAA. VSMCs were grown in Smooth Muscle Cell Growth Medium 2 (SMC-GM2; PromoCell, Heidelberg, Germany) supplemented with 100 U/ml penicillin and 100 U/ml streptomycin (Thermo Fisher Scientific, Gibco,

Germany) at 37°C and 5%CO_2 in a humidified atmosphere. For subculturing, the cells were split 1 : 2 when reaching 80-90% confluence. The medium was changed twice a week for routine growth independent of splitting. Three to seven cell cultures at passages 5 to 10 were used for each experiment in this study. A few days before and during the experiments, cells were grown without antibiotics.

2.2. MitoTracker Staining and Mitochondrial Morphology Analysis. Cells were seeded on cover slips and treated as indicated in the figure legends. After washing, cells were stained with MitoTracker Red CMXRos (Thermo Fisher Scientific, Waltham, USA) at a final concentration of 180 nM in Smooth Muscle Cell Growth Medium 2 at 37°C 5% CO_2 for 30 minutes prior to fixation with paraformaldehyde as described above. After final washing for three times, ProLong Antifade Gold Mountant with DAPI (Thermo Fisher Scientific, Waltham, USA) was applied to counterstain cell nuclei. Cells were visualized under a fluorescence microscope (Zeiss Axiostar Plus) with 40x objective, and photos were taken for further analysis. Four to six individual cells were captured and analysed per cell line by using the mitochondrial morphology macro for ImageJ designed by Ruben K. Dagda (https://imagejdocu.list.lu/plugin/morphology/mitochondrial_morphology_macro_plug-in/start [21]. For the characterization of mitochondrial dysfunction, fusion, and fission in VSMC, four main parameters were considered: (1) count: number of mitochondrial particles counted; (2) Mito content: average percentage of cytoplasm occupied by mitochondria per cell; (3) average perimeter: average perimeter of mitochondria (in μm); (4) average circularity: average circularity of mitochondria, 1 being a perfect circle and 0 being a perfect line; and (5) mitochondrial fission count (MFC) was calculated using ImageJ data (mitochondria count × 100/mitochondrial area (%area of cell) per cell).

2.3. Total DNA Extraction and Quantification of mtDNA Copy Number by Real-Time PCR. Total DNA was isolated from 1×10^6 cells of each culture using DNeasy Blood and Tissue Kit (Qiagen, Hilden, Germany) according to the instructions of the manufacturer. At the final step, DNA was eluted in 100 μl nuclease-free water. Quantification of mtDNA copies/cell was performed as described previously [18, 22]. Briefly, human nicotinamide adenine dinucleotide (reduced) (NADH) dehydrogenase 1 (MTND1) cDNA clone (SC101172, OriGene Technologies, Rockville, MD, USA) was used as a standard for mtDNA copy number. Equivalents of 10^9, 10^8, 10^7, 10^6, 10^5, 10^4, 10^3, 10^2, 10^1, and 10^0 copies of a plasmid encoding the MTND1 cDNA were amplified by PCR with an ABI StepOne Plus cycler, and a standard curve was generated by plotting the copy numbers against the cycles at a threshold of 0.4. Primer sequences were as follows: forward CGAGCAGTAGCCCAAACAAT and reverse TGTGATAAGGGTGGAGAGGTT. For analysis of the VSMC samples, 1 μl of total DNA extract from each culture was inserted into PCR. Details of the PCR protocol are available upon request. The cycle numbers obtained at a threshold of 0.4 from each sample were converted to total copy number by using the formula derived from the standard curve. The copy number/cell was calculated as follows: $C = Q \times V_{DNA}/V_{PCR} \times 1/V_{EXT}$, where C is the copy number/cell, Q is the quantity (total copy number) of DNA determined by the sequence detector in the PCR, V_{DNA} is the volume of cell DNA obtained after extraction (100 μl), V_{PCR} is the volume of cell DNA solution used for PCR, and V_{EXT} is the number of cells used for DNA extraction.

2.4. Transfection and Luciferase Reporter Assays. Transfection of VSMC was performed by electroporation, using the Neon transfection system (Thermo Fisher, Scientific, Waltham, USA) as recommended by the manufacturer. Briefly, proliferating VSMCs (passages 4-8) were harvested and resuspended in Buffer R of the Neon transfection system 100 μl kit (Thermo Fisher, Scientific, Waltham, USA) at a density of 10^7 cells/ml. 100 μl of the cell suspension was mixed with a reporter plasmid mix using a 100 μl Neon tip. For analysis of oxidative stress response, the antioxidant response reporter plasmid pNL[NlucP/ARE/Hygro] and reference reporter plasmid pGL4.13[luc2/SV40] were mixed at a ratio of 100 : 1 and a final concentration of 1 μg/μl. Electroporation was performed at 1475 volts with a pulse width of 20 ms and a pulse number of 2. The transfected cell suspension was diluted in 5 ml prewarmed medium (SMC-GM2) without antibiotics, and 100 μl per well was seeded into white 96-well plates (resulting in 20000 cell/well). Cells were incubated at 37°C and 5% CO_2 overnight to recover before further treatments were performed as indicated. After transfection and recovery, cells were treated with human AngII (Sigma, Merck, Darmstadt, Germany) in 80 μl medium/well at different concentrations for 3 h or 24 h, respectively, or left untreated (control) as described in the figure legends. For detection of luciferase activity, dual luminescence was measured using the Nano-Glo Dual-Luciferase Reporter Assay System (Promega, Walldorf, Germany), following the protocol of the manufacturer. Briefly, plates were equilibrated to room temperature and 80 μl of One-Glo Ex Luciferase reagent was added to each well. Plates were mixed for 3 min at 240 rpm, and firefly luminescence was measured using a TECAN spark multiplate reader. Next, NanoDLR Stop & Glo Reagent was prepared (diluted 1 : 100 in buffer) and 80 μl was added to each well. Plates were mixed by shaking for 3 min and incubated at room temperature for 10 min. NanoLuc luciferase was measured, again using the TECAN spark reader. Relative luminescence (RLU) was calculated by dividing the signal intensities of the NanoLuc luciferase by the signal intensities of the firefly luciferase.

2.5. Detection and Quantification of Hydrogen Peroxide Levels Using ROS-Glo H_2O_2 Assay. VSMC were seeded at 1×10^4 cells per well in a 96-well plate and serum-deprived overnight. Detection of H_2O_2 was performed with ROS-Glo H_2O_2 assay (Promega, Walldorf, Germany) as described by the manufacturer. Briefly, cells were treated for different lengths of time with 40 μl complete medium (control) or AngII at 1 μmol/l and/or MitoQ (mitoquinone mesylate, Biozol, Eching, Germany) at 100 nmol/l in 40 μl complete SMC-GM2, at 37°C and 5% CO_2 in a humidified

atmosphere. For detection after 2 h, 10 μl of H_2O_2 substrate solution was added immediately at the start of the treatment. For detection after 6 h and 24 h, 10 μl of H_2O_2 substrate solution was added 6 h before measurement. After treatment, 50 μl of ROS-Glo Detection Solution was added and cells were incubated for 20 min, before luminescence was measured with a TECAN plate reader.

2.6. Detection and Quantification of Superoxide Anion (O_2^-) Levels Using CellROX Green Assay. VSMCs were seeded at 1×10^4 cells per well in a 96-well plate and serum-deprived overnight. Detection of O_2^- was performed with CellROX Assay (Thermo Fisher, Invitrogen) as described by the manufacturer. Briefly, cells were treated with complete medium (control) or AngII at 1 μmol/l and/or MitoQ at 100 nmol/l in complete SMC-GM2, as described in the figure legends. After treatment, cells were washed three times with phosphate-buffered saline (PBS) and 50 μl of CellROX green reagent was added. Cells were incubated for 30 min at 37°C and 5% CO_2 in a humidified atmosphere, before fluorescence was measured with a TECAN plate reader at an excitation wavelength of 485 nm and an emission wavelength of 535 nm.

2.7. NADP+/NADPH Assays. Analysis of total NADP+/NADPH levels was performed with NADP/NADPH-Glo Assay (Promega, Walldorf, Germany), according to the instructions of the manufacturer. Briefly, VSMCs were seeded in 96-well plates at different densities (1×10^3, 4×10^3, and 8×10^3 cells/well) in 100 μl complete growth medium and incubated at 37°C and 5% CO_2 overnight. Next, 50 μl of NADP/NADPH-Glo Detection Reagent (prepared as recommended by the manufacturer) was added to each well and luminescence was measured as relative light units (RLU) after 60 min with a TECAN Spark multiplate reader. For analysis of the NADPH/NADP+ ratio, 8000 cells per well were seeded with or without AngII (1 μM) in 100 μl complete growth medium and incubated overnight. Cells were washed with DPBS and lysed with 0.2 N NaOH solution containing 1% DTAB (dodecyltrimethylammonium-bromid) by shaking of the plates for 15 min. Cell lysates (100 μl each) were used immediately for analysis or cryopreserved at -80°C, before oxidized (NADP+) and reduced (NADPH) levels were analysed separately, as recommended by the manufacturer. Briefly, 50 μl of each lysate was transferred to an empty well for acid treatment (NADP+ measurement) and 50 μl of each lysate was transferred to another well for base treatment (NADPH measurement). To measure NADP+, 25 μl of 0.4 N HCl was added per well and heated to 60°C for 15 min. To measure NADPH, samples were directly heated to 60°C for 15 min. Samples were equilibrated for 10 min at room temperature, before 25 μl of 0.5 M Trizma® base was added to each well of the acid-treated cells, and 50 μl of HCl/Trizma® solution was added to each well of base-treated samples. Next, 100 μl of NADP/NADPH-Glo™ Detection Reagent was transferred to each well and luminescence was measured after 60 min with a TECAN Spark multiplate reader.

2.8. Immunofluorescence Staining of γ-H2A.X and Analysis of DNA Damage. Cells were seeded on cover slips in complete SMC-GM2 per well and grown overnight at 37°C and 5% CO_2. The medium was replaced with AngII-containing medium at different concentrations (0 nM, 10 nM, 100 nM, or 1000 nM) and incubated for another 24 h. H_2O_2-(100 μM) containing medium was used as a positive control. Cells were washed three times with Dulbecco's phosphate-buffered saline (DPBS), with 0.1% Tween 20 and fixed in 4% paraformaldehyde for 10 min at room temperature. After additional washing, cells were permeabilized with 0.1% Triton X-100 in DPBS for 10 minutes and blocked with 2% albumin fraction + 2%FBS in washing buffer for 1 hour. Primary antibody (Phospho-Histone H2A.X (Ser139), Cell Signaling Technology Europe, Frankfurt, Germany, #2577; dilution 1 : 400) was added overnight in a humidified chamber at 4°C. Cover slips were washed again three times, before the secondary antibody (Anti-rabbit IgG Fab2 Alexa Fluor 488, Cell Signaling Technology Europe, Frankfurt, Germany, #4412; dilution 1 : 500) was added for one hour. After final washing for three times, ProLong Antifade Gold Mountant with DAPI (Thermo Fisher Scientific, Waltham, USA) was applied to counterstain cell nuclei. Cells were visualized under a fluorescence microscope (Zeiss Axiostar Plus) with 40x objective, and photos were taken for further analysis. Eight to 15 images were captured for each treatment group per cell line. For quantification, the total number and the number of γ-H2A.X-positive nuclei were determined from the pictures to obtain the percentage of positive nuclei.

2.9. Immunofluorescence Staining of p21Waf1/Cip1. Cells were seeded on cover slips and grown overnight at 37°C and 5% CO_2 in SMC-GM2 with reduced serum (1% supplement) to synchronize the cell cycle. After three times washing with PBS, cells were fixed and permeabilized as described above, before blocking buffer (5% goat serum, 0.3% Triton™ X-100 in PBS) was added for 1 h. Primary antibody (p21Waf1/Cip1(12D1), Cell Signaling Technology Europe, Frankfurt, Germany, #2947; dilution 1 : 500) was added overnight in a humidified chamber. Further processing and addition of the secondary antibody were performed as described above. Cells were visualized under a fluorescence microscope (Zeiss Axiostar Plus) with 20x objective, and photos were taken for further analysis. Two to three images were captured for each treatment group per cell line. Quantification of p21-positive nuclei was performed with FIJI/ImageJ.

2.10. WST-1 Proliferation Assay. The WST-1 proliferation assay (Sigma Aldrich, Taufkirchen, Germany) was used for analysis, as described by the manufacturer. Briefly, cells were grown overnight in 96-well plates at a density of 1×10^4 cells/well in 100 μl SMC-GM2 with reduced serum (1% supplement) to synchronize the cell cycle. Assays were initiated by changing the medium to complete SMC-GM2, and cells were grown for another 0 h (start), 24 h, 48 h, and 72 h as described in the figure legends. For analysis, 10 μl of WST-1 proliferation reagent was added to each well and absorbance was measured at 450 nm versus 620 nm with a

TECAN Spark reader, as recommended by the manufacturer. To determine the relative proliferation rate, all data (A450-A620) were normalized to the absorbance at the start. All experiments were performed in triplicate.

2.11. Apoptosis Assay. Apoptotic cells were quantified by using the bioluminescent Caspase-Glo 3/7 Assay Systems (Promega, Walldorf, Germany) as described by the manufacturer. Briefly, cells were grown overnight in 96-well plates at a density of 1×10^4 cells/well in SMC-GM2 with reduced serum (1% supplement) to synchronize the cell cycle. Assays were initiated by changing the medium to 50 μl complete SMC-GM2, and cells were grown for another 0 h (start), 24 h, 48 h, and 72 h as described in the figure legends. For analysis, 50 μl of the Caspase-Glo® 3/7 Reagent was added to each well and Caspase-Glo 3/7 activity was measured as relative light units (RLU) with a TECAN Spark reader.

2.12. Statistical Analysis. Three to eight individual cell cultures were analysed in triplicate to quintuplicate for each experiment. Data were processed by using the GraphPad Prism software (version 9.0.0). Pairwise comparison was performed using the Mann–Whitney *U* test or Wilcoxon rank sum test as nonparametric tests or Student's *t*-test as parametric test. Multiple comparisons were performed by 2-way ANOVA and additional tests as described in the figure legends.

3. Results

3.1. Morphological Analysis Indicates Increased Mitochondrial Fission in AAA-SMC. To investigate mitochondrial morphology and dynamics, AAA-SMC and healthy VSMC were stained with MitoTracker Red CMXRos (Figure 1(a)) and mitochondria were analysed microscopically for four parameters as previously described [21]. The mitochondrial particle count per cell did not differ significantly between AAA-SMC and healthy VSMC (Figure 1(b)). In contrast, the percentage of cytoplasm occupied by mitochondria was significantly reduced in AAA-SMC (median = 3.0%) compared with healthy VSMC (median = 17.5%), indicating a lower mitochondrial mass in AAA-SMC (Figure 1(c)). The median mitochondrial perimeter was as well significantly lower in AAA-SMC than in healthy VSMC ($\text{median}_{\text{AAA-SMC}}$: 13.0 μm versus $\text{median}_{\text{healthy VSMC}}$: 26.0 μm) (Figure 1(d)).

Finally, the average circularity of mitochondria was significantly higher in AAA-SMC compared with healthy VSMC (Figure 1(e)). Taken together, AAA-SMC contained less mitochondrial bodies, which were smaller and rounder than those in healthy VSMC. Accordingly, the mitochondrial fission count was elevated in AAA-SMC (Figure 1(f)), indicating increased mitochondrial damage in these cells.

Because of the different degree of fusion of mitochondria, the number of mitochondrial bodies does not exactly reflect their individual number. We therefore performed a mitochondrial DNA- (mtDNA-) specific real-time quantitative PCR [18] using the human MTND1 gene, which is encoded in the mitochondrial genome, to generate a standard curve. The mtDNA copy number per cell was significantly higher in AAA-SMC (median = 494 copies/cell) than in healthy VSMC (median = 197 copies/cell, Figure 1(g)).

3.2. The Antioxidant Stress Response Is Affected in AAA-SMC. Given that mitochondrial dysfunction is particularly driven by oxidative stress [23, 24], we next determined the antioxidant stress response of AAA-SMC versus healthy VSMC. Cells were transfected with a plasmid containing the antioxidant response element (ARE) driving NanoLuc luciferase as a reporter gene. ARE is an enhancer element that is found in several genes encoding detoxification enzymes and initiates a pathway to protect cells from oxidative stress-induced cell death when activated by the transcription factor Nrf2 (nuclear factor erythroid 2-related factor 2) [25, 26].

In untreated cells, ARE activity did not differ between healthy VSMC and AAA-SMC (Figure 2(a)). To increase oxidative stress, we challenged the cells with AngII, which has been reported to induce ROS production, thereby mediating oxidative DNA damage and senescence in VSMC [27, 28]. Treatment of the cells with increasing doses of AngII for 3 h resulted in a significant linear increase of the ARE response in healthy VSMC (Figure 2(b)) but not in AAA-SMC (Figure 2(c)). No difference was observed after 24 h of AngII treatment (supplementary figure S1). This suggests that the response to AngII-mediated oxidative stress is affected in AAA-SMC. Results of the individual cell cultures may be found in supplementary figure S2.

3.3. Oxidative Stress and ROS Production. Increased oxidative stress has been found in human and mouse AAA tissues [10, 13, 29, 30] and was mainly localized to infiltrating macrophages within the adventitia [13], infiltrating inflammatory cells, and VSMC [30], by using in situ imaging. To address mitochondrial ROS production in VSMC *in vitro*, we next determined the levels of superoxide anions (O_2^-) and hydrogen peroxide (H_2O_2) in untreated and AngII-challenged SMC cultures in the presence or absence of the mitochondrial-specific antioxidant MitoQ, which was shown to reduce ROS production in VSMC [28]. After three hours of treatment, the amount of O_2^- was significantly higher in AAA-SMC than in healthy VSMC (Figure 3(a)), and MitoQ treatment significantly decreased the amount of O_2^- in healthy VSMC, both in controls and in AngII-challenged cell cultures (Figure 3(b)).

In AAA-SMC, the amount of O_2^- was also reduced by MitoQ, but to a lower extent. This indicates that O_2^- production derived from mitochondria is increased in AAA-SMC. No significant differences in the amount of O_2^- were observed after 24 h of treatment (supplementary figure S3a and b). In contrast, the amount of H_2O_2 was unaffected after two hours of treatment (supplementary figure S3c), both in healthy and in AAA-SMC but displayed clear differences after 24 h of treatment, when H_2O_2 levels were clearly higher in healthy VSMC cultures than in AAA-SMC (Figure 3(c)). Moreover, the amount of H_2O_2 was significantly increased in MitoQ-treated cells after 24 h, again with a stronger effect in healthy VSMC than in AAA-SMC (Figure 3(d)).

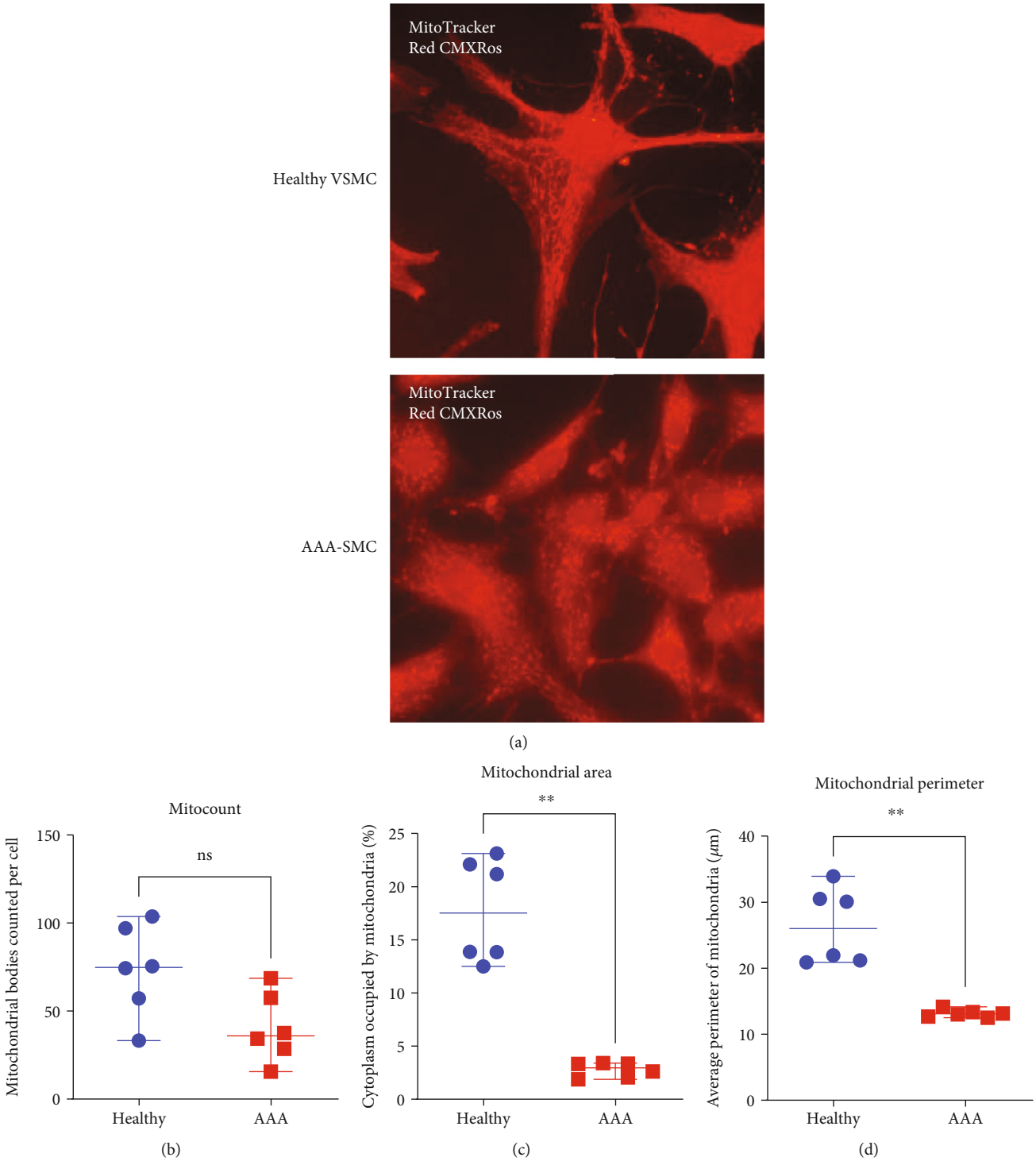

Figure 1: Continued.

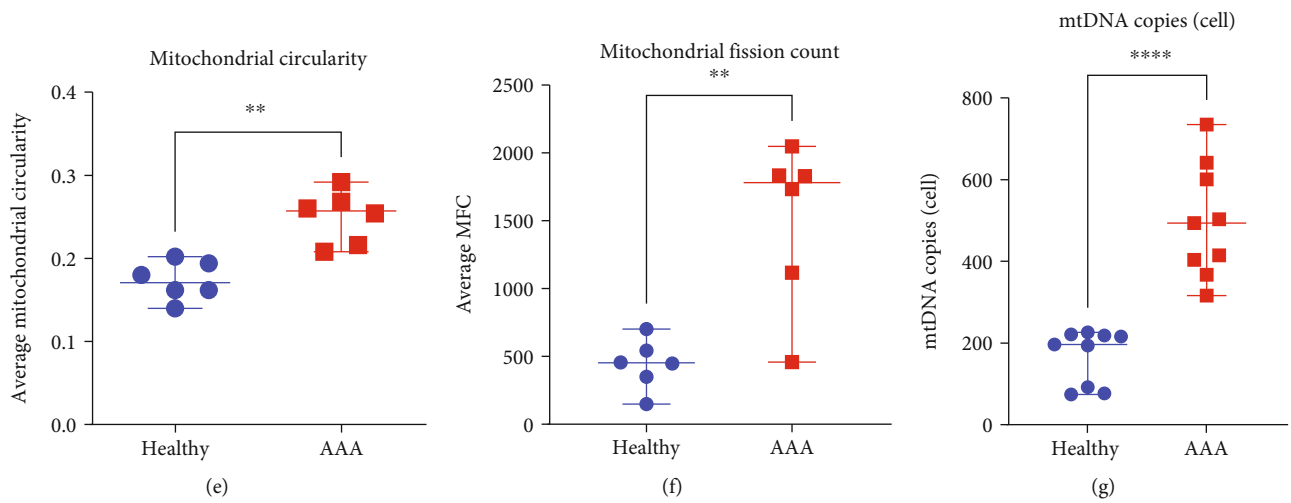

Figure 1: (a) Representative images of healthy VSMC ($n = 6$ cultures) and AAA-SMC ($n = 6$ cultures) stained with MitoTracker Red CMXRos. Mitochondrial particle count per cell (b), mitochondrial area (c), mitochondrial perimeter (d), and mitochondrial circularity (e) were determined by ImageJ as described in Materials and Methods. (f) Mitochondrial fission count was calculated using ImageJ data (mitochondria count × 100/mitochondrial area (%area of cell) per cell = MFC). (g) The number of mitochondrial DNA copies per cell was determined by real-time PCR. Data points represent the means of each culture (4-6 cells were captured per cell culture) and are shown with median and range. Data were analysed with the Mann–Whitney U test; $^{**}p < 0.01$ and $^{****}p < 0.0001$, ns: not significant.

AngII treatment elicited similar effects on ROS production as MitoQ treatment. After 3 h of treatment, O_2^- production was significantly reduced in healthy VSMC (Figure 3(b)), resulting in an increased H_2O_2 production after 24 h (Figure 3(d)). Again, the effect of AngII on ROS production was much weaker and not significant in AAA-SMC (Figures 3(a)–3(d)).

3.4. AAA-SMCs Contain Less NADPH/NADP+ Than Healthy VSMC. Nicotinamide adenine dinucleotide phosphate (NADP+) and its reduced form (NADPH) play critical roles in both antioxidation system and generation of oxidative stress [31, 32]. Because they are predominantly located in mitochondria [31], we used a bioluminescent NADP/NADPH-Glo Assay to determine the total amount and the ratio of NADPH/NADP+ as surrogates for mitochondrial function in VSMC. The median total amount of NADP+/NADPH was found to be significantly lower in AAA-SMC than in healthy VSMC (Figure 4(a)), indicating a reduced metabolic activity. Treatment of the cells with AngII did not change the total amount of NADPH/NADP+, neither in healthy nor in AAA-SMC (supplementary figure S4). In contrast to the total amount, the NADPH/NADP+ ratio did not differ significantly between healthy and AAA-SMCs (Figure 4(b)).

3.5. Elevated γ-H2A.X Presence Indicates Increased DNA Damage in AAA-SMC in Response to AngII. Excessive ROS levels produced by dysfunctional mitochondria can cause severe oxidative damage to macromolecules, especially the DNA [33]. We therefore evaluated DNA double-strand breaks in AAA-SMC ($n = 7$ cultures) and healthy VSMC ($n = 7$ cultures) by immunostaining for γ-H2A.X foci after 3 h (Supplementary Figure S5) and 24 h (Figure 5) of treatment with different concentrations of AngII. Gamma-H2A.X is a phosphorylated histone protein, which is required for checkpoint-mediated cell cycle arrest and DNA repair following double-strand breaks and represents a very early event in DNA damage response [34].

Gamma-H2A.X positive nuclei were observed to appear in a wide spectrum from singular small foci to staining of the whole nucleus (Figure 5(a)). The percentage of γ-H2A.X-positive nuclei did not differ significantly between AAA-SMC and healthy VSMC in untreated cells and in response to short-time AngII exposures (Supplementary Figure S5). When the cells were treated with 1 μM AngII for 24 h, the percentage of γ-H2A.X-positive nuclei increased significantly in AAA-SMC, when compared with untreated cells and with healthy VSMC, indicating an increased number of cells with double-strand breaks. (Figure 5(b)).

3.6. AAA-SMCs Are Subject to Earlier Growth Arrest Than Healthy VSMC. The identification of mitochondrial dysfunction, altered metabolic activity, and increased sensitivity towards DNA damage prompted us to investigate proliferation of AAA-SMC versus healthy VSMC by using a WST-1 proliferation assay and a Caspase-3/7 Apoptosis Assay. The mean number of viable cells was similar in healthy VSMC and AAA-SMC at 24 h, 48 h, and 72 h after initiation of the assay (Figure 6(a) and Supplementary figures 6 and 7). In contrast, the proportion of apoptotic cells in healthy VSMC increased continuously, whereas it remained unchanged in AAA-SMC (Figure 6(b)).

Thus, healthy VSMCs balance apoptosis by increased proliferation, whereas AAA-SMCs grow slowly, despite very little apoptosis. Together, this indicates that AAA-SMCs stop proliferating earlier than healthy VSMCs. In line with this observation, the amount of the cell cycle inhibitor and DNA damage checkpoint marker p21Waf1/Cip1 was increased in AAA-SMC grown for 72 hours (Figure 6(c)),

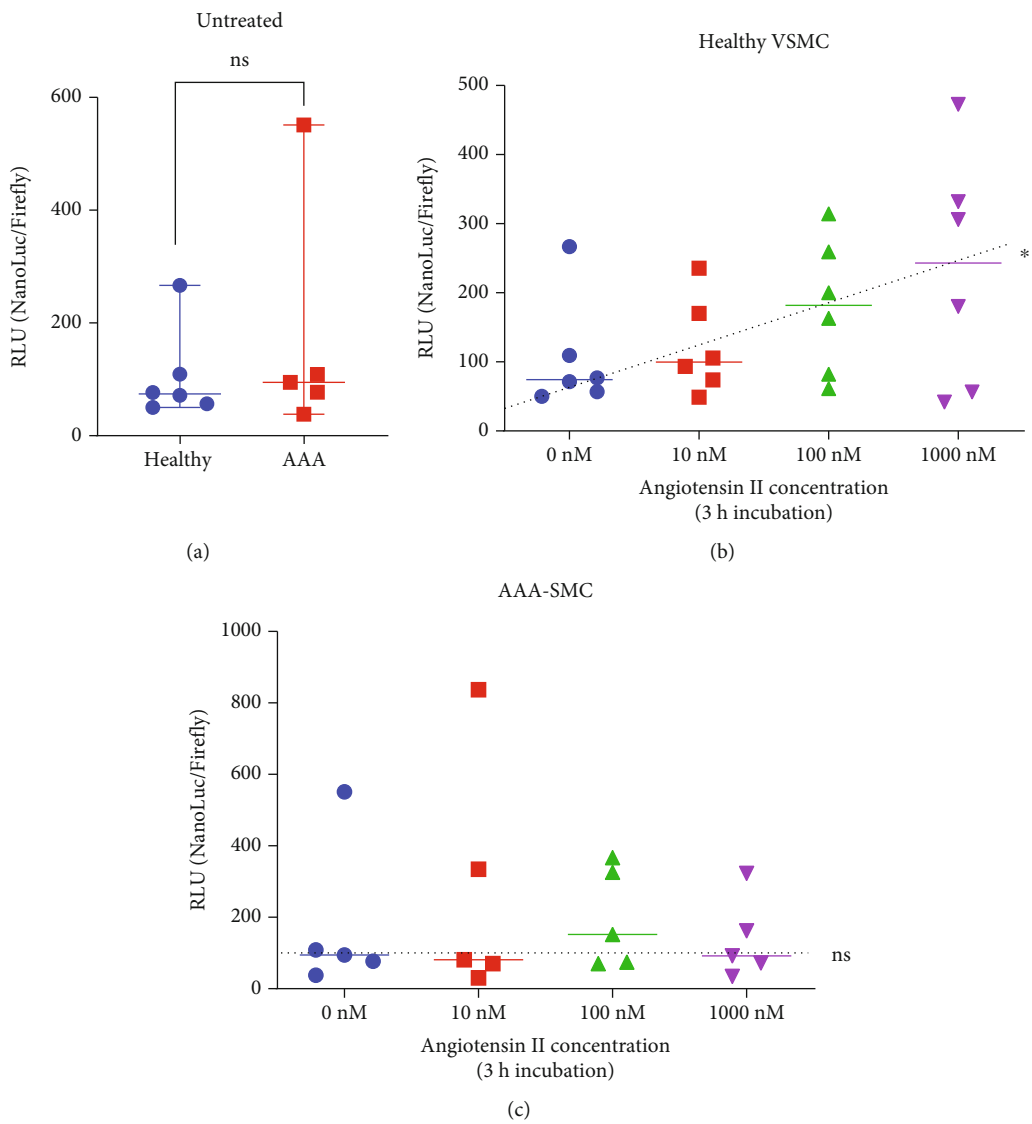

Figure 2: Antioxidative response element (ARE) activity was analysed in healthy ($n = 6$) and AAA-VSMC ($n = 5$) cultures following 3 h of AngII treatment at 0, 10, 100, and 1000 nM concentrations. ARE activity was determined as relative luminescence (RLU) of the ARE-driven NanoLuc luciferase divided by the RLU of a reference firefly luciferase. (a) ARE activity in untreated cells. Data points represent the means of four replicates per culture and are shown with median and range of all cultures. Statistical analysis was performed with the Mann–Whitney U test. ns: not significant. (b, c) ARE activity in healthy VSMC (b) and AAA-SMC (c) as a function of 3 h treatment with different doses of AngII. Data points represent the means of four replicates per culture and are shown with median. Ordinary one-way ANOVA was performed to test for a linear trend. $^{*}p < 0.05$. The dotted line represents the trend line.

indicating that the cells do not pass the DNA damage/G2 checkpoint. No additional effect on cell viability and p21 expression was observed, when the cells were treated with AngII for 72 hours (Figure 6(c) and supplementary figures 6 and 7), indicating that AngII had no effect on the proliferation rate.

4. Discussion

In this paper, we characterized mitochondrial oxidative stress in AAA-SMC in comparison to healthy VSMC, grown *in vitro*. Our data present evidence that mitochondria in AAA-derived VSMC are permanently and more severely damaged than those of healthy VSMC derived from age-matched controls. We have also highlighted the role of AngII, which appears to exert different effects on ROS production in healthy and aneurysm-damaged cells, respectively. So far, most studies of VSMC physiology, metabolism, and therapeutic targets have been performed in single cultures of healthy cells, ignoring the fact that many processes may be different in cells from diseased tissue and between individuals. Therefore, our approach was to separately study and compare the mitochondrial function of individual VSMC cultures from different healthy and aneurysmal aortas, at early passages after isolation from the tissue.

Under physiological conditions, ROS production in vascular mitochondria is at a low level. However,

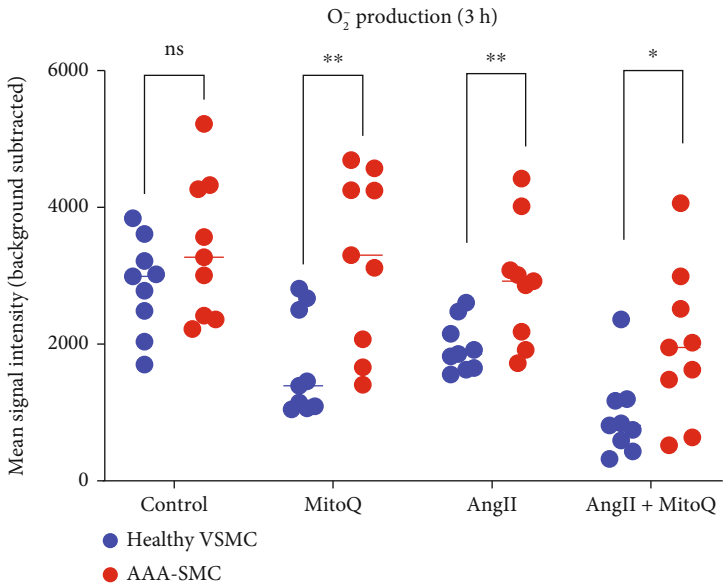

(a)

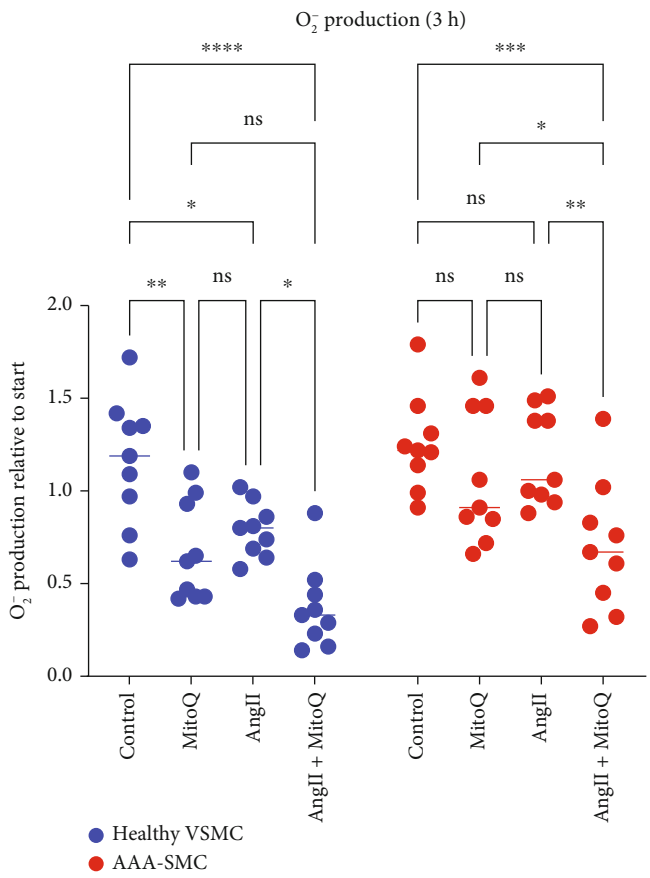

(b)

Figure 3: Continued.

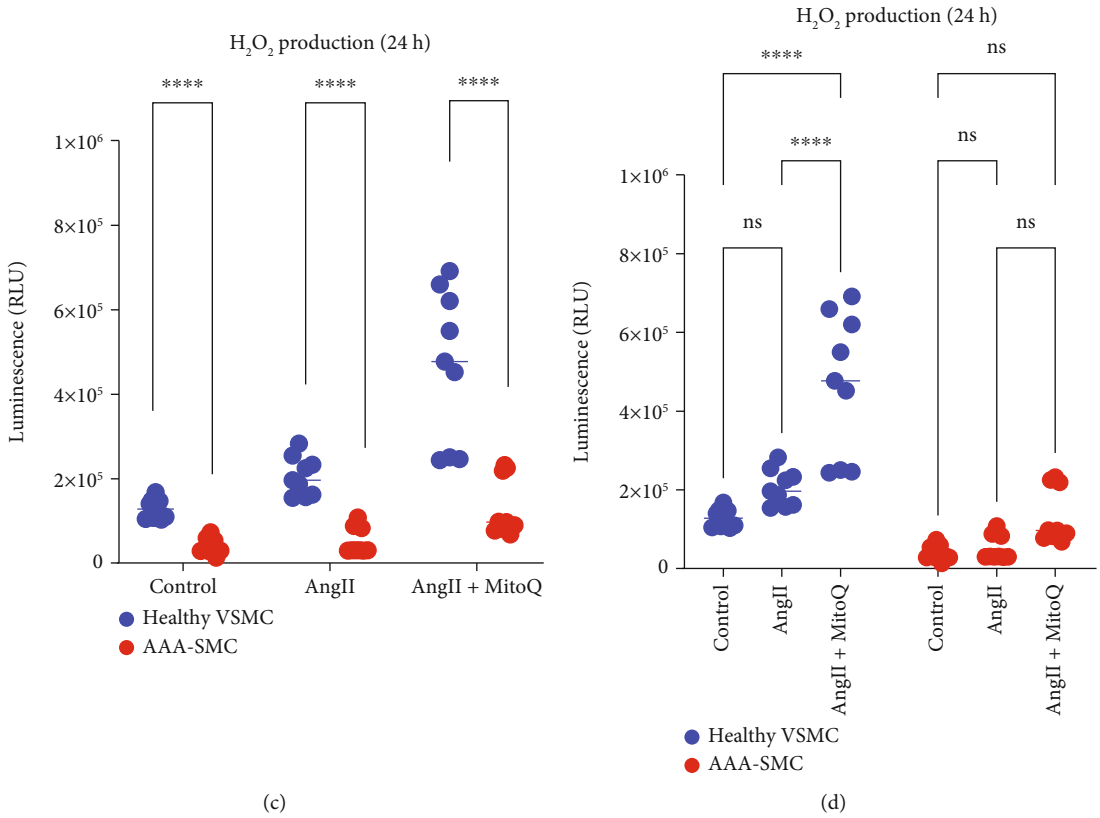

Figure 3: ROS production in healthy VSMC and AAA-SMC. (a, b) Analysis of O_2^- production in controls and after 3 h of treatment with 100 nM MitoQ, or 1 μM AngII, or a combination of both. Cells were stained with CellROX green reagent, and fluorescence was measured with a TECAN multiplate reader. Data are shown as mean signal intensity after background subtraction (a) or as absorbance relative to start (b) of three healthy and three AAA-SMC cultures analysed in triplicate. (c, d) Analysis of H_2O_2 amounts in controls and after 24 h of treatment with 1 μM AngII alone or in combination with 100 nM MitoQ. Detection of H_2O_2 was performed with a luminescent ROS-Glo H_2O_2 assay. Data are shown as relative light units (RLU) of three healthy and three AAA-SMC cultures analysed in triplicate and were analysed by multiple Mann–Whitney tests (a, c) or by 2-way ANOVA and Šidák's multiple comparison test as a post hoc test (b, d). ns: not significant; $^{*}p < 0,05$, $^{**}p < 0.01$, $^{***}p < 0.001$, and $^{****}p < 0.0001$.

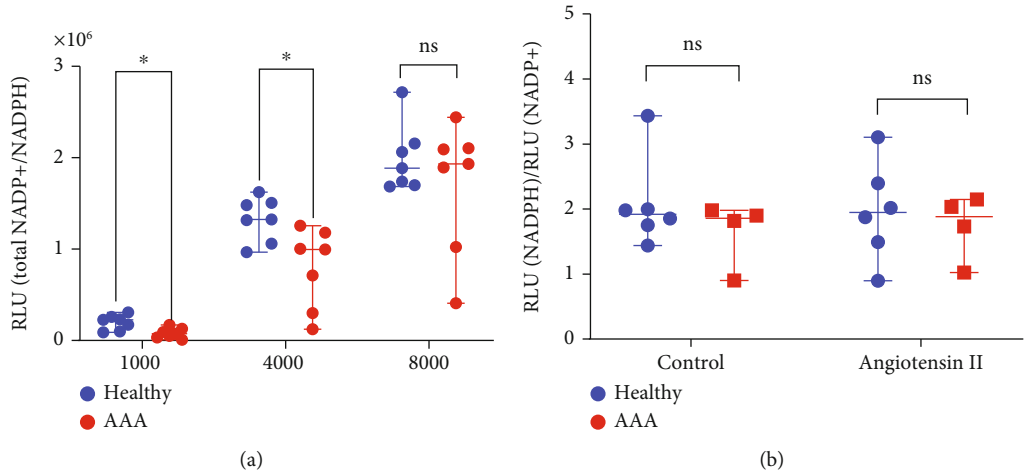

Figure 4: NADP+/NADPH metabolism. (a) Total NADP+/NADPH levels in untreated healthy VSMC ($n = 7$) and AAA-SMC ($n = 7$) cultures for varying cell densities. (b) NADPH to NADP+ ratio in healthy VSMC ($n = 6$) and AAA-SMC ($n = 4$) lines, left untreated or after treatment with 1 μM AngII for 24 hours. All measurements were performed in triplicate. Data are shown as median with range and were analysed pairwise with the Mann–Whitney U test, $^{*}p < 0,05$; ns: not significant.

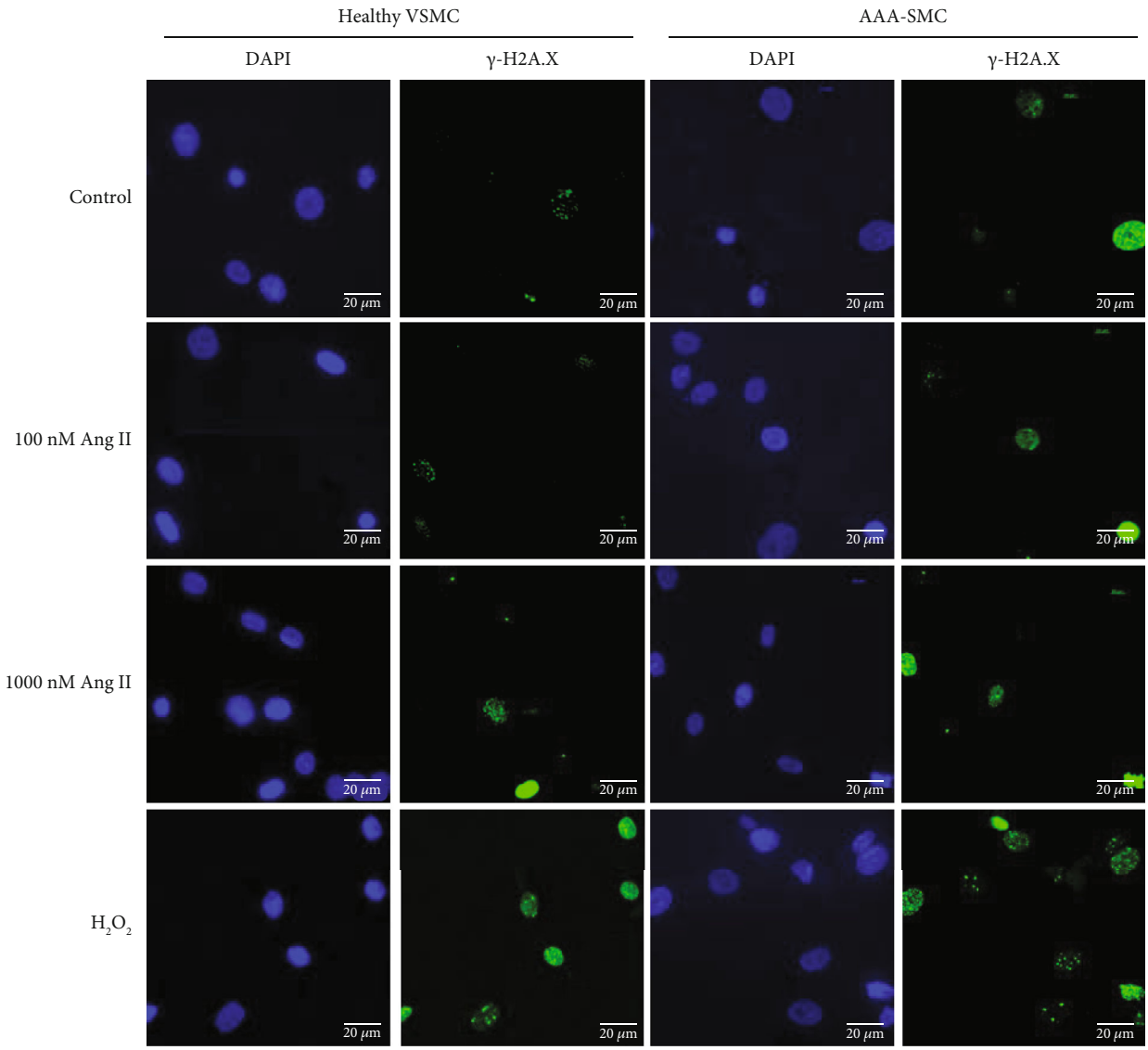

(a)

Figure 5: Continued.

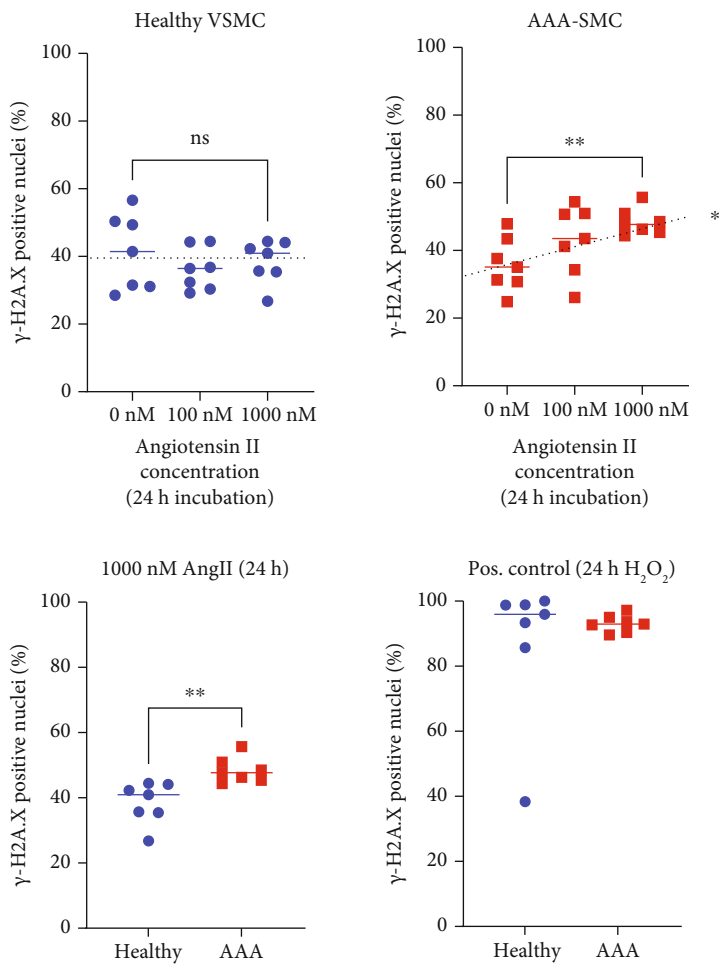

(b)

Figure 5: DNA damage in response to AngII in AAA-SMC ($n = 7$ cultures) versus healthy VSMC ($n = 7$ cultures). Cells were incubated with increasing concentrations of AngII for 24 h, respectively; fixed; and immunostained with an anti-γ-H2A.X antibody as described in Materials and Methods. 100 μM H_2O_2 was used as a positive control for maximal DNA damage after 24 h. (a) Representative images of healthy VSMC and AAA-SMC after treatment with AngII for 24 h. Scale bars = 20 μm. (b) Graphical representation of the image evaluation. Data points represent the mean percentage of γ-H2A.X-positive nuclei per total nuclei for each cell culture and are presented with median of $n = 7$ AAA-SMC cultures and $n = 7$ healthy VSMC cultures. Eight to fifteen images of each culture were evaluated for analysis. Statistical analysis was performed pairwise with the Mann–Whitney U test, $^{**}p < 0.01$. Ordinary one-way ANOVA was performed to test for a linear trend. $^{**}p < 0.01$; ns: not significant.

overproduction of these ROS can trigger pathophysiological reactions and thus impair vascular function [35]. This is because, despite antioxidant repair mechanisms, excessive amounts of ROS can eventually no longer be compensated and generate oxidative stress. Over many years, mitochondria can counteract this stress by regenerating permanently. A cycle of biogenesis, fusion, and fission guarantees the preservation of function and the disposal of damaged mitochondria by mitophagy [36]. However, with increasing age, dysfunctional mitochondria accumulate and thus also increase oxidative stress [37].

Here, we used *in vitro* cultures of AAA-derived and age-matched healthy VSMC to decipher the impact of mitochondrial oxidative stress in connection with AAA. We observed that mitochondrial damage in AAA-SMC was permanent and the resulting oxidative stress could not be compensated for as well as in healthy VSMC. Indeed, AAA-SMC contained less mitochondrial bodies, which were smaller and rounder than those in healthy VSMC. In addition, mitochondrial fission was significantly increased. Our findings are in line with previous reports. Increased fission of mitochondria has been described as a therapeutic target of AAA in humans and rodent abdominal aortic VSMC [38]. The authors speculated that the underlying mechanism involves upregulation of Drp1-mediated mitochondrial fission which results in a proinflammatory phenotype. In addition, exposure to AngII, one of the main inducers of AAA in mouse models, has been shown to induce mitochondrial fission in cultured rat aortic VSMC [39]. In general, mitochondrial fission creates smaller, more discrete mitochondria, which are more capable of generating ROS, and a higher fission-to-fusion rate has been associated with many diseases

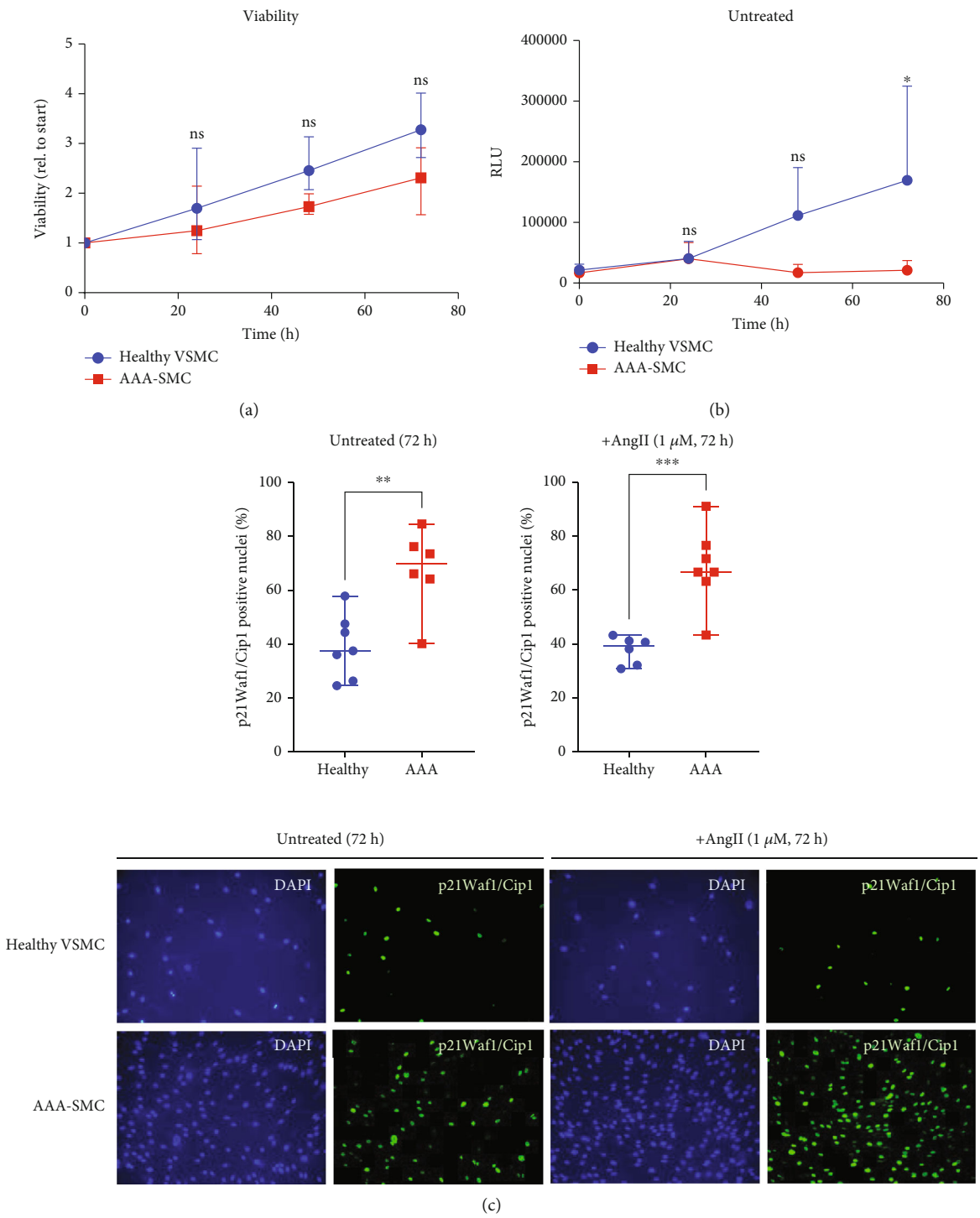

Figure 6: AAA-SMCs are subject to earlier growth arrest than healthy VSMCs. Cells were grown with serum withdrawal overnight before full medium was added with or without different concentrations of AngII. (a) Viability at different time points of untreated healthy VSMC and AAA-SMC as determined by WST-1 proliferation assay. Data show the means and ranges of $n = 3$ healthy VSMC and $n = 3$ AAA-SMC cultures analysed in triplicate. ns: not significant. (b) Apoptosis at different time points of untreated healthy VSMC and AAA-SMC as determined by Caspase-Glo 3/7 Assay. Data show the means and ranges of $n = 3$ healthy VSMC and $n = 3$ AAA-SMC cultures that were analysed in triplicate. Data were statistically analysed with 2-way ANOVA and Šídák's multiple comparison test as a post hoc test using the GraphPad Prism software. $^{*}p < 0.05$; ns: not significant. (c) Upper panel: percentage of p21Waf1/Cip1-positive nuclei in untreated and AngII-treated cell cultures. Data represent the median and range of $n = 3$ healthy VSMC and $n = 4$ AAA-SMC cultures, of which two or three images were taken for analysis. Data were statistically analysed with unpaired t-tests using the GraphPad Prism software. $^{*}p < 0.05$, $^{**}p < 0.01$, and $^{***}p < 0.001$. (c) Lower panel: representative images of samples grown for 72 hours without or with (1 μM) AngII and fluorescently labelled with p21Waf1/Cip1.

including cancer and cardiovascular diseases [40]. Under physiological conditions, fission is used to distribute mitochondria evenly among daughter cells during cell division. In addition, defective mitochondria can be separated and disposed of in this way before they cause damage or induce cell death [36]. Accordingly, our findings of increased fission in AAA-SMC may be interpreted as a response to the accumulation of damaged mitochondria that occurred during the course of aortic degeneration.

The higher number of mtDNA copies in AAA-SMC detected here was unexpected. Filamentous, elongated mitochondria contain several (6-8) mtDNA copies per mitochondrial nucleoid, whereas small mitochondria contain little to no mtDNA [41]. Thus, the higher mtDNA copy number seems to be at odds with the smaller and rounder mitochondria that were detected in AAA-SMC. However, reduction of mitochondrial particles after fission also requires functional mitophagy. Moreover, mtDNA can be released from defective mitochondria and accumulate outside of mitochondria if not properly removed. Thus, the high mtDNA copy number in combination with an increased fission to fusion rate may indicate defects in mitophagy in AAA-SMC, as it has been suggested by others [42]. Clear evidence of defective mitophagy in VSMC and its underlying causes in the course of AAA disease is still pending.

Another important observation described in this paper is the role of AngII, which appears to exert different effects on healthy and aneurysm-derived cells, respectively. A clear dose-dependent response to AngII via the antioxidative stress element ARE was only observed in healthy VSMC but not in AAA-SMC. AngII has been repeatedly described as a significant stimulus for ROS production in the vasculature and a trigger of senescence in aortic VSMC [28, 43–45]. All of these reports have used healthy VSMC for their analyses. Our data are in line with these reports, demonstrating that ARE response increased with AngII in healthy VSMC cultures 3 h after AngII treatment. However, to our knowledge, this is the first report that presents evidence for an alteration in the antioxidative stress response via the ARE pathway in AAA-SMC. Activation of the ARE element in genes encoding detoxification enzymes by the transcription factor Nrf2 protects cells from oxidative stress-induced cell death. The Nrf2/ARE-pathway has been shown to be important for protection against H_2O_2-induced inflammation and oxidative stress in cardiomyocytes [46], and alterations in this cascade have been reported to be associated with neurodegenerative diseases [47]. Given the importance of ROS detoxification, it will be very interesting to investigate Nrf2 and other components of this pathway for their expression and function in vascular cells in connection with AAA. It is possible that VSMC respond differently to AngII depending on the activity of this signalling pathway. This might explain in part the heterogenous stress response observed in AAA-SMC and has important implications for future use of pharmaceutical therapeutics.

As a result of reduced ARE activation and thus expression of detoxification enzymes, an accumulation of ROS would be expected. Indeed, our data demonstrated increased O^{2-} levels in AAA-SMC. The fact that mitochondria-targeted MitoQ was able to reduce O^{2-} levels in both controls and AngII-challenged healthy VSMCs, but not in AAA-SMCs, suggests involvement of mitochondria in activation of the Nrf2/ARE cascade, as it was demonstrated in cardiomyocytes [46]. Interestingly, the level of another ROS, H_2O_2, was clearly higher in healthy VSMC cultures than in AAA-SMC after 24 h. Moreover, the amount of H_2O_2 was significantly increased in MitoQ-treated cells after 24 h, again with a stronger effect in healthy VSMC than in AAA-SMC. Overall, this indicates that H_2O_2 production follows mitochondrial O_2^- production and is reduced in AAA-SMC. Considering that mitochondrial antioxidant defence is largely performed by manganese superoxide dismutase (MnSOD), which converts O_2^- to H_2O_2 and was shown to play an important role in vascular function [48], our data suggest MnSOD as another target that might be affected in AAA-SMC. MnSOD is considered the chief ROS scavenging enzyme in the cell, and reduced expression and/or activity of MnSOD result in diminished antioxidant capacity of the cell, including alterations of metabolic function. The resulting excess of O_2^- radicals contributes to the production of other ROS that further damage mitochondria [49]. Interestingly, a recent study demonstrated that mitochondrial-targeted therapies require mitophagy to prevent oxidative stress induced by MnSOD inactivation in cardiomyocytes [50]. Together with the alterations found here in mitochondrial dynamics and the reduced response to the antioxidant MitoQ, this supports the hypothesis of MnSOD inactivation in AAA-SMC.

The capability to balance NADPH and NADP+ was unaffected in both healthy VSMC and AAA-SMC, suggesting that the activity of NADPH oxidase which has previously been demonstrated to increase ROS production in VSMC [29] is not implied in oxidative stress generation, here. In contrast, the lower total amount of NADPH/NADP+ argues for a reduced mitochondrial mass in AAA-SMC, which is in line with our observations on mitochondrial dynamics.

Finally, the DNA in AAA-SMC appears to be more vulnerable towards high doses of AngII than that in healthy VSMC. Considering the differences in ARE activity, described above, this might be a consequence of their lack of an effective antioxidative stress response. The precise mechanism of this inadequate antioxidative stress response however remains to be elucidated.

Overall, we identified several distinct targets that may be impaired in AAA-SMC, thereby contributing to the development and persistence of oxidative stress in AAA: mitochondrial fission, mitophagy, the Nrf2/ARE pathway, and MnSOD. It is also possible that different alterations in these targets are present in AAA-SMC from different individuals, all leading to the same outcome, namely, a cascade of oxidative stress, inflammation, and degradation of the vessel wall. Future investigation will elucidate the roles of these targets and help to identify subsets of AAA patients that might benefit from different target-specific therapeutics to slow down the growth and prevent rupture of AAA.

A limitation of our study may be the origin of the healthy VSMCs that were used for control. While the AAA-SMCs were taken from the abdominal region of the

aorta, the healthy VSMCs were exclusively from thoracic regions of the aorta, because healthy abdominal VSMCs are not commercially available. In fact, thoracic and abdominal VSMCs stem from different embryonic lineages and there is evidence for different vulnerability and different responses to stress factors between thoracic and abdominal VSMCs [51–53]. Therefore, we cannot exclude that some of the differences in mitochondrial function and oxidative stress responses observed here are determined by their embryonic origin instead of reflecting damage associated with AAA progression. However, preliminary experiments with VSMC isolated from thoracic aneurysms and dissection argue for a disease-specific stress response rather than an embryologically determined one. Using the same experiments for investigation as described here, our studies showed that VSMCs from thoracic aneurysm and dissection respond more like VSMC from abdominal aneurysms than like healthy thoracic VSMCs (data not shown). A more detailed investigation of these differences is planned for future studies.

5. Conclusions

Based on our investigations on multiple cell cultures derived from healthy aorta and aortic aneurysms, we conclude that AAA-SMCs are persistently damaged. Our data strongly support the hypothesis that mitochondrial metabolism-generated free radicals, particularly O_2^-, account for mitochondrial dysfunction in AAA-SMC resulting in DNA damage and earlier senescence than healthy VSMC of age-matched adults. In addition, our data indicate a greater heterogeneity within AAA-SMC samples than within healthy VSMC which reflects the different responses to stress factors induced during aneurysm growth. Finally and in line with the observed heterogeneity, our data question the role of AngII in ROS-induced mitochondrial damage of AAA-SMC. AngII may drive ROS production in VSMC at early stages but seems to have little impact on advanced AAA-SMC. We conclude from our data that mitochondria in AAA-SMC may represent a worthwhile target for therapeutic intervention, for example, with mitochondria-targeted antioxidants to slow the growth of abdominal aortic aneurysms. However, these therapies may only be effective in some subgroups of AAA patients because of heterogeneous cellular responses, necessitating further studies.

Data Availability

All the data supporting the conclusion were shown in the paper and in the supplementary files. Details of the primary data that support the findings of this study are available from the corresponding author upon reasonable request.

Conflicts of Interest

The authors declare that there is no conflict of interest regarding the publication of this paper.

Acknowledgments

We thank Anja Spieler for the excellent technical assistance, i.e., isolation and in vitro culture of the cell lines and performing some of the experiments. The study was supported by budget funds of the Klinik für Gefäßchirurgie und Endovaskuläre Chirurgie Heidelberg. For the publication fee, we acknowledge the financial support by Deutsche Forschungsgemeinschaft within the funding programme "Open Access Publikationskosten" as well as by Universität Heidelberg.

Supplementary Materials

Supplementary table S1: characteristics of VSMC cultures. Supplementary Figure S1: ARE activity (relative to control, 0 nM) after 3 h and 24 h AngII treatment. Supplementary Figure S2: ARE activity in individual healthy VSMC and AAA-SMC cultures after treatment for 3 and 24 h with 0 nM, 10 nM, 100 nM and 1000 nM AngII. Supplementary figure S3: ROS production in healthy VSMC and AAA-SMC. (a and b) Analysis of O_2^- production in controls and after 24 h of treatment with 100 nM MitoQ, or 1 μM AngII, or a combination of both. Supplementary figure S4: total NADPH/NADP+ levels in response to AngII. Supplementary figure S5: DNA damage in response to AngII in AAA-SMC ($n = 7$ cultures) versus healthy VSMC ($n = 8$ cultures). Supplementary figure S6: viability of individual healthy VSMC cultures in response to AngII. Supplementary figure S7: viability of individual AAA-SMC cultures in response to AngII. *(Supplementary Materials)*

References

[1] P. Lacolley, V. Regnault, A. Nicoletti, Z. Li, and J. B. Michel, "The vascular smooth muscle cell in arterial pathology: a cell that can take on multiple roles," *Cardiovascular Research*, vol. 95, no. 2, pp. 194–204, 2012.

[2] G. Qian, O. Adeyanju, A. Olajuyin, and X. Guo, "Abdominal aortic aneurysm formation with a focus on vascular smooth muscle cells," *Life*, vol. 12, no. 2, p. 191, 2022.

[3] Z. Li and W. Kong, "Cellular signaling in abdominal aortic aneurysm," *Cellular Signalling*, vol. 70, article 109575, 2020.

[4] F. M. Davis, A. Daugherty, and H. S. Lu, "Updates of recent aortic aneurysm research," *Arteriosclerosis, Thrombosis, and Vascular Biology*, vol. 39, no. 3, pp. e83–e90, 2019.

[5] A. S. Peters, M. Hakimi, P. Erhart et al., "Current treatment strategies for ruptured abdominal aortic aneurysm," *Langenbeck's Archives of Surgery*, vol. 401, no. 3, pp. 289–298, 2016.

[6] F. L. Moll, J. T. Powell, G. Fraedrich et al., "Management of abdominal aortic aneurysms clinical practice guidelines of the European Society for Vascular Surgery," *European Journal of Vascular and Endovascular Surgery*, vol. 41, Suppl 1, pp. S1–S58, 2011.

[7] J. Golledge, J. V. Moxon, T. P. Singh, M. J. Bown, K. Mani, and A. Wanhainen, "Lack of an effective drug therapy for abdominal aortic aneurysm," *Journal of Internal Medicine*, vol. 288, no. 1, pp. 6–22, 2020.

[8] M. Navas-Madronal, C. Rodriguez, M. Kassan et al., "Enhanced endoplasmic reticulum and mitochondrial stress

in abdominal aortic aneurysm," *Clinical Science*, vol. 133, no. 13, pp. 1421–1438, 2019.

[9] T. I. Emeto, J. V. Moxon, M. Au, and J. Golledge, "Oxidative stress and abdominal aortic aneurysm: potential treatment targets," *Clinical Science (London, England)*, vol. 130, no. 5, pp. 301–315, 2016.

[10] G. Cafueri, F. Parodi, A. Pistorio et al., "Endothelial and smooth muscle cells from abdominal aortic aneurysm have increased oxidative stress and telomere attrition," *PLoS One*, vol. 7, no. 4, article e35312, 2012.

[11] M. L. Lucas, C. C. Carraro, A. Bello-Klein et al., "Oxidative stress in aortas of patients with advanced occlusive and aneurysmal diseases," *Annals of Vascular Surgery*, vol. 52, pp. 216–224, 2018.

[12] I. Wiernicki, M. Parafiniuk, A. Kolasa-Wolosiuk et al., "Relationship between aortic wall oxidative stress/proteolytic enzyme expression and intraluminal thrombus thickness indicates a novel pathomechanism in the progression of human abdominal aortic aneurysm," *The FASEB Journal*, vol. 33, no. 1, pp. 885–895, 2019.

[13] F. Usui, K. Shirasuna, H. Kimura et al., "Inflammasome activation by mitochondrial oxidative stress in macrophages leads to the development of angiotensin II-induced aortic aneurysm," *Arteriosclerosis, Thrombosis, and Vascular Biology*, vol. 35, no. 1, pp. 127–136, 2015.

[14] M. A. Kluge, J. L. Fetterman, and J. A. Vita, "Mitochondria and endothelial function," *Circulation Research*, vol. 112, no. 8, pp. 1171–1188, 2013.

[15] C. H. Byon, J. M. Heath, and Y. Chen, "Redox signaling in cardiovascular pathophysiology: a focus on hydrogen peroxide and vascular smooth muscle cells," *Redox Biology*, vol. 9, pp. 244–253, 2016.

[16] M. Wortmann, M. Arshad, A. S. Peters, M. Hakimi, D. Bockler, and S. Dihlmann, "The C57Bl/6J mouse strain is more susceptible to angiotensin II-induced aortic aneurysm formation than C57Bl/6N," *Atherosclerosis*, vol. 318, pp. 8–13, 2021.

[17] M. J. Rossman, R. A. Gioscia-Ryan, Z. S. Clayton, M. P. Murphy, and D. R. Seals, "Targeting mitochondrial fitness as a strategy for healthy vascular aging," *Clinical Science*, vol. 134, no. 12, pp. 1491–1519, 2020.

[18] A. W. Caliri, S. Tommasi, and A. Besaratinia, "Relationships among smoking, oxidative stress, inflammation, macromolecular damage, and cancer," *Mutation Research, Reviews in Mutation Research*, vol. 787, article 108365, 2021.

[19] M. Miyao, S. Cicalese, T. Kawai et al., "Involvement of senescence and mitochondrial fission in endothelial cell proinflammatory phenotype induced by angiotensin II," *International Journal of Molecular Sciences*, vol. 21, no. 9, p. 3112, 2020.

[20] M. Wortmann, E. Skorubskaya, A. S. Peters, M. Hakimi, D. Bockler, and S. Dihlmann, "Necrotic cell debris induces a NF-κB-driven inflammasome response in vascular smooth muscle cells derived from abdominal aortic aneurysms (AAA-SMC)," *Biochemical and Biophysical Research Communications*, vol. 511, no. 2, pp. 343–349, 2019.

[21] R. K. Dagda, S. J. Cherra, S. M. Kulich, A. Tandon, D. Park, and C. T. Chu, "Loss of PINK1 function promotes mitophagy through effects on oxidative stress and mitochondrial fission," *The Journal of Biological Chemistry*, vol. 284, no. 20, pp. 13843–13855, 2009.

[22] J. H. Bae, S. I. Jo, S. J. Kim et al., "Circulating cell-free mtDNA contributes to AIM2 inflammasome-mediated chronic inflammation in patients with type 2 diabetes," *Cell*, vol. 8, no. 4, 2019.

[23] J. C. Chang, S. J. Kou, W. T. Lin, and C. S. Liu, "Regulatory role of mitochondria in oxidative stress and atherosclerosis," *World Journal of Cardiology*, vol. 2, no. 6, pp. 150–159, 2010.

[24] A. J. Kowaltowski, N. C. de Souza-Pinto, R. F. Castilho, and A. E. Vercesi, "Mitochondria and reactive oxygen species," *Free Radical Biology & Medicine*, vol. 47, no. 4, pp. 333–343, 2009.

[25] T. H. Rushmore, M. R. Morton, and C. B. Pickett, "The antioxidant responsive element. Activation by oxidative stress and identification of the DNA consensus sequence required for functional activity," *The Journal of Biological Chemistry*, vol. 266, no. 18, pp. 11632–11639, 1991.

[26] J. M. Lee, J. Li, D. A. Johnson et al., "Nrf2, a multi-organ protector?," *The FASEB Journal*, vol. 19, no. 9, pp. 1061–1066, 2005.

[27] B. Briard, D. E. Place, and T. D. Kanneganti, "DNA sensing in the innate immune response," *Physiology (Bethesda)*, vol. 35, no. 2, pp. 112–124, 2020.

[28] I. C. Tsai, Z. C. Pan, H. P. Cheng, C. H. Liu, B. T. Lin, and M. J. Jiang, "Reactive oxygen species derived from NADPH oxidase 1 and mitochondria mediate angiotensin II-induced smooth muscle cell senescence," *Journal of Molecular and Cellular Cardiology*, vol. 98, pp. 18–27, 2016.

[29] M. L. McCormick, D. Gavrila, and N. L. Weintraub, "Role of oxidative stress in the pathogenesis of abdominal aortic aneurysms," *Arteriosclerosis, Thrombosis, and Vascular Biology*, vol. 27, no. 3, pp. 461–469, 2007.

[30] F. J. Miller Jr., W. J. Sharp, X. Fang, L. W. Oberley, T. D. Oberley, and N. L. Weintraub, "Oxidative stress in human abdominal aortic aneurysms," *Arteriosclerosis, Thrombosis, and Vascular Biology*, vol. 22, no. 4, pp. 560–565, 2002.

[31] W. Ying, "NAD+/NADH and NADP+/NADPH in cellular functions and cell death: regulation and biological consequences," *Antioxidants & Redox Signaling*, vol. 10, no. 2, pp. 179–206, 2008.

[32] W. Xiao, R. S. Wang, D. E. Handy, and J. Loscalzo, "NAD(H) and NADP(H) redox couples and cellular energy metabolism," *Antioxidants & Redox Signaling*, vol. 28, no. 3, pp. 251–272, 2018.

[33] A. Barzilai and K. I. Yamamoto, "DNA damage responses to oxidative stress," *DNA Repair*, vol. 3, no. 8-9, pp. 1109–1115, 2004.

[34] J. Yuan, R. Adamski, and J. Chen, "Focus on histone variant H2AX: to be or not to be," *FEBS Letters*, vol. 584, no. 17, pp. 3717–3724, 2010.

[35] Y. Mikhed, A. Daiber, and S. Steven, "Mitochondrial oxidative stress, mitochondrial DNA damage and their role in age-related vascular dysfunction," *International Journal of Molecular Sciences*, vol. 16, no. 7, pp. 15918–15953, 2015.

[36] C. Vasquez-Trincado, I. Garcia-Carvajal, C. Pennanen et al., "Mitochondrial dynamics, mitophagy and cardiovascular disease," *The Journal of Physiology*, vol. 594, no. 3, pp. 509–525, 2016.

[37] R. S. Balaban, S. Nemoto, and T. Finkel, "Mitochondria, oxidants, and aging," *Cell*, vol. 120, no. 4, pp. 483–495, 2005.

[38] H. A. Cooper, S. Cicalese, K. J. Preston et al., "Targeting mitochondrial fission as a potential therapeutic for abdominal

aortic aneurysm," *Cardiovascular Research*, vol. 117, no. 3, pp. 971–982, 2021.

[39] S. Lim, S. Y. Lee, H. H. Seo et al., "Regulation of mitochondrial morphology by positive feedback interaction between PKCδ and Drp1 in vascular smooth muscle cell," *Journal of Cellular Biochemistry*, vol. 116, no. 4, pp. 648–660, 2015.

[40] S. L. Archer, "Mitochondrial dynamics — mitochondrial fission and fusion in human diseases," *The New England Journal of Medicine*, vol. 369, no. 23, pp. 2236–2251, 2013.

[41] F. Legros, F. Malka, P. Frachon, A. Lombes, and M. Rojo, "Organization and dynamics of human mitochondrial DNA," *Journal of Cell Science*, vol. 117, no. 13, pp. 2653–2662, 2004.

[42] M. Ouyang, M. Wang, and B. Yu, "Aberrant mitochondrial dynamics: an emerging pathogenic driver of abdominal aortic aneurysm," *Cardiovascular Therapeutics*, vol. 2021, Article ID 6615400, 9 pages, 2021.

[43] K. E. Herbert, Y. Mistry, R. Hastings, T. Poolman, L. Niklason, and B. Williams, "Angiotensin II-mediated oxidative DNA damage accelerates cellular senescence in cultured human vascular smooth muscle cells via telomere-dependent and independent pathways," *Circulation Research*, vol. 102, no. 2, pp. 201–208, 2008.

[44] S. Masi, M. Uliana, and A. Virdis, "Angiotensin II and vascular damage in hypertension: role of oxidative stress and sympathetic activation," *Vascular Pharmacology*, vol. 115, pp. 13–17, 2019.

[45] L. J. Min, M. Mogi, M. Iwai, and M. Horiuchi, "Signaling mechanisms of angiotensin II in regulating vascular senescence," *Ageing Research Reviews*, vol. 8, no. 2, pp. 113–121, 2009.

[46] C. Shen, J. Wang, M. Feng et al., "The mitochondrial-derived peptide MOTS-c attenuates oxidative stress injury and the inflammatory response of H9c2 cells through the Nrf2/ARE and NF-kappaB pathways," *Cardiovasc Engineering and Technology*, vol. 13, 2022.

[47] A. Sarlette, K. Krampfl, C. Grothe, N. Neuhoff, R. Dengler, and S. Petri, "Nuclear erythroid 2-related factor 2-antioxidative response element signaling pathway in motor cortex and spinal cord in amyotrophic lateral sclerosis," *Journal of Neuropathology and Experimental Neurology*, vol. 67, no. 11, pp. 1055–1062, 2008.

[48] T. Fukai and M. Ushio-Fukai, "Superoxide dismutases: role in redox signaling, vascular function, and diseases," *Antioxidants & Redox Signaling*, vol. 15, no. 6, pp. 1583–1606, 2011.

[49] A. K. Holley, V. Bakthavatchalu, J. M. Velez-Roman, and D. K. St Clair, "Manganese superoxide dismutase: guardian of the powerhouse," *International Journal of Molecular Sciences*, vol. 12, no. 10, pp. 7114–7162, 2011.

[50] V. Peugnet, M. Chwastyniak, P. Mulder et al., "Mitochondrial-targeted therapies require mitophagy to prevent oxidative stress induced by SOD2 inactivation in hypertrophied cardiomyocytes," *Antioxidants*, vol. 11, p. 723, 2022.

[51] M. Leroux-Berger, I. Queguiner, T. T. Maciel, A. Ho, F. Relaix, and H. Kempf, "Pathologic calcification of adult vascular smooth muscle cells differs on their crest or mesodermal embryonic origin," *Journal of Bone and Mineral Research*, vol. 26, no. 7, pp. 1543–1553, 2011.

[52] J. M. Ruddy, J. A. Jones, and J. S. Ikonomidis, "Pathophysiology of thoracic aortic aneurysm (TAA): is it not one uniform aorta? Role of embryologic origin," *Progress in Cardiovascular Diseases*, vol. 56, no. 1, pp. 68–73, 2013.

[53] S. L. Thieszen, M. Dalton, P. F. Gadson, E. Patterson, and T. H. Rosenquist, "Embryonic lineage of vascular smooth muscle cells determines responses to collagen matrices and integrin receptor expression," *Experimental Cell Research*, vol. 227, no. 1, pp. 135–145, 1996.

Hindawi
Oxidative Medicine and Cellular Longevity
Volume 2022, Article ID 2062885, 14 pages
https://doi.org/10.1155/2022/2062885

Research Article

CircCRIM1 Ameliorates Endothelial Cell Angiogenesis in Aging through the miR-455-3p/Twist1/VEGFR2 Signaling Axis

Lei Zhao,[1,2,3] **Rencong Chen**,[1,2,3] **Jiacong Qiu**,[4] **Yingxiong Huang**,[5] **Chong Lian**,[6] **Xiaonan Zhu**,[7] **Jin Cui**,[1,2,3] **Siwen Wang**,[1,2,3] **Shenming Wang**,[1,2,3] **Zuojun Hu**,[1,2,3] **and Jinsong Wang**[8]

[1]*Department of Vascular Surgery, The First Affiliated Hospital of Sun Yat-sen University, NO. 58, Zhong Shan Er Lu, Guangzhou 510080, China*
[2]*National-Guangdong Joint Engineering Laboratory for Diagnosis and Treatment of Vascular Diseases, NO. 58, Zhong Shan Er Lu, Guangzhou 510080, China*
[3]*Guangdong Engineering and Technology Center for Diagnosis and Treatment of Vascular Diseases, NO. 58, Zhong Shan Er Lu, Guangzhou 510080, China*
[4]*Department of vascular Surgery, The Second Affiliated Hospital of Nanchang University, Nanchang University, Nanchang, Jiangxi 330006, China*
[5]*Department of Emergency, The First Affiliated Hospital of Sun Yat-sen University, NO. 58, Zhong Shan Er Lu, Guangzhou 510080, China*
[6]*Department of Endovascular Surgery, The First Affiliated Hospital of Zhengzhou University, 450000 Zhengzhou, Henan, China*
[7]*Department of Pharmacology Laboratory, Zhongshan School of Medicine, Sun Yat-sen University, NO. 58, Zhong Shan Er Lu, Guangzhou 510080, China*
[8]*Division of Vascular and Plastic Surgery, Guangdong Provincial People's Hospital, Guangdong Academy of Medical Sciences, Guangzhou 510080, China*

Correspondence should be addressed to Jinsong Wang; wangjinsong@gdph.org.cn

Received 29 June 2022; Accepted 22 September 2022; Published 8 October 2022; Published October 2022

Academic Editor: Yanshuo Han

Background. Aging leads to vascular endothelial cell senescence. Decreased expression of VEGFA and VEGFR2 plays a crucial role in impairing angiogenesis in senescent endothelial cells. Noncoding RNAs, including circular RNAs (circRNAs) and microRNAs (miRNAs), regulate endothelial cell proliferation, differentiation, apoptosis, and migration and participate in the occurrence and development of vascular diseases. However, the mechanism of noncoding RNAs in age-related vascular endothelial dysfunction remains unclear. Here, we aimed to identify the circRNA that is associated with VEGF/VEGFR2 signaling pathway activation in angiogenesis. *Methods*. Immunoblotting, quantitative reverse transcription-polymerase chain reaction (qRT–PCR), *in vitro* and *in vivo* experiments, luciferase assays, and chromatin immunoprecipitation followed by qRT–PCR (ChIP–qPCR) assays were performed to clarify the roles played by circCRIM1 in mouse aortic endothelial cell (MAEC) angiogenesis. *Results*. CircCRIM1 expression was downregulated in both an aging mouse model of lower limb ischemia *in vivo* and aging MAECs *in vitro*. Overexpressing circCRIM1 mediated through a plasmid or adeno-associated virus (AAV) reversed the downregulation of angiogenesis-related phenotype acquisition during aging. MiR-455-3p was confirmed to be a potential target of circCRIM1 through luciferase assays followed by RNA fluorescence in situ hybridization (FISH), which revealed the colocalization of circCRIM1 and miR-455-3p. CircCRIM1 was found to be a competitive endogenous RNA that sponged miR-455-3p and regulated angiogenesis-related phenotypes in MAECs. Furthermore, Twist1 was found to be downstream of miR-455-3p. A ChIP–qPCR assay showed that Twist1 promoted VEGFR2 expression by binding to the promoter region, playing a vital role in angiogenesis. *Conclusions*. Decreased expression of circCRIM1 impaired angiogenesis in aging via the miR-455-3p/Twist1/VEGFR2 axis. Our findings suggest that overexpression of circCRIM1 may be an effective therapeutic strategy for promoting ischemic lower limb blood flow recovery.

1. Introduction

Peripheral artery disease (PAD) is a severe medical challenge that significantly impacts people's lives and health in aging societies worldwide. In China, 6.6% of adults more than 35 years old (approximately 45.3 million people) have PAD, and the prevalence of PAD among people 60 years old and older ranges from 2.8% to 15.3% [1]. Age is an independent factor affecting vascular homeostasis, leading to impaired angiogenesis [2]. Endothelial cells (ECs), which bridge blood and vascular tissue to deliver nutrients and active molecules, play important roles in maintaining vascular homeostasis, including in vascular growth and differentiation, as well as vascular tone regulation [3]. Therefore, elucidation of the biological role and molecular mechanism of ECs in aging for early PAD detection and therapeutic target development is of high clinical significance.

Recently, noncoding RNAs that play key roles in regulating gene expression have attracted considerable attention. As a type of noncoding RNA, circular RNAs (circRNAs) tend to form a ring structure by covalent bonding in the absence of a 5′-end cap and a 3′-end poly (A) tail [4]. Benefiting from their stability, conservation, endogenous nature, and abundance, circRNAs have been associated with an increasing number of functions in epigenetic regulation in various organisms [5]. Studies have shown that circRNAs are of considerable importance to regulate epigenetic modifications that affect vascular EC function, including proliferation, differentiation, migration, and tube formation, thus mediating the occurrence and development of various vascular diseases [6, 7]. However, the effects of circRNAs on vascular EC angiogenesis in aging and the related mechanism remain unclear. Consequently, there is an urgent need for research on differentially expressed circRNAs in young and old ECs to explore the mechanisms of age-related angiogenesis, especially to provide new insights into early diagnostic markers and therapeutic targets for PAD.

In our study, we found that the circular RNA mmu_circ_0007020, a putative circRNA originating from the cysteine-rich transmembrane BMP regulator 1 (chordin like) (CRIM1) mRNA, was significantly downregulated in vascular endothelial cells in elderly mice by performing a whole-transcriptome sequencing data screening. To explore the underlying functional role played by mmu_circ_0007020 (circCRIM1) in ECs, *in vitro* and *in vivo* experiments were performed and showed that circCRIM1 sponged miR-455-3p and thus enhanced endothelial angiogenesis in aging, targeting Twist1/VEGFR2 signaling axis.

2. Materials and Methods

2.1. Clinical Samples and Ethical Statements. This study has been approved by the ethics committee of the First Affiliated Hospital of Sun Yat-sen University (Approval No. [2022]337) and is in accordance with the Helsinki Declaration. The arterial tissues were derived from patients over 65 years old that were performed abdominal aortic aneurysmectomy with artery reconstruction, or patients less than 30 years who volunteer to donate their bodies with informed consent. Samples were sectioned from the distal iliac arterial tissues adjacent to the lesions in old patients, or the normal iliac arteries in young patients.

2.2. Cell Culture. MAECs were isolated from C57BL/6 mice and were cultured as described in our previous study [8]. Briefly, aortas were dissected from euthanized mice and were digested by trypsin. The harvested MAECs were cultured in DMEM (Thermo Fisher Scientific) medium containing 10% fetal bovine serum (FBS, Thermo Fisher Scientific), and 1% penicillin/streptomycin in an incubator at 37°C with 5% CO_2. The old mice were 18 months old, and the young mice were 4 weeks old [9]. MAECs were extracted from the same sample batch obtained from 4 mice, and the experiments were performed at passages 3 to 5. The mouse studies and experimental procedures were approved by the Ethics Committee for Experimental Animals of the First Affiliated Hospital of Sun Yat-sen University (Approval No. [2021]581).

2.3. Cell Transfection. CircCRIM1 short interfering RNA (siRNA, RiboBio) and plasmid (Geneseed) were incubated with Lipofectamine 3000 (Thermo Fisher Scientific) in a reduced serum medium and then used for cell transfection with the concentration of 50 nmol and 2.5 μg/mL, respectively. Transfected cells were cultured at 37°C in an incubator with 5% CO_2. RNA and total protein were extracted from 48 to 72 h after transfection. Transfected cells were performed in subsequent experiments after 48 h transfection. All siRNA sequences used for transfection are listed in Supplementary Material Table I.

2.4. RNA Extraction and qRT–PCR. TRIzol reagent (Thermo Fisher Scientific) was used to extract total RNA from MAECs in the old group and young group. And then the RNAs were performed on reverse transcription into cDNA using a first-strand cDNA synthesis kit (TaKaRa) after purity and spectrophotometric identification of concentration. SYBR green PCR Master Mix (TaKaRa) was used for subsequent qRT–PCR detected in a LightCycler 480 system (Roche). GAPDH expression was compared with circCRIM1 and Twist1 expression levels as the internal reference gene, and U6 expression was compared with microRNA (miRNA) expression as the internal reference gene. All primer sequences are listed in Supplementary Material Table II.

2.5. RNase R Experiment. RNAs from MAECs (10 μg) were incubated with ribonuclease R (RNase R, 3 U/μg, Geneseed) at 37°C for 20 min. Then the treated RNAs were reversely transcribed using different primers and then detected by qRT–PCR.

2.6. RNA Immunoprecipitation. RNA immunoprecipitation kit (Geneseed) was used for RNA immunoprecipitation (RIP) analysis. First, MAECs were transfected by a plasmid or vector, respectively. And then RNAs extracted from each group were incubated with magnetic beads bound to anti-Argonaute 2 (AGO2) or anti-IgG antibody (Millipore) at 4°C for 6 h. Then the magnetic beads were cleaned and purified with columns to eliminate the DNAs and RNAs. Finally, proteins were isolated by acetone and ethyl alcohol and subsequently determined by western blotting.

2.7. ChIP–qPCR. SimpleChIP® Enzymatic Chromatin IP Kit (Agarose Beads) (Cell Signaling Technology, Inc.) was used for the ChIP experiment. Proteins and nucleic acids in MAECs were cross-linked by treatment with a 1% formaldehyde solution. Then, MAECs were incubated with the protease inhibitor cocktail at 4°C and were collected for subsequent experiments. The cross-linked chromatin was extracted from MAECs by lysis buffer, followed by purification procedures and sonication. After being treated with RNase A and Proteinase K as required, the qualified chromatin sample was incubated at 4°C overnight with 1 × ChIP buffer supplemented with Twist1 antibody (Santa Cruz Biotechnology, Inc.). On the next day, the Protein G Agarose Beads were used for further immunoprecipitation and purification. Finally, the pellets were eluted and reverse cross-linked to release ChIP DNA, and then the DNAs were prepared and used for subsequent qRT–PCR. All protocol details were available in the manual. The primers for VEGFR2 used in ChIP–qPCR are listed in Supplementary Material Table III.

2.8. Nucleic Acid Electrophoresis. qRT–PCR products of cDNA and gDNA were performed on electrophoresis at 100 V for 45 minutes in 3% agarose gel supplemented with TAE buffer. Nucleic acid fragments of 100-500 bp were identified by using a DNA marker (Accurate Biology). Then the gel was irradiated and imaged by an ultraviolet (UV) ray detector.

2.9. Fluorescence In Situ Hybridization (FISH). Cy3-labeled circCRIM1 probe and FITC-labeled miR-455-3p probe were synthesized by GenePharma (Shanghai, China). FISH was carried out to determine the localization of circCRIM1 and miR-455-3p in MAECs. CircCRIM1 and miR-455-3p probes were hybridized and incubated overnight. The Zeiss LSM710 confocal laser scanning microscope (Zeiss Instruments) captured images, and the Otsu FLTER software automatically sets thresholds to quantify the immunofluorescence signals of circCRIM1 and miR-455-3p. The colocated signals (Pearson Manders' coefficients) were calculated based on representative cell images by the JACoP (i.e., co-location plug-in). The probe sequences of circCRIM1 and miR-455-3p refer to Supplementary Material Table IV.

2.10. Western Blotting. Frozen RIPA buffer (Thermo Fisher Scientific) containing protease and phosphatase inhibitors was used for lysis. After using a BCA Protein Analysis Kit (Thermo Fisher Scientific) to detect the concentration, and equivalent quantities (30 μg) of protein samples were loaded onto 10% gels for SDS-PAGE, followed by transference to PVDF membrane (Millipore). Then, the membrane was blocked with TBST containing 5% bovine serum albumin (BSA, BioFroxx), and rabbit primary antibody against Twist1 was applied to incubate at 4°C overnight, while GAPDH was used as control. And then, the secondary antibody was applied to membrane incubation for an hour at room temperature. NovexECL (Invitrogen) visualized the expression of proteins and the signal quantification was analyzed by ImageJ software (version 1.8.0).

2.11. Luciferase Assay. CircCRIM1 sequences with miR-455-3p binding site mutations were acquired with a QuikChange II Locus-Directed Mutation Kit (Stratagene). Wild-type-(Wt-) miR-455-3p and mutant (MUT)-miR-455-3p purchased from Geneseed were cotransfected with the negative control (NC) or circCRIM1 sequence into HEK-293 T cells by Lipofectamine 3000 (Thermo Fisher Scientific). After 24 h transfection, luciferase activities were detected using a dual-luciferase reporting and detection kit (TransGen Biotech).

2.12. In Vitro Wound Healing Assay. Treated MAECs were inoculated in a 6-well culture plate until the confluence of 90% was reached. The cell monolayer was scratched to create a reference point by a 1 ml sterile pipette tip, and then they were washed with sterile phosphate-buffered saline (PBS) buffer. Reference images before the experiment were recorded by a microscope (Olympus Co., Ltd.). After being cultured in the serum-free medium for one day, the cell images of the same area were obtained by microscopy again, and statistical analysis of the scratch healing area was performed with ImageJ software.

2.13. Transwell Assay. A chamber with an 8 μm aperture (Corning Life Sciences) was placed into a twenty-four-well plate with the lower chamber containing 400-600 μL of complete medium supplemented with 15% FBS, in which the upper chamber was inoculated with treated MAECs that were suspended by 300 μL of serum-free medium. After 24 h of culture, the cells were fixed with 4% paraformaldehyde for 20 min and were subsequently stained with crystal violet for 15 min. Finally, the nonmigrating cells were removed from the inner membrane by gently wiping the upper chamber wall with cotton balls, and the migrating cells in 5 random areas were counted through light microscopy (Olympus Co., Ltd.).

2.14. Tube Formation Experiment. Twenty-four-well plates were precooled overnight at 4°C, and each well was padded with 200 μL of matrix glue (Corning Life Sciences), placed in a cold closet for 10 min to level the matrix glue, followed by culture in a cell incubator for half an hour to enable matrix coagulation. MAECs with a density of 150 thousand/well were added into the solidified matrix gel and cultured for six hours. At last, a light microscope (Olympus Co., Ltd.) was used to take images. The tube length measurements were performed by the ImageJ software.

2.15. 5-Ethynyl-2′-Deoxyuridine (EdU) Cell Proliferation Assay. MAECs were cultured in nighty-six-well plates until 60-70% confluence was achieved. The proliferative capacity of MAECs was assessed according to the instructions of a C10310-1/-2/-3 kit (RiboBio), and cell proliferation capacity was assessed by measuring the proportion of EdU-positive cells with a fluorescence microscope (Leica).

2.16. Animal Model. All procedures were approved by the Animal Ethics Committee of the First Affiliated Hospital of Sun Yat-sen University (Approval No. [2021]581). C57BL/6 mice aged eighteen months or four weeks

(GemPharmatech Co., Ltd.) was used to establish an animal model of unilateral hindlimb ischemia. The mice were anesthetized with isoflurane and were conducted by a 1-cm incision in the right inguinal region. After subcutaneous tissue separation followed by the femoral artery sheath open, the femoral artery was separated from the concomitant vein and nerve. Then, the femoral arteries were ligated with 7-0 silk thread at both ends and subsequently cut off in between. Finally, the incision was sutured. The other side of the left hindlimb was used as the control. The mice were randomly divided into 4 groups, including old mice injected with adeno-associated virus serotype 9 (AAV9)-circCRIM1, old mice injected with AAV9-NC, old mice injected with PBS, and young mice injected with PBS. All AAVs were designed and obtained from GeneChem (Shanghai, China). To develop overexpression AAV, circCRIM1 was subcloned into a GV526 AAV9 vector (CAG-MCS-SV40 PolyA). AAV9 (30 μL in each leg for 10^{10} VG of virus volume) was injected and PBS (30 μL in each leg) was injected into the calf gastrocnemius muscle two weeks before the operation, and the left hindlimb on the other side as the control. Blood flow was observed with an animal blood flow imaging apparatus before and on days 0, 3, 7, 14, 21, and 28 after surgery. The mice were euthanatized via intraperitoneal injection of high-dose pentobarbital on day 28 after the operation, and the gastrocnemius muscles were analyzed by immunohistochemistry, qRT–PCR, and other experiments.

2.17. Blood Flow Measurements. An animal blood flow imaging apparatus, PeriCamPS I (Perimed), was used to measure lower limb blood flow in mice 0, 3, 7, 14, 21, and 28 days after surgery in an environment with suitable temperature and humidity, without excessive light or noise. PIMSoft (Perimed) software was used to analyze the blood flow recovery index by calculating the perfusion ratio of ischemic limbs to normal limbs.

2.18. Immunohistochemistry. Hydrogen peroxide blocker-treated mouse muscle sections (3 μm) were incubated with anti-CD31 and anti-Twist1 primary antibodies overnight. Then, the sections were washed and subsequently incubated with secondary antibodies, followed by 3, 3′-diaminobenzidine reagent (DAB; Solarbio) treatment and hematoxylin staining. Olympus BX51 microscope (Olympus) was used to take images of the muscle sections.

2.19. Statistical Analysis. All data are presented as the mean ± standard deviation (SD) and were analyzed by the GraphPad Prism 8.0.1. Comparisons between two groups were analyzed by independent sample T-test, and a one-way analysis of variance (ANOVA) was performed for comparisons between three or more groups. P value < 0.05 was considered statistically significant.

3. Results

3.1. CircCRIM1 characteristics. We found that circCRIM1 expression in ECs of elderly mice was downregulated compared with that of young mice based on our previous whole-transcriptome sequencing [8]. To determine the expression of circCRIM1 in aging, we investigated the expression of circCRIM1 in 5th generation old endothelial cells (OEC) and young endothelial cells (YEC) using qRT–PCR. The results showed that circCRIM1 expression was significantly lower in the OEC than in YEC (Figure 1(a)). Information on circCRIM1 from the circBase database showed that in mice circCRIM1 is derived from the CRIM1 gene on chromosome 17 (Figure 1(b)). The code in circBase is mmu_circ_0007020 and shows 1041 bases. Agarose gel electrophoresis revealed that divergent circCRIM1 primers were amplified by cDNA but not by gDNA (Figure 1(c)). CircCRIM1 was resistant to RNase R digestion, while CRIM1 mRNA and GAPDH were not amplified by cDNA (Figure 1(d)). To verify the subcellular localization of circCRIM1, an RNA FISH assay was implemented and showed that circCRIM1 was predominantly localized in the cytoplasm (Figure 1(e)).

3.2. CircCRIM1 Promotes MAECs' Proliferative, Migratory, and Tube Formative Capacities In Vitro. To clarify whether circCRIM1 plays a role in MAEC angiogenesis, we designed an overexpression vector of circCRIM1 (OE-circCRIM1) that was subsequently transfected into OEC. qRT–PCR showed that circCRIM1 in the OEC was successfully overexpressed (Figure 2(a)) and that the expression of CRIM1 mRNA was not altered (Figure 2(b)).

To silence endogenous circCRIM1 expression, we transfected circCRIM1 siRNA into YEC, and siRNA-NC was transfected into YEC to establish the control. qRT–PCR showed that siRNAs significantly knocked down the expression of circCRIM1 in YEC and that si-circCRIM1-2 showed the most obvious effect, and therefore, si-circCRIM1-2 was selected for use in subsequent experiments (Figure 2(c)). Notably, none of the siRNAs altered the expression of CRIM1 mRNA (Figure 2(d)).

A series of functional experiments were conducted to further examine the function of circCRIM1 in angiogenesis-related phenotype acquisition. After circCRIM1 expression was upregulated by transfecting OE-circCRIM1 into OEC, MAEC showed increased proliferation capacity, as evaluated by EdU assay (Figure 2(e)), while circCRIM1 siRNAs diminished MAEC proliferation among the YEC populations (Figure 2(f)). Furthermore, CircCRIM1 increased the OEC tube formation number (Figure 2(g)), and tube formation was impaired in the YEC transfected with circCRIM1 siRNA (Figure 2(h)). As shown in Figures 2(i) and 2(j), the Transwell assay results showed that upregulation of circCRIM1 expression ameliorated OEC migration, while silencing of circCRIM1 expression resulted in a low YEC migration rate. Similarly, *in vitro* wound healing assay results supported the finding suggesting that overexpressing circCRIM1 invigorated OEC migration (Figure 2(k)), and transfection of circCRIM1 siRNA took the edge off the migratory capacity of the YEC (Figure 2(l)).

3.3. MiR-455-3p is the Downstream Target of CircCRIM1. As circCRIM1 is abundantly expressed in the cytoplasm, we investigated how it regulates angiogenesis in MAECs. RIP

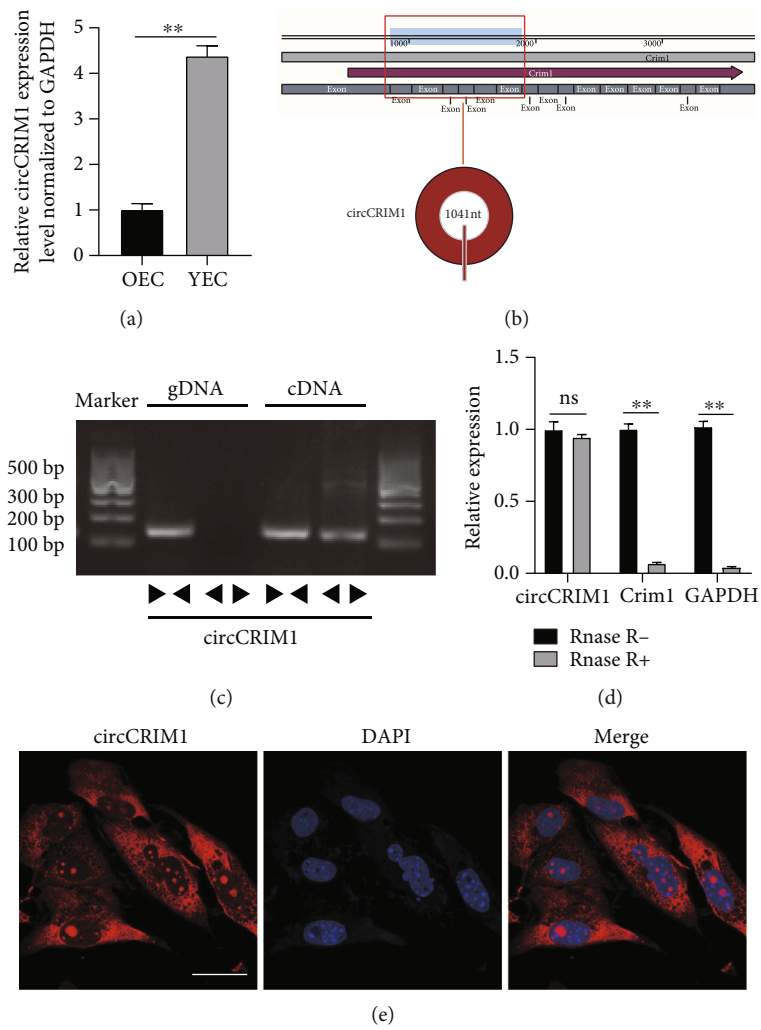

Figure 1: Profiling of circCRIM1. (a) Comparison of the circCRIM1 expression in OECs and YECs, normalized to GAPDH ($n = 3$). (b) Information of circCRIM1 from the circBase database. (c) Agarose gel electrophoresis results showed that divergent circCRIM1 primers were amplified by cDNA but not by gDNA. (d) With or without RNase R, comparison of the circCRIM1 and linear CRIM1 mRNA expression in MAECs. (e) FISH assay showed that circCRIM1 was predominantly localized in the cytoplasm. (Magnification, 400×, scale bar, 15 μm). (The data are expressed as the mean ± SD, $^{**}P < 0.01$ versus the negative control, ns means no significance).

experiments with OEC showed that circCRIM1 interacted with the AGO2 protein, which bound circRNA and miRNA to fulfill the competing endogenous RNA (ceRNA) function (Figure 3(a)). To identify the miRNAs that were potentially targeted by circCRIM1, we performed bioinformatics analysis using the miRanda database and RNAhybrid database. Among the potential miRNAs, we verified that only miR-455-3p was significantly overexpressed in the OEC compared with YEC (Figure 3(b)). Then, qRT–PCR was performed to verify that circCRIM1 overexpression resulted in the downregulation of miR-455-3p in the OEC (Figure 3(c)). In contrast, miR-455-3p was found to be upregulated after circCRIM1 knockdown in YECs (Figure 3(d)). The results of the FISH experiments showed the colocalization of circCRIM1 and miR-455-3p (Figure 3(e)). To further validate the potential binding sites of circCRIM1 and miR-455-3p, a luciferase assay was performed to prove that miR-455-3p suppressed the luciferase activity of the circCRIM1 3′-UTR-WT construct but not the circCRIM1 3′-UTR-MUT construct (Figure 3(f)). Our results indicated that the specific interaction between circCRIM1 and miR-455-3p exists.

3.4. MiR-455-3p Inhibits MAECs Proliferation and Migration. To further determine the functional role played by miR-455-3p in MAECs, we transfected an inhibitor of miR-455-3p into OEC to silence miR-455-3p and simultaneously overexpressed miR-455-3p in YEC through transfection of mimic. qRT–PCR was performed to prove the transfection efficacy (Figures 3(g) and 3(h)). As shown in Figures 3(i) and 3(j), proliferation was significantly increased by the miR-455-3p inhibitor transfected into OEC but impaired by transfection of the miR-455-3p mimic in YEC, as determined by the EdU assay. The

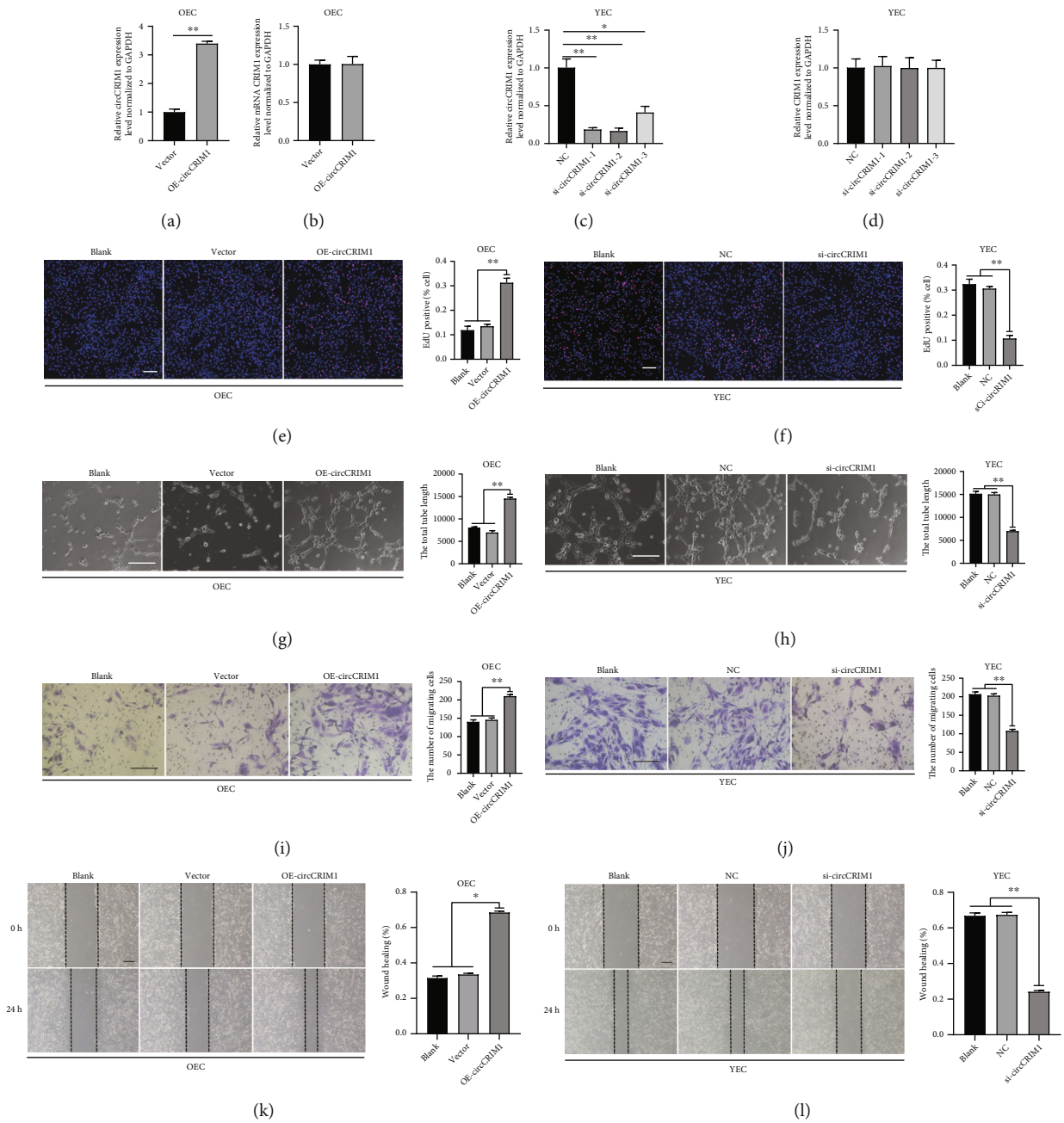

Figure 2: CircCRIM1 promotes MAECs' proliferative, migratory, and tube formative capacities *in vitro*. (a) CircCRIM1 expression was upregulated by transfecting OE-circCRIM1 into OEC ($n = 3$). (b) The CRIM1 mRNA expression was not altered significantly after circCRIM1 overexpression ($n = 3$). (c) CircCRIM1 expression was knockdown by transfecting circCRIM1 siRNAs into YEC ($n = 3$). (d) The CRIM1 mRNA expression was not altered significantly after transfection of circCRIM1 siRNAs ($n = 3$). (e) Overexpressing circCRIM1 increased OEC proliferation capacity in the EdU assay ($n = 3$, scale bar, 100 μm). (f) CircCRIM1 siRNAs diminished YEC proliferation in the EdU assay ($n = 3$, scale bar, 100 μm). (g) Overexpressing circCRIM1 promoted OEC tube formation ($n = 3$, scale bar, 100 μm). (h) CircCRIM1 siRNAs impaired YEC tube formation ($n = 3$, scale bar, 100 μm). (i) Overexpressing circCRIM1 ameliorated OEC migration in the Transwell assay ($n = 3$, scale bar, 100 μm). (j) CircCRIM1 siRNAs decreased YEC migration in the Transwell assay ($n = 3$, scale bar, 100 μm). (k) Overexpressing circCRIM1 invigorated OEC migration in the *in vitro* wound healing assay ($n = 3$, scale bar, 100 μm). (l) CircCRIM1 siRNAs diminished YEC migration in the *in vitro* wound healing assay ($n = 3$, scale bar, 100 μm). (The data are presented as the *mean* ± *SD*, $^{*}P < 0.05$, $^{**}P < 0.01$ versus the negative control).

in vitro wound healing assay showed an enhanced migratory capacity of the OEC because of miR-455-3p silencing (Figure 3(k)), while upregulation of miR-455-3p resulted in a weakened migratory capacity of YEC (Figure 3(l)).

3.5. CircCRIM1 Promotes Angiogenesis by Sponging MiR-455-3p in MAECs. Furthermore, we performed rescue experiments to determine whether circCRIM1 regulates angiogenesis by sponging miR-455-3p and to discern its function.

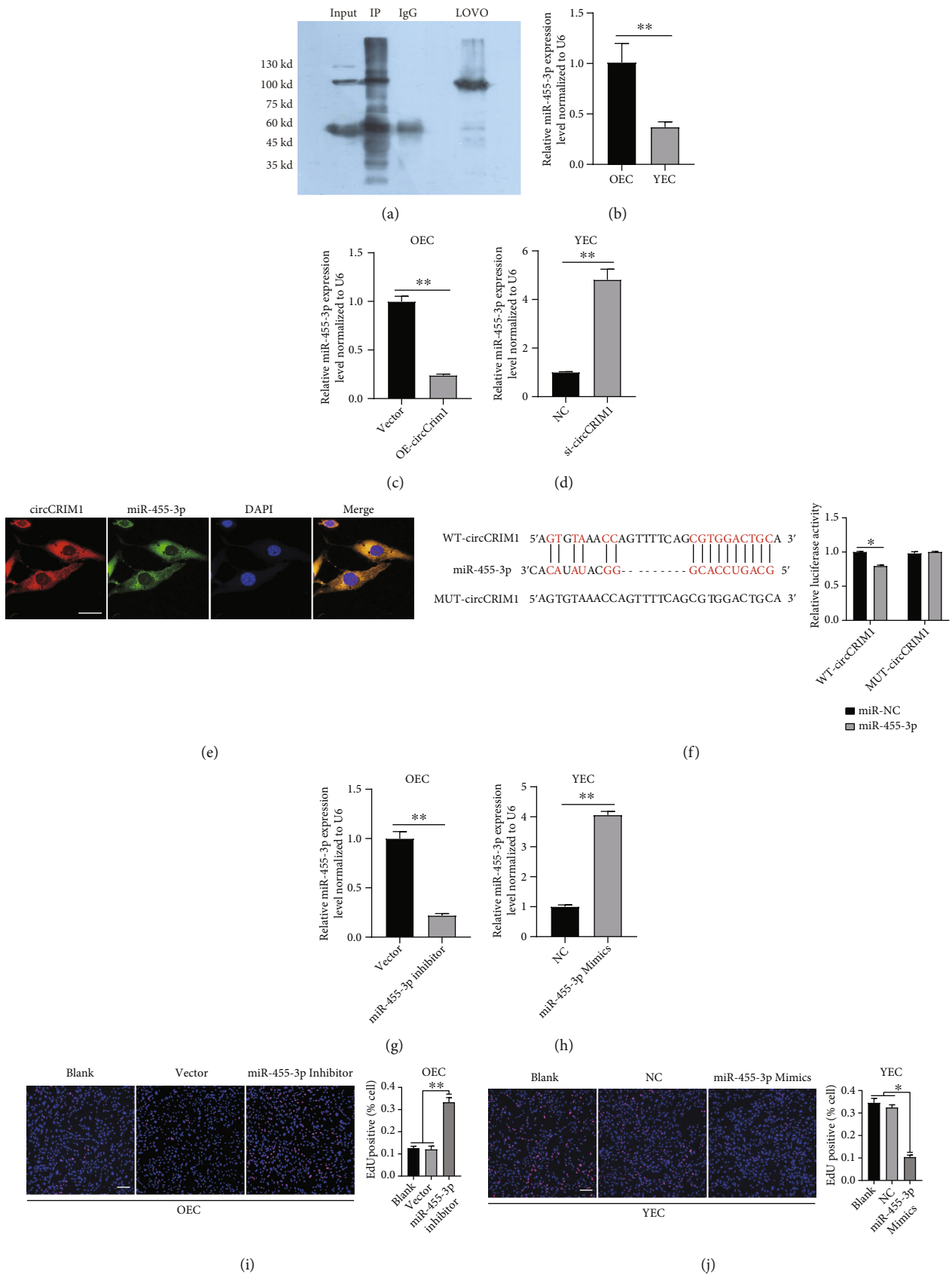

Figure 3: Continued.

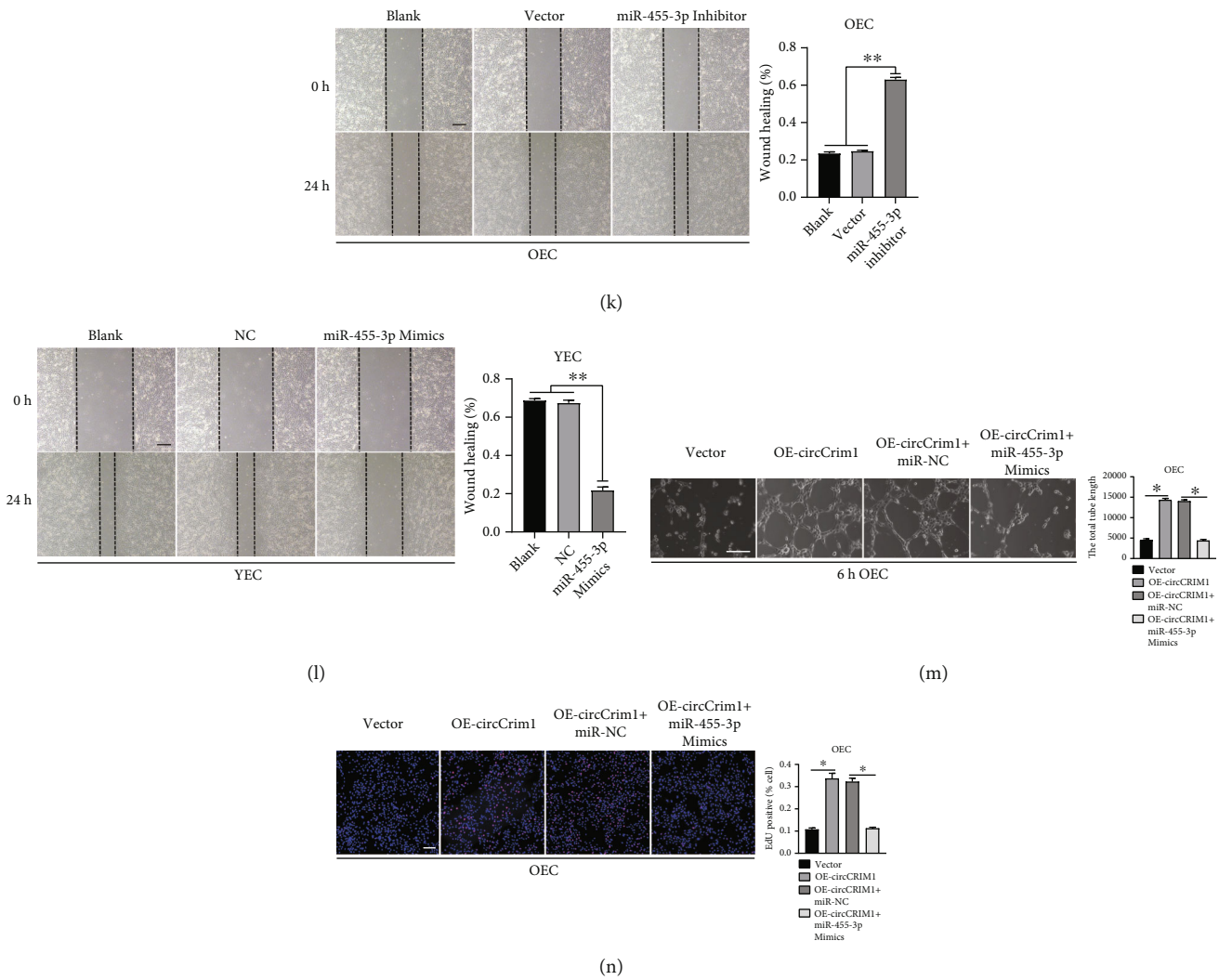

Figure 3: MiR-455-3p is the downstream target of circCRIM1 and inhibits the proliferation, and migration of MAECs. (a) RIP assay was performed in OEC, followed by western blot to detect AGO2 expression. (b) MiR-455-3p was significantly overexpressed in the OEC compared with the YEC ($n = 3$). (c) MiR-455-3p expression was downregulated by overexpressing circCRIM1 in OEC ($n = 3$). (d) MiR-455-3p expression was upregulated in YEC transfected by circCRIM1 siRNA ($n = 3$). (e) The results of the FISH experiments showed the colocalization of circCRIM1 and miR-455-3p (magnification, 400×, scale bar, 15 μm) ($n = 3$, analyzed 8 cells). (f) Schematic diagrams of the circCRIM1-WT and circCRIM1-MUT structure. Luciferase assay proved that miR-455-3p suppressed the luciferase activity of the circCRIM1 3′-UTR-WT construct but not the circCRIM1 3′-UTR-MUT construct. (g) qRT–PCR results showed successful miR-455-3p silence in OEC ($n = 3$). (h) qRT–PCR results showed successful miR-455-3p upregulation in YEC ($n = 3$). (i) OEC proliferation capacity was increased by the inhibitor of miR-455-3p ($n = 3$, scale bar, 100 μm). (j) YEC proliferation capacity was diminished by the miR-455-3p mimic ($n = 3$, scale bar, 100 μm). (k) Transfection of the inhibitor of miR-455-3p invigorated OEC migration in the *in vitro* wound healing assay ($n = 3$). (l) Transfection of the miR-455-3p mimic impaired YEC migration in the *in vitro* wound healing assay ($n = 3$). (m) Tube formation assay of OECs treated with vector, OE-circCRIM1, OE-circCRIM1+miR-NC, or OE-circCRIM1+miR-455-3p mimics ($n = 3$, scale bar, 100 μm). (n) EdU assay of OECs treated with vector, OE-circCRIM1, OE-circCRIM1+miR-NC or OE-circCRIM1+miR-455-3p mimics ($n = 3$, scale bar, 100 μm). (The data are presented as the mean ± SD, $^{*}P < 0.05$, $^{**}P < 0.01$ versus the negative control).

The OEC tube formation rate was accelerated because of circCRIM1 upregulation, but this augmentation was reduced by cotransfection with the miR-455-3p mimic (Figure 3(m)). Moreover, overexpressing circCRIM1 increased the OEC proliferation, but failed to maintain this increase in proliferation in the presence of the miR-455-3p mimic (Figure 3(n)). These results suggested that miR-455-3p is a downstream target of circCRIM1, playing a vital role in regulating MAEC angiogenesis.

3.6. Twist1 is the Downstream Target of MiR-455-3p. To further investigate the target genes of miR-455-3p, we searched the potential mRNA targets through the miRanda and RNA-hybrid databases and found that Twist1 expression was directly regulated by miR-455-3p. qRT–PCR results revealed that the Twist1 mRNA level was significantly lower in OEC than in YEC (Figure 4(a)). Twist1 mRNA was also downregulated after transfection of the miR-455-3p mimic in YEC (Figure 4(b)). A western blot analysis showed that the

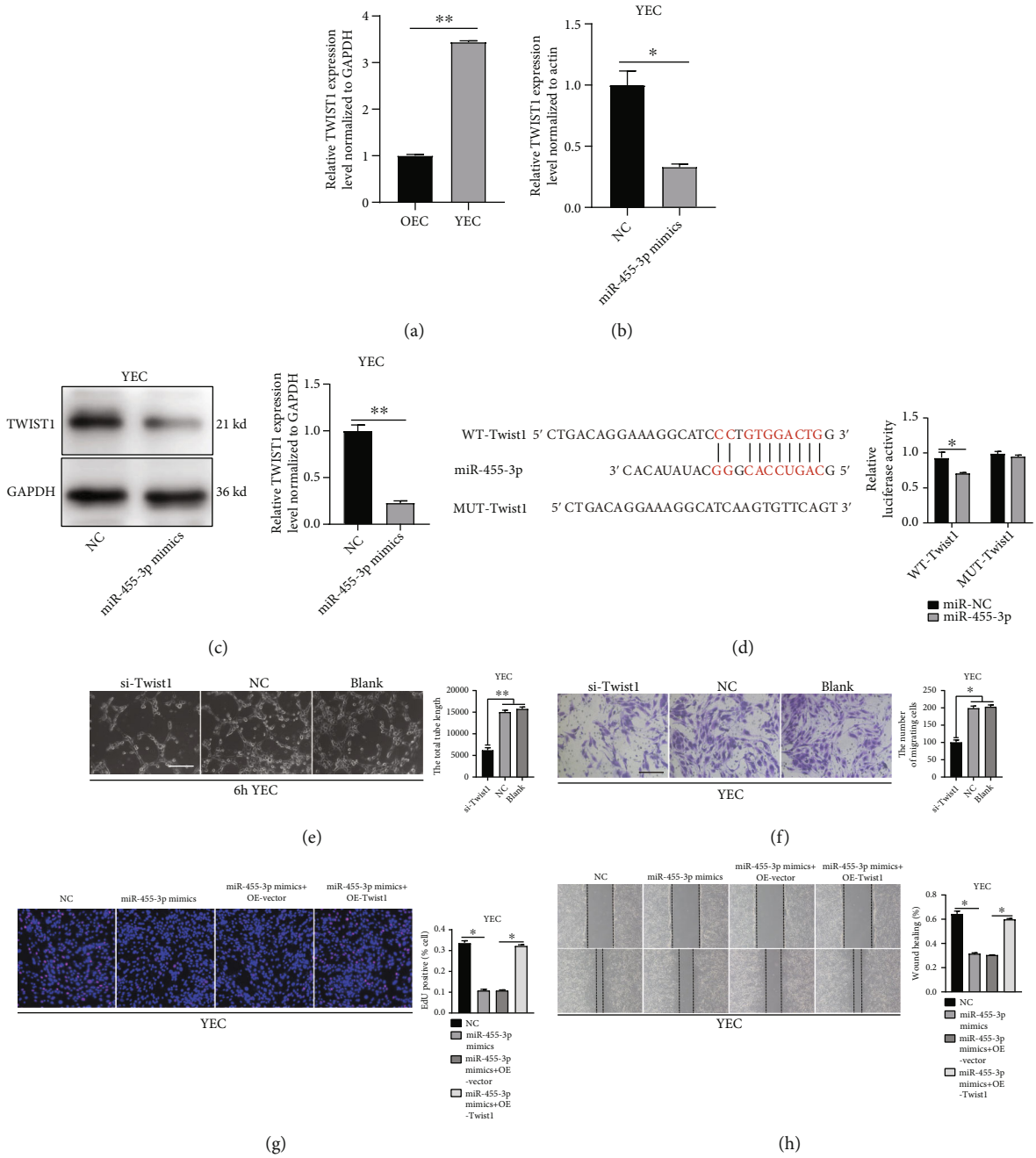

Figure 4: Twist1 is the downstream target of miR-455-3p. (a) qRT–PCR results showed that the Twist1 mRNA level was significantly lower in OEC than in YEC ($n = 3$). (b) The Twist1 mRNA level was decreased in YEC transfected with miR-455-3p mimic ($n = 3$). (c). Western blot analysis showed that the miR-455-3p mimic resulted in decreased Twist1 expression. (d) Schematic diagrams of the Twist1-WT and Twist1-MUT structure. Luciferase assay proved that Twist1-WT 3′UTR but not the MUT 3′UTR was suppressed by miR-455-3p mimics. (e) Silencing Twist1 diminished YEC tube formation ($n = 3$, scale bar, 100 μm). (f) Silencing Twist1 diminished YEC migratory capacity in the Transwell assay ($n = 3$, scale bar, 100 μm). (g) EdU assay of YEC treated with NC, miR-455-3p mimics, miR-455-3p mimics +vector or miR-455-3p mimics +OE-Twist1 ($n = 3$). (h) *In vitro* wound healing assay of YEC treated with NC, miR-455-3p mimics, miR-455-3p mimics +vector, or miR-455-3p mimics +OE-Twist1 ($n = 3$). (The data are presented as the mean ± SD, $^{*}P < 0.05$, $^{**}P < 0.01$ versus the negative control).

miR-455-3p mimic resulted in decreased Twist1 expression (Figure 4(c)). In the luciferase assay, miR-455-3p significantly inhibited luciferase activity in the MAECs transfected with Twist1 3'-UTR-WT, but not in the MAECs transfected with Twist1 3′-UTR-MUT (Figure 4(d)). Then, we transfected Twist1 siRNA into YEC to silence the Twist1 expression. A tube formation assay showed that Twist1 siRNA impaired the tube formation capacity of YEC (Figure 4(e)).

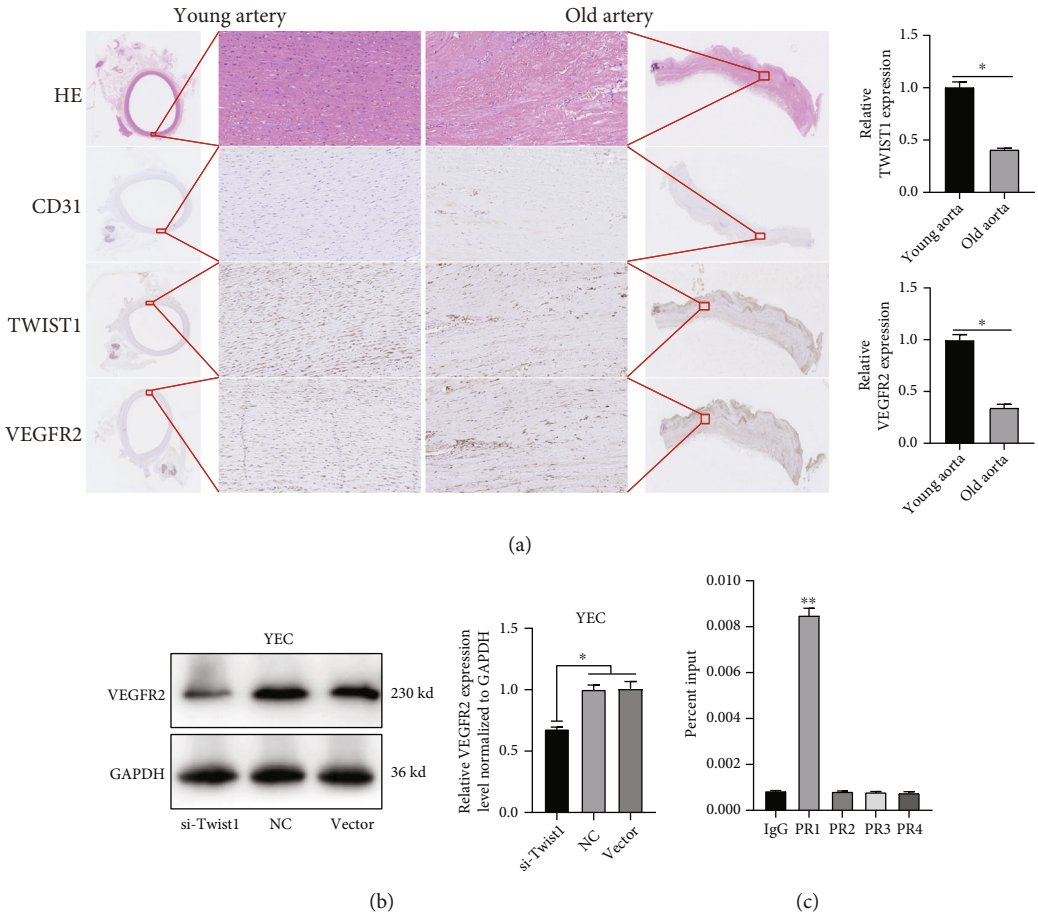

Figure 5: Twist1 acts as a transcription factor to regulate VEGFR2 expression. (a) Representative images of immunohistochemistry staining for Twist1 and VEGFR2 and relative expression levels of young patients' arterial and old patients' arterial tissue ($n = 3$). (b) Western blot analysis of the Twist1 expression in YECs transfected with si-Twist1 or NC ($n = 3$). (c) The CHIP experiment followed by qRT–PCR results showed that Twist1 was coprecipitated with the VEGFR2 primers 1. (The data are presented as the mean ± SD, $^{*}P < 0.05$, $^{**}P < 0.01$ versus the negative control).

In a Transwell assay, the migratory capacity of the YECs was also reduced after Twist1 silencing (Figure 4(f)).

Rescue experiments were performed to estimate the regulation of angiogenesis by miR-455-3p via Twist1 mRNA. The YEC proliferation rate was decreased after transfection of the miR-455-3p mimic, but this attenuation was prevented by Twist1 overexpression (Figure 4(g)). The *in vitro* wound healing assay results showed that upregulation of Twist1 expression reversed the low migratory capacity of YEC resulting from transfection of the miR-455-3p mimic (Figure 4(h)).

3.7. Twist1 Is a Transcription Factor that Regulates VEGFR2 Expression. Twist1 is a transcription factor that regulates gene expression by binding to the promoter region. We performed a bioinformatics prediction analysis using the Jaspar database. Notably, the VEGFR2 gene sequence was potentially targeted by Twist1 through four binding sites. To verify the age-related expression of Twist1, immunohistochemistry staining for Twist1 and VEGFR2 was performed and showed that, compared to that of old patients, the arterial tissue of young patients exhibited higher expression (Figure 5(a)). Furthermore, western blot analysis showed that the VEGFR2 protein level was significantly decreased in YEC transfected with Twist1 siRNA (Figure 5(b)). To further pinpoint the predicted binding sites between VEGFR2 and Twist1, four primers for the VEGFR2 gene promoter region were applied to a ChIP–qPCR experiment. The qRT–PCR results showed that Twist1 coprecipitated with primer 1. These results indicated the interaction between Twist1 and VEGFR2 gene promoter regions (Figure 5(c)).

3.8. CircCRIM1 Ameliorated Angiogenesis in Lower Limb Blood Flow Recovery in Aging Mice. We aimed to characterize the function of circCRIM1 in age-related lower limb ischemia *in vivo*. Aging mice were subjected to unilateral femoral artery ligation that cut off blood flow in the hind limbs, which was realized when the gastrocnemius muscle was injected with PBS or AAV9 particles carrying circCRIM1 or a vector 2 weeks before the establishment of the model, while the contralateral hind limbs and young mice injected with PBS on ipsilateral hind limbs were established as NC.

A PeriCam PSI imager was used to monitor blood flow before and 0, 3, 7, 14, 21, and 28 days after the operation (Figure 6(a)). The perfusion analysis showed that blood flow

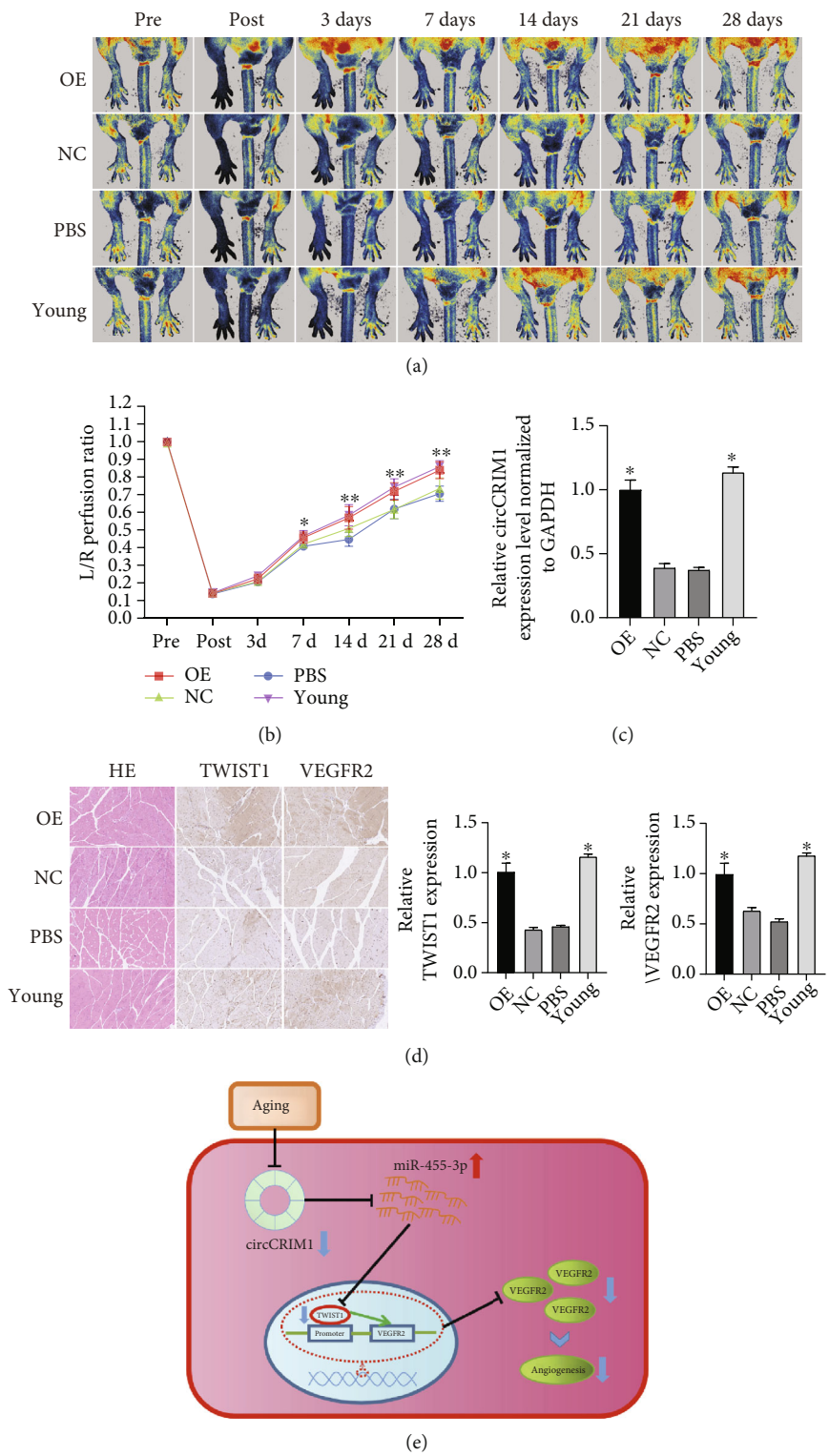

Figure 6: Overexpression of circCRIM1 ameliorated angiogenesis in lower limb blood flow recovery in aging mice. (a) Representative images of perfusion in the mice's femoral artery before and 0, 3, 7, 14, 21, and 28 days after the operation ($n = 5$). (b) Perfusion analysis was presented as the indexes by calculating the perfusion ratio of ischemic limbs to normal limbs before and 0, 3, 7, 14, 21, and 28 days after the operation ($n = 5$). (c) CircCRIM1 expression was markedly increased by AAV9-circCRIM1 in old mice gastrocnemius muscle sampled 2 weeks after the operation and was equivalent to that in the young group. (d) Representative images of the immunohistochemical staining for HE, anti-Twist1, and anti-VEGFR2 in mouse left lower limb gastrocnemius muscles sampled 28 days after surgery. The Twist1 and VEGFR2 expression were markedly increased in the circCRIM1 overexpression group compared with the NC group, and was equivalent to that in the young group ($n = 5$) (The data are presented as the mean ± SD, $^{*}P < 0.05$, $^{**}P < 0.01$ versus the negative control). (e) Schematic plot showed that circCRIM1 ameliorated angiogenesis in aging mice.

was increased 7, 14, 21, and 28 days after surgery in the circCRIM1 overexpression group compared with the NC group (Figure 6(b)), suggesting that circCRIM1 significantly improved blood flow recovery of the ischemic lower extremities *in vivo*. Furthermore, the qRT–PCR results confirmed that the abundance of circCRIM1 was markedly increased by AAV9-circCRIM1 in the gastrocnemius muscle sampled two weeks after the operation (Figure 6(c)). Consistent with these results, immunohistochemical staining for Twist1 and VEGFR2 in gastrocnemius muscle tissues in the circCRIM1 overexpression group sampled 28 days after surgery was also markedly increased compared with that in the NC group, and was equivalent to that in the young group. Taken together, these findings suggest that circCRIM1 acts as a miR-455-3p sponge inducing angiogenesis via the miR-455-3p/Twist1/VEGFR2 axis (Figure 6(e)).

4. Discussion

CircRNAs were initially discovered in virus research in the 1970s [10]. In the 1990s, an early report of circRNAs in eukaryotes showed that the mouse sperm-related gene Sry and the human ETS1 gene generated circRNAs through transcription [11, 12]. Previous studies showed that circRNAs were likely to be unfunctional byproducts of incorrect gene splicing due to a low abundance. However, with the rapid development of high-throughput sequencing in recent years, circRNAs have drawn a lot of interest with the characteristics of endogenous, abundant, conserved, and stable. CircRNAs participate in regulating the occurrence and development of various human diseases through transcriptional and protein translation [13, 14]. In this study, circCRIM1 was significantly decreased in OEC, and overexpression of circCRIM1 promoted OEC proliferation, migration, and tube formation capacity, suggesting that circCRIM1 was involved in EC angiogenesis in aging mice.

CircRNAs were revealed to action in the following ways: (1) as molecular sponges for miRNAs, adsorbing and sequestering miRNAs and thus playing a competitive inhibitory role; (2) as partners of RBPs, affecting RBP function; (3) as mediators of transcriptional regulatory elements by direct binding; and (4) as templates in protein-coding and translation [4, 15, 16].

Numerous studies support that circRNA can be miRNA sponges, which is an important aspect of the ceRNA regulatory mechanism hypothesis. It has been reported that ciRS-7 binds to AGO2 protein and competitively sponges miR-7, thereby regulating the expression of downstream target genes in the human brain [17]. CircRNA-Sry acts as a miR-138 sponge, thereby inhibiting its biological activity and playing a regulatory role in the occurrence and development of various pathologies [18]. Circ-ITCH acts in the miR-7/EGFR pathway to promote the migration and invasion of osteosarcoma cells through sponge adsorption [19]. CircHIPK3 elevates CCND2 expression and promotes cell proliferation and invasion in gliomas via miR-124 [20]. However, research on the ceRNA mechanism of circRNAs in aging ECs was infrequently reported.

Evidence of a high abundance in the cytoplasm and sufficient binding sites for target miRNAs proves that circRNAs can participate in regulating cellular functions by sponging miRNAs. In this study, we found that circCRIM1 was abundantly localized in the cytoplasm in mouse ECs through a FISH experiment. These results supported that circCRIM1 acts as a miRNA sponge. AGO2 is a core protein in RNA-induced silencing complexes (RISCs) that take charge of RNA interference and gene silence by cleaving target mRNA in the cytoplasm [21]. We found that circCRIM1 binds to the AGO2 protein Using RIP experiments, providing important evidence that circCRIM1 regulates the biological functions of vascular ECs through ceRNA mechanisms.

When seeking to identify the downstream target genes of circCRIM1, we found that miR-455-3p may be the target of circCRIM1 on the basis of the miRanda database and RNAhybrid database. To verify the interaction between circCRIM1 and miR-455-3p, qRT–PCR was performed after overexpressing circCRIM1 in OEC and knocking down circCRIM1 expression in YEC. The results showed that miR-455-3p was significantly and negatively correlated with the changes in circCRIM1 expression and that miR-455-3p was significantly more abundant in the OEC compared to YEC. Then, we performed FISH experiments and found that circCRIM1 and miR-455-3p colocalized in the cytoplasm. Moreover, a luciferase assay showed that miR-455-3p bound circCRIM1, thereby inhibiting circCRIM1 expression and regulating EC function in mice.

MiR-455-3p plays an inhibitory role in tumor angiogenesis, but its role in physiological angiogenesis affected by aging is still unclear. Therefore, after transfecting miR-455-3p mimics and inhibitors into MAECs, we found that inhibition of miR-455-3p expression enhanced OEC proliferation, tube formation, and migratory capacity, while YEC functions were attenuated after overexpression of miR-455-3p, as determined through a series of *in vitro* and *in vivo* experiments. In addition, we found stronger evidence of circCRIM1 regulating miR-455-3p through a rescue experiment. In OEC overexpressing circCRIM1, cotransfection of miR-455-3p mimics inhibited the angiogenesis-related phenotypes acquisition of OEC that had been enhanced by circCRIM1 upregulation. These results support that miR-455-3p is a downstream target of circCRIM1 and participates in regulating EC angiogenesis.

Studies have shown that miRNAs affected EC function by accelerating mRNA degradation and decreasing mRNA translation [22]. We performed bioinformatics analysis using the miRanda database and RNAhybrid database and found that Twist1 may be a downstream target gene of miR-455-3p. To further investigate Twist1 function, qRT–PCR was performed and showed that Twist1 mRNA level was significantly decreased in YEC transfected with the circCRIM1siRNA or miR-455-3p mimic, followed by western blotting determined that the Twist1 protein expression level was markedly downregulated. These results suggest that Twist1 expression was affected by miR-455-3p and circCRIM1. To further verify the relationship between Twist1 and miR-455-3p, we performed a luciferase assay and found that miR-455-3p bound Twist1 and inhibited Twist1

expression, but this phenomenon disappeared when the predicted binding site was mutated. Therefore, we confirmed that miR-455-3p is directly bound to Twist1 mRNA and regulated EC function in mice.

Studies have reported that Twist1 is a transcription factor that plays a role in cell development, tumor metastasis, and epithelial-mesenchymal transition in vertebrates [23, 24]. In various malignancies, such as sarcoma, melanoma, and glioblastoma, Twist1 is found that regulates tumor cell invasion and metastasis [25–27]. However, the study of the Twist1 in regulating angiogenesis has been controversial. The expression of Twist1 in the retinal capillary endothelium increased VEGFR2 expression, thereby promoting retinal angiogenesis in neonatal mice [28]. Nevertheless, the increased Twist1 expression with lower VEGFR2 levels was observed in older human adipocytes and mouse lung cells. And further overexpressing Twist1 in EC of mouse lung resection model was not related to the reduced VEGFR2 expression level and impaired proliferation or migratory capacity of EC. In contrast, overexpression of Twist1 increased VEGFR2 expression [29]. Intriguingly, we found that Twist1 was significantly downregulated in OEC compared with YEC. Therefore, we speculate that the role played by Twist1 in regulating vascular EC function may be tissue-specific.

To identify the role of Twist1 in MAECs, we found that the tube formation and migration rates were increased in the OEC overexpressing Twist1. Furthermore, the tube formation and migration rates were attenuated after the transfection of Twist1 siRNA in YEC. Then, we performed a rescue experiment and found that cotransfection of the Twist1 overexpressing plasmid released the inhibition of angiogenesis-related phenotype acquisition resulting from transfection of the miR-455-3p mimic in YEC.

Twist1 has been reported to be a transcription factor that binds the promoter region of VEGFR2 with an E-box domain that was highly conserved [28]. In this study, VEGFR2 expression was found to be parallel to Twist1 expression in MAECs. We predicted the possible binding sites of Twist1 to the promoter region of VEGFR2 on the basis of the Jaspar database. And then, based on the sense strand, we designed 4 pairs of primers for a ChIP–qPCR assay. The results showed that Twist1 bound to the promoter region of VEGFR2 (primer 1). We also determined the expression of Twist1 and VEGFR2 in arterial tissue in young and old patients through immunohistochemistry staining. And these results showed that the Twist1 and VEGFR2 expressions were significantly increased in young arteries than those in arteries. Therefore, it is believed that Twist1 promotes angiogenesis by promoting the expression of VEGFR2 in MAECs, which further supports the tissue-specific angiogenic effect of Twist1, as suggested in the literature.

To further study the effect of circCRIM1 on angiogenesis *in vivo*, we established a lower extremity femoral artery ischemia mice model and found that overexpressing circCRIM1 significantly accelerated the mouse ischemic limb blood flow recovery compared with those in the NC group and was equivalent to young mice group. The expression levels of Twist1 and VEGFR2 were higher in the OE-circCRIM1 group than in the NC group, as determined by immunohistochemistry staining. These results indicate that circCRIM1 can promote capillary regeneration after lower extremity ischemia and enhance blood flow recovery after acute lower extremity ischemia in aged mice *in vivo*.

5. Conclusion

In summary, we showed that upregulation of circCRIM1 reversed the angiogenic dysfunction of aging EC by targeting the miR-455-3p/Twist1/VEGFR2 axis *in vivo* and *in vitro*. This finding sheds light on a novel insight that circCRIM1 may be a potential therapeutic target for aging-related PAD.

Data Availability

The data used to support the findings of this study are available from the corresponding author upon reasonable request.

Conflicts of Interest

The authors declare that there are no conflicts of interest.

Authors' Contributions

Lei Zhao and Rencong Chen contributed equally to this work.

Acknowledgments

Our research was supported by the National Natural Science Foundation of China (No.81873813) and the Natural Science Foundation of Guangdong Province (No.2020A1515011412). We are very grateful to Joshua Wang for his considerable contribution to the manuscript writing and revising.

Supplementary Materials

Table I: SiRNA sequence for mouse gene used in this study. Table II: qRT–PCR primers for mouse genes used in this study. Table III: The primers for VEGFR2 used in ChIP–qPCR. Table IV: The probe sequences of circCRIM1 and miR-455-3p used in the FISH experiments. *(Supplementary Materials)*

References

[1] A. X. Gao, Z. Tong, Y. Wu, L. Guo, Y. Gu, and A. Dardik, "Similarities and differences in peripheral artery disease between China and Western countries," *Journal of Vascular Surgery*, vol. 74, no. 4, pp. 1417–1424.e1, 2021.

[2] Z. S. Katusic and S. A. Austin, "Endothelial nitric oxide: protector of a healthy mind," *European Heart Journal*, vol. 35, no. 14, pp. 888–894, 2014.

[3] C. Regina, E. Panatta, E. Candi et al., "Vascular ageing and endothelial cell senescence: molecular mechanisms of physiology and diseases," *Mechanisms of Ageing and Development*, vol. 159, pp. 14–21, 2016.

[4] L. S. Kristensen, M. S. Andersen, L. V. W. Stagsted, K. K. Ebbesen, T. B. Hansen, and J. Kjems, "The biogenesis, biology and characterization of circular RNAs," *Nature Reviews Genetics*, vol. 20, no. 11, pp. 675–691, 2019.

[5] W. R. Jeck, J. A. Sorrentino, K. Wang et al., "Circular RNAs are abundant, conserved, and associated with ALU repeats," *RNA*, vol. 19, no. 2, pp. 141–157, 2013.

[6] K. Wang, B. Long, F. Liu et al., "A circular RNA protects the heart from pathological hypertrophy and heart failure by targeting miR-223," *European Heart Journal*, vol. 37, no. 33, pp. 2602–2611, 2016.

[7] C. Liu, M. D. Yao, C. P. Li et al., "Silencing of circular RNA-ZNF609 ameliorates vascular endothelial dysfunction," *Theranostics*, vol. 7, no. 11, pp. 2863–2877, 2017.

[8] J. Qiu, R. Chen, L. Zhao et al., "Circular RNA circGSE1 promotes angiogenesis in ageing mice by targeting the miR-323-5p/NRP1 axis," *Aging*, vol. 14, no. 7, pp. 3049–3069, 2022.

[9] J. Wang, X. Z. Peng, R. M. Lassance-Soares et al., "Aging-induced collateral dysfunction: impaired responsiveness of collaterals and susceptibility to apoptosis via dysfunctional eNOS signaling," *Journal of Cardiovascular Translational Research*, vol. 4, no. 6, pp. 779–789, 2011.

[10] C. Cocquerelle, P. Daubersies, M. A. Majérus, J. P. Kerckaert, and B. Bailleul, "Splicing with inverted order of exons occurs proximal to large introns," *The EMBO Journal*, vol. 11, pp. 1095–1098, 1992.

[11] Y. Tay, J. Rinn, and P. P. Pandolfi, "The multilayered complexity of ceRNA crosstalk and competition," *Nature*, vol. 505, no. 7483, pp. 344–352, 2014.

[12] B. Capel, A. Swain, S. Nicolis et al., "Circular transcripts of the testis-determining gene _Sry_ in adult mouse testis," *Cell*, vol. 73, no. 5, pp. 1019–1030, 1993.

[13] Y. Yang, X. Fan, M. Mao et al., "Extensive translation of circular RNAs driven by N^6-methyladenosine," *Cell Research*, vol. 27, no. 5, pp. 626–641, 2017.

[14] J. Xue, Y. Liu, F. Luo et al., "Circ100284, via miR-217 regulation of EZH2, is involved in the arsenite- accelerated cell cycle of human keratinocytes in carcinogenesis," *Biochimica et Biophysica Acta (BBA) - Molecular Basis of Disease*, vol. 1863, no. 3, pp. 753–763, 2017.

[15] "Circular RNAs are a large class of animal RNAs with regulatory potency," *Nature*, vol. 495, no. 7441, pp. 333–338, 2013.

[16] J. Zang, D. Lu, and A. Xu, "The interaction of circRNAs and RNA binding proteins: an important part of circRNA maintenance and function," *Journal of Neuroscience Research*, vol. 98, no. 1, pp. 87–97, 2020.

[17] J. Chen, J. Yang, X. Fei, X. Wang, and K. Wang, "CircRNA ciRS-7: a novel oncogene in multiple cancers," *International Journal of Biological Sciences*, vol. 17, no. 1, pp. 379–389, 2021.

[18] J. T. Granados-Riveron and G. Aquino-Jarquin, "Does the linear Sry transcript function as a ceRNA for miR-138? The sense of antisense," *F1000Research*, vol. 3, p. 90, 2014.

[19] H. Li, M. Lan, X. Liao, Z. Tang, and C. Yang, "Circular RNAcir-ITCH promotes osteosarcoma migration and invasion throughcir-ITCH/miR-7/EGFR pathway," *Technology in Cancer Research & Treatment*, vol. 19, no. 12, 2020.

[20] Z. Liu, S. Guo, H. Sun, Y. Bai, Z. Song, and X. Liu, "Circular RNA CircHIPK3 elevates CCND2 expression and promotes cell proliferation and invasion through miR-124 in glioma," *Frontiers in Genetics*, vol. 11, article 1013, 2020.

[21] A. L. Teixeira, A. S. Patrão, F. Dias et al., "AGO2expression levels and related genetic polymorphisms: influence in renal cell progression and aggressive phenotypes," *Pharmacogenomics*, vol. 22, no. 16, pp. 1069–1079, 2021.

[22] Z. Ali Syeda, S. S. Langden, C. Munkhzul, M. Lee, and S. J. Song, "Regulatory mechanism of MicroRNA expression in cancer," *International Journal of Molecular Sciences*, vol. 21, no. 5, 2020.

[23] T. Mammoto, A. Jiang, E. Jiang, and A. Mammoto, "Role of Twist1 phosphorylation in angiogenesis and pulmonary fibrosis," *American Journal of Respiratory Cell & Molecular Biology*, vol. 55, no. 5, pp. 633–644, 2016.

[24] J. Meng, S. Chen, J.-X. Han et al., "Twist1 regulates vimentin through Cul2 circular RNA to promote EMT in hepatocellular carcinoma," *Cancer Research*, vol. 78, no. 15, pp. 4150–4162, 2018.

[25] S. Choo, P. Wang, R. Newbury, W. Roberts, and J. Yang, "Reactivation of TWIST1 contributes to Ewing sarcoma metastasis," *Pediatric Blood & Cancer*, vol. 65, no. 1, 2018.

[26] P. Zhang, C. Huang, C. Fu et al., "Cordycepin (3′-deoxyadenosine) suppressed HMGA2, Twist1 and ZEB1-dependent melanoma invasion and metastasis by targeting miR-33b," *Oncotarget*, vol. 6, no. 12, pp. 9834–9853, 2015.

[27] X. Cai, S. Feng, J. Zhang, W. Qiu, M. Qian, and Y. Wang, "USP18 deubiquitinates and stabilizes Twist1 to promote epithelial-mesenchymal transition in glioblastoma cells," *American Journal of Cancer Research*, vol. 10, no. 4, pp. 1156–1169, 2020.

[28] J. Li, C. H. Liu, Y. Sun et al., "Endothelial TWIST1 promotes pathological ocular angiogenesis," *Investigative Ophthalmology & Visual Science*, vol. 55, no. 12, pp. 8267–8277, 2014.

[29] K. Hendee, T. Hunyenyiwa, K. Matus, M. Toledo, A. Mammoto, and T. Mammoto, "Twist1 signaling in age-dependent decline in angiogenesis and lung regeneration," *Aging*, vol. 13, no. 6, pp. 7781–7799, 2021.